ELECTROSTATIC CONTROL OVER TEMPERATURE-DEPENDENT TUNNELING ACROSS SINGLE-MOLECULE JUNCTIONS

by

ALVAR RODRIGUEZ GARRIGUES
B.S. University of Science and Arts of Oklahoma, 2010
M.S. University of Central Florida, 2013

A dissertation submitted in partial fulfillment of the requirements
for the degree of Doctor of Philosophy
in the Department of Physics
in the College of Science
at the University of Central Florida
Orlando, Florida

Spring Term
2016

Major Professor: Enrique del Barco

ABSTRACT

The aim of the present dissertation is to improve the understanding and methodology of temperature-dependent tunnel conduction through individual molecules by single-electron transport spectroscopy. New advances in electrochemistry present individual molecular diodes as a realistic option for the implementation on molecular circuits thanks to their high current rectification ratios. Therefore, a major requisite in this field is to understand and control the conduction behaviors for a large variety of conditions. This work focuses on the electric conduction through ferrocene-based molecules as a function of temperatures within a wide range of bias and gate voltages by means of three-terminal electromigrated-broken single-electron transistors (SETs).

The results show that the temperature dependence of the current (from 80 to 260 K) depends strongly on the bias and gate voltages, with areas in where the current increases exponentially with temperature (at the Coulomb blockade regimes), and others where the increase of the temperature makes the current only to vary slightly (at resonance) or to decrease monotonically (at the charge degeneracy points). These different observed behaviors of the tunneling current with increasing temperatures can be well explained by a formal single-level coherent tunneling model where the temperature dependence relies on the thermal broadening of the Fermi distributions of the electrons in the leads. The model portraits the molecule as a localized electrostatic level capacitively coupled to the transistor leads, and the electrical conduction through the junction as coherent sequential tunneling.

To my father, my mother and my sister Granada

ACKNOWLEDGMENTS

I think back over the past years here at the University of Central Florida and I have really enjoyed them. And that has been possible thanks to the many people who I have been surrounded that I would like to thank now.

First, I would like to thank UCF for giving me the means and time for achieving my Ph.D., as well as, the Department of Physics where there are/were a lot of very helpful people: Jessica, Monika, Elisabeth, Esperanza, Mike, Pat and Felix.

Thanks to the people that, inside my lab, I could learn and shared my time: Firoze Haque (taught me how to fabricate transistors), Hajrah Quddusi, Asma Amjad, Simranjeet Singh (always there to teach/help me in the lab and often very late!), James Atkinson, Rebecca Cebulka, Priyanka Vaidya, Christopher Coleman and Tyler Townsend.

Thanks to: Dr. Masahiro Ishigami and Dr. Eloy Hernandez, who I could always count for help and their knowledge made me better. Also: Dr. Robert Peale, Dr. Eduardo Mucciolo, Dr. Talat Rahman, Dr. Ahlam Al-Rawi, Dr. Jacquelyn Chini, Guy Zummo, David Bradford, Ray Ramotar and Phillip Chan. Also, thanks to Dr. Christian Nijhuis and Dr. Lejia Wang for their knowledge in chemistry and synthesizing molecular diodes.

Special thanks to Dr. Elena Flitsiyan who always was there supporting me. I have truly enjoyed her company teaching physics labs through these years.

Also, I would like to acknowledge the Grad students who at some point share time and ideas with me: Jaekyun, Evan, Jyoti, Ryuichi, Lin, Takat, Abrar, Udai, Anu, Narae, Patricio,

Farnood, Mike, Sebastian, Javi, Tu, Cristian, Yuli, Carlos, Cameron, Daniel, Imen, Javaneh Westley, Pedro, Jonathan, Akbar, Will and Byron. Special thanks to Diego and Mark for that great semester abroad enjoying physics.

Thanks to the people that have accompanied me outside the lab: Belen, Javi, Tracy, Chris and the group of Spaniards here in Orlando.

Now, I would like to name Marta Anguera Antoñana because she has not only accompanied me as a lab-mate but as a friend. I really think that without her everything would have been more difficult. She was always there listening to me, answering very wisely to my questions and making me love my time here.

I know that I couldn't finish this Ph.D. without the wise advice for almost 6 year of Dr. Enrique del Barco. I can't be prouder for learning physics with him, for programming challenging experiments and make them work in the lab, for his complete support in everything I have proposed and for the knowledge he shared with me. I liked physics when I started here but not even close to the way I do now, thanks!

To finish, I would like to thank my family, my brother and my sisters: Javier, Cristina, Elena and Susana. Thank you mom and dad for being as you are and thank you Granada. Granada, you were gone the same day I defended the proposal for this Ph.D. but I know that you have always been with me. I always remember you, I love you Granada.

TABLE OF CONTENTS

LIST OF FIGURES

LIST OF TABLES

CHAPTER 1:
INTRODUCTION AND BACKGROUND

1.1. Electrical Tunneling Transport Spectroscopies

Advances in the control of electrical transport through molecular tunnel junctions have risen as an important tool for understanding the different transport regimes which may govern future molecular electronics devices. Aimed at studying tunneling conduction in molecular tunnel junctions, several sophisticated experimental techniques have substantially advanced over the last years, including electromigrated single-electron transistors (SET) [1-9], scanning tunneling microscopy (STM) break-junctions [10-11], and self-assembled monolayers (SAM) of molecules sandwiched between two macroscopic electrodes [12-22], among others.

STM break-junctions can be used to obtain statistics on electron transport at an individual molecular level but the supramolecular and the electronic structure of the junctions cannot be investigated independently. By contrast, it is possible to measure both the supramolecular and electronic structure of the SAMs immobilized on one of the electrodes (usually referred to as the bottom-electrode) using standard surface characterization techniques before fabrication of the top-contact. For most of these systems, however, it is not clear how much the energy level alignment changes once the molecules are in contact with the top-electrodes [23] and therefore models are often lacking to extract all the relevant transport parameters. In spite of the poor understanding of the specifics, from a technological point of view SAM-based junctions are promising candidates for molecular electronics technologies, with rectification ratios rapidly approaching values of commercial semiconductor devices [24,25].

On the other hand, three-terminal SETs electrically gate the molecular electronic states of an individual molecule, enabling the full spectroscopic resolution of the molecular energy landscape giving the possibility of manipulating molecules, as a function of magnetic fields and/or temperatures, in order to tune its intrinsic properties for a final implementation in molecular circuits [1-9]. However, they encompass other intrinsic limitations, such as a low experimental yield.

1.2. Single-electron Transistors

SETs are three-terminal nanoscale devices with the ability of studying quantum dots (QD) or quantum "islands" by means of electrical conduction and capacitive coupling. The mechanics in these transistors works similar to the field-effect transistor, with the peculiarity that the conduction channel involves a single quantum system. This tremendously small conducting channel exhibits intrinsic quantum mechanics of the system such as the quantization of the current flowing through the device and tunnel effects in the electric conduction, among others [1-9].

SETs consist of two conducting lead electrodes (source/drain or left/right) connected to a QD, with a third electrode (back-gate) electrically isolated from the leads and the dot. Figure 1 shows a schematic diagram of a three-terminal single-electron transistor. The QD creates a junction between the source and drain leads on top of the gate electrode. In this disposition the dot capacitively couples with the electrodes creating three different capacitances: C_s, C_d and C_g, respectively. Moreover, conducting electrons can tunnel from the source/drain leads, in and out of the dot in a sequential tunneling transport process by means of an electric bias potential (V_{bias}),

through a potential barrier that energetically separates the leads from the QD. The transport of the electrons through the device is determined by two tunnel rates, represented by Γ_S and Γ_D, from the source and drain, respectively, which account for the number of electrons tunnelling through the tunnel junction per unit of time. In turn, the third electrode (gate) capacitively couples with the electrochemical potential of the dot, being able to tune its energy levels upon application of electrostatic gate voltage (V_{gate}).

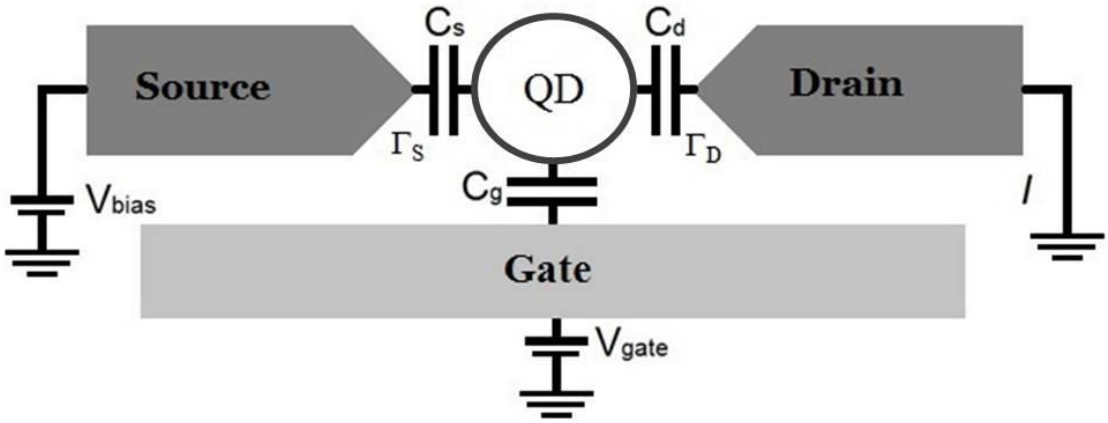

Figure 1: Schematic diagram of a SETs device. A quantum dot (QD) surrounded by three electrodes: source, drain and gate. V_{bias} describes the electric potential between the source and drain lead electrodes while V_{gate} represents the voltage applied to the gate. C_s, C_d and C_g are the different capacitances between the QD and the electrodes. Γ_s and Γ_d represent the tunneling rates for the electrons flowing in and out of the QD.

As mentioned above, the electric transport in SETs is driven by electrons tunneling in and out of the QD from/to the electrodes in a sequential process. This process is activated when the system is driven to the conducting resonance. For a better understanding Figure 2 reproduces the energy diagram of a molecular SET with a quantum dot between the source and drain electrodes. In this diagram, the Fermi energy of the electrodes (black regions) is at equilibrium and characterized by the electrochemical potential, μ_S and μ_D, of the source and the drain, respectively, and can be increased by the applied bias, V_{bias}. The grey bars represent the tunnel

potential barriers that separate the electrons in the leads to the ones in the dot. These barriers depend on the coupling between the dot and the electrodes and ultimately determine the tunnel characteristics of the device. Finally, in between the conducting electrodes and the barriers, the QD is described by discrete molecular energy levels filled up to the number of electrons, *N*, in the thermal equilibrium of the dot, μ_N. Solid lines represent the occupied energy states and dashed lines the unoccupied states.

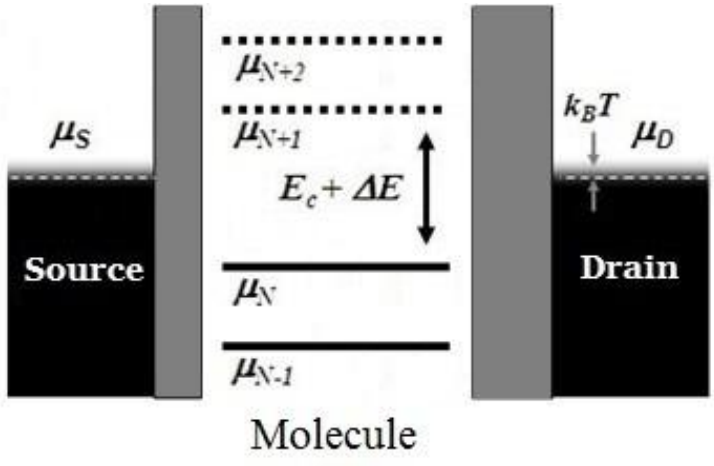

Figure 2: Schematic energy diagram in a SET. A quantum dot (QD) is sandwiched between the source and drain electrodes (black regions) and two potential barriers (grey blocks). The QD is described by a discrete molecular energy levels in which the occupied energy levels of are marked as solid lines and the unoccupied in dashed lines. μ_S, μ_D, and μ_N denote the electrochemical potential in the source, drain and QD, respectively, where *N* is the number of electrons in the dot.

When the quantum dot is an individual molecule, the first solid line corresponds to the highest occupied molecular orbital (HOMO), μ_N, and the last dashed line to the lowest unoccupied molecular orbital (LUMO), μ_{N+1}. In the case of Figure 2, the system is at the Coulomb blockade configuration, in which the conduction through the device is suppressed since the conducting electrons, traveling from either the source or drain electrode, do not have enough energy for tunneling into the next available molecular energy level (LUMO) in the QD. In order

to bring the system into a resonance and have electrical conduction, the conduction electrons need a minimum energy of $E_c + \Delta E$ (E_c being the charging energy and ΔE the molecular electronic level spacing of the dot) more than the energy of the HOMO level, to open a new channel of conduction and add one more electron to the QD. In other words, transport in a SET occurs when the conduction electrons tunnel through the potential barriers with an energy equal or greater than the energy of the LUMO level with two alternatives of reproducing this scenario: a) by applying V_{bias} or b) by making use of V_{gate}. Of course, conduction can also occur involving the HOMO level, which will also enter the bias conduction window when applying a negative bias to the transistor. Indeed, in most cases of molecular SETs, the HOMO level is the one responsible for conduction, since it is the one closest to the Fermi energy of the metallic electrodes. When the HOMO-LUMO gap is reduced by energy renormalization effects due to the proximity of the metallic electrodes, then both levels can enter the conduction window and govern the electrical conduction through the junction. In general, one could see the following actions by the bias and gate electrostatic voltages:

a) V_{bias} raises/lowers the electrochemical potential in the source electrode (with respect to the drain lead) giving the conduction electrons energy enough to tunnel through the potential barrier and occupy the HOMO or LUMO level. At that point, electrons flow through the device increasing the current until the molecular level is completely filled. Once a level is involved (limiting the conduction to an electron at a time), further increasing of the V_{bias} does not translate into an increase of the current, until the next unoccupied energy level is reached. Consequently, the current only increases in steps separated by an energy equal to the energy separation between the molecular levels.

b) V_{gate} generates an electric field that energetically adds to the molecular energy levels of the dot/molecule. In this mechanism, V_{gate} can tune (gate) up or down the molecular energy levels allowing the alignment between the unoccupied molecular levels and the electrochemical potential of the conducting electrodes for different values of V_{bias}.

The work in this thesis applies only to individual molecules as QDs, where the electric conduction occurs after bringing the system into resonance, with, the individual molecule, oxidizing/reducing when accepting/giving one electron into/out of its electronic configuration. For individual molecules, the redox-energy falls into the range of 0.1-1 *eV* in solid state devices, therefore, in order to distinguish between molecular energy levels, the SET spectroscopy has to overcome any thermal energy ($k_B T$; k_B = 8.617 *eV/K*, Boltzmann constant), making it imperative to work at cryogenic temperatures.

1.3. Spectroscopy in Single-electron Transistors

The single-electron transport spectroscopy allows studying and understanding quantum systems such as individual molecules through electrical conduction. This spectroscopy is based in analysing the response in conduction of molecules after applying an electric potential difference (V_{bias}) while modifying the electrostatic energy of the molecule by means of a gate voltage (V_{gate}). When a molecule is placed in a SET and it is contributing to the conductance through the device, *I-V* curves will show, in principle, a constant value for the current followed by a rapid increase when the system reaches the energy resonance (*Section 1.2.*). Applying a V_{gate} the molecular levels in the molecule experience a shift in energy, which translates into a displacement in the rapid increase of the current when repeating the same I-V_{bias} measurement.

Figure 3a shows three different I-V_{bias} curves (current, I, in the *y-axis* and bias voltage, V_{bias}, in the *x-axis*) corresponding to three different V_{gate} values. The three curves in the graph start with a constant value for the current, at negative V_{bias}, where the conduction electrons in the drain (negative V_{bias}) have enough energy to tunnel through the device. Reducing the negative value of V_{bias}, the current sharply drops to zero since the electrons lose that much energy which maintained the electrochemical potential of the drain aligned with the HOMO level in the molecule. Here, the system is taken from the resonance state into the Coulomb blockade regime (*Section 1.2.*). This change in regime occurs at different V_{bias} for the three curves due to the different V_{gate} applied to each of them. On the other hand, for the positive V_{bias}, electrons in the source start at the Coulomb blockade regime with a suppression of the current in the system. By increasing V_{bias}, the electrochemical potential in the source make electrons obtain enough energy to realign with the LUMO level and tunnel though the device represented by a rapidly increase in the current. Once the LUMO level is occupied, the molecule does not accept more electrons, represented by a constant value for the current.

Figure 3b shows the differential conductance (dI/dV) of the same I-V curves plotted in Figure 3a, where the peaks represent the resonance alignment of the electrochemical potential in the leads with the LUMO level of the molecule.

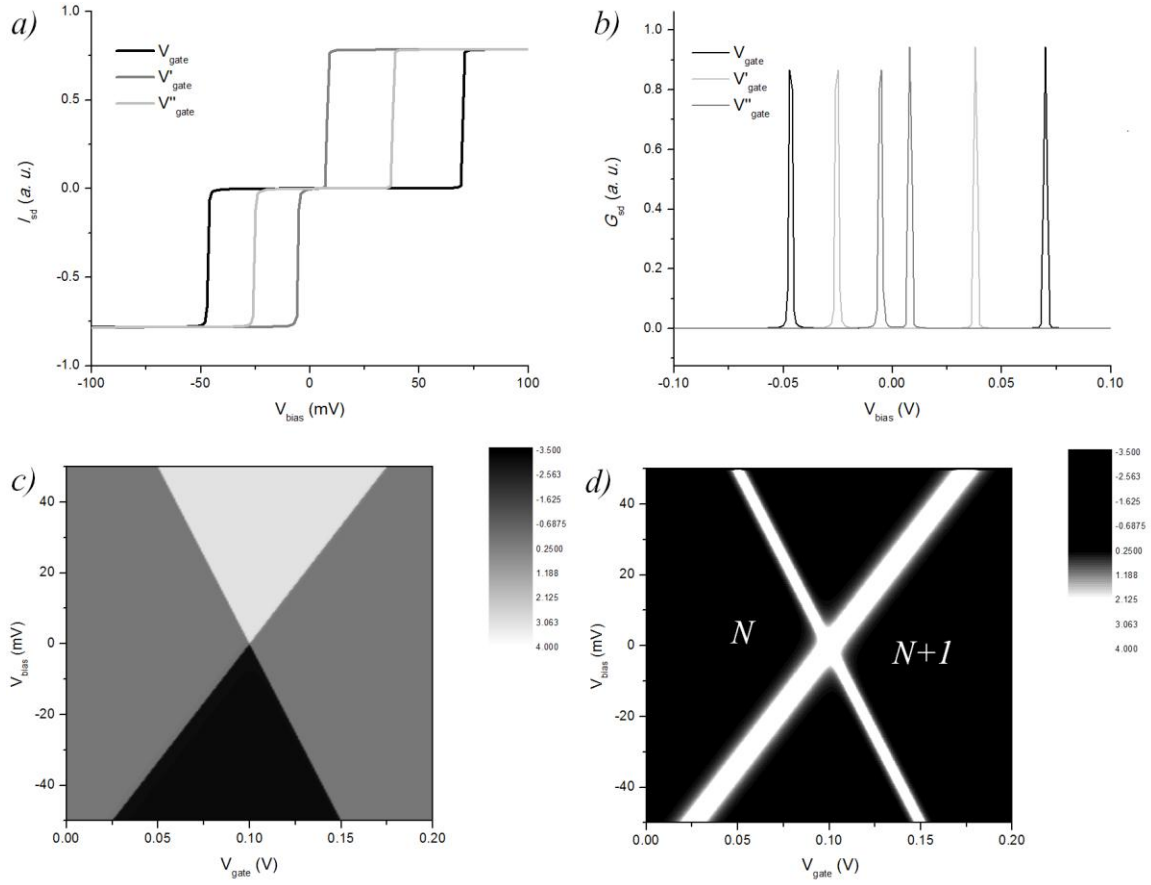

Figure 3: a) three *I*-V_{bias} curves for three different V_{gate} values. b) *dI/dV* plot for the three curves in (a). c) Coulomb blockade diamond diagram V_{gate} is in the *x-axis*, V_{bias} in the *y-axis* and current, *I*, in the *z-axis* (back and white coded). d) the *dI/dV* of (b) diagram, *N* represents the number of electrons in the molecule.

Moreover, a collection of these *I*-*V* curves can be united in a colour contour-plot with the V_{gate} in the *x-axis*, V_{bias} in the *y-axis* and current, *I*, in the *z-axis*. Figure 3c shows the response of a molecular SET with the characteristic Coulomb diamond (black and white coded). Positive current (in white) and the negative current (in black) reflect the sign of the conduction through the SET, where the other two areas (in grey) represent the Coulomb blockade regime where the current is suppressed. Figure 3d is the *dI/dV* analysis of Figure 3c. The single point where all conduction regimes meet is the charge degeneracy point or Coulomb peak (as seen in the V_{gate}

axis) and separates two different charge states within the molecule, *N* and *N+1* (*N* representing the number of electrons). The slopes correspond to different electrostatic couplings of the molecule with each of the electrodes, which are usually different in molecular SETs, where the position of the molecule with respect to each electrode is uncontrollable in the transistor gap.

1.4. Theory for Single-electron Transistors

1.4.1. Coulomb Blockade Theory

The Coulomb Blockade theory describes the mechanism of conduction in SETs. There are many reviews and theses with great level of detail in the field (see, e.g., Refs. [28-32]). In this section, it is not my intention to repeat what is already in the literature but to review and derive the most important concepts in the mechanism of the tunneling conduction in SETs as well as to present the formulas needed for the spectroscopy studies included in this work.

First, let us assume that the configuration of a conducting molecule bridging the leads of a SET can be considered as a spherical capacitor. This assumption is made due to the potential barriers that energetically separate the molecule to the electrodes creating two metallic shells and the capacitance coupling in the nature of the junction. Therefore, a molecule in a SET creates a charging energy equal to: $W = \frac{Q^2}{2C} = \frac{(Ne)^2}{2C}$, where *N* is the number of electrons in the molecule. Consequently, the total energy in the system is:

$$U(N) = \sum_1^N E_i + \frac{(Ne)^2}{2C} \qquad (1.1)$$

where E_i is the chemical potential of the molecule with *i* electrons. Now, when a new electron is promoted to a new orbital in the molecule, the total energy raises up to:

$$U(N+1) = \sum_1^{N+1} E_i + \frac{\left((N+1)e\right)^2}{2C} \quad (1.2)$$

Equation 1.1 and *Equation 1.2* are the energy expressions of two consecutive energies in the system when a single electron is added, and therefore, the subtraction of both will give the minimum energy required to add the *N*-th electron to an individual molecule which by definition is the electrochemical potential. Thus, the electrochemical potential in the molecule is:

$$U(N) - U(N-1) = E_N + \frac{(N-\frac{1}{2})e^2}{C} = \mu_N \quad (1.3)$$

Equation 1.3 defines the minimum energy necessary for conduction transport in SETs and this one will only occur when the electrochemical potential of the source, μ_S, or drain, μ_D, is higher than the one in the molecule, μ_N, and electrons have enough energy to tunnel through the device. In turn, when a single electron is added to the molecule and promoted to a new molecular orbital, the electrochemical potential μ_N increases to μ_{N+1}, giving the expression:

$$\mu_{N+1} = \mu_N + \frac{e^2}{C} + \Delta E \quad (1.4)$$

Here ΔE is $E_{N+1} - E_N$, and is defined as the electronic level spacing (the energy between molecular levels) and $\frac{e^2}{C}$ is the energy that the conduction electrons, in the leads, need to overcome the electric potential barrier that separates them from the molecule and hop into it; this energy is called the charging energy, E_c (previously described in *Section 1.2.*). These two quantities add up to the minimum energy necessary, to make the system fall into conducting

resonance. This energy will make electrons hop in and out of the molecule, one by one in a sequential way since only one electron can occupy one molecular orbital at a given time.

Let us now derive the electrochemical potential equations when V_{bias} and V_{gate} are present. Before, we assumed the capacitive coupling of the individual molecule with the electrodes and in *Section 1.2.* it was established that each electrode capacitively couples with the molecule creating a capacitance value. Therefore, the molecule must experience a total capacitance equal to the arithmetic sum of the individual capacitances with each of the electrodes, $C_t = C_g + C_s + C_d$. This total capacitance affects the electric potential applied into the device, *V,* which in terms of bias and gate voltage is:

$$V = \frac{1}{C_t}\sum C_i V_i = \frac{C_s}{C_t}V_{bias} + \frac{C_g}{C_t}V_{gate} \tag{1.5}$$

(Here, *Equation 1.5* accounts for the three electrodes of the system, although there is no term addressing the drain coupling. This is due to V_{bias} which being the electric potential between the source and drain electrodes is kept grounded at the drain side, $V_{drain} = 0$, therefore, this term vanishes and the only contribution comes from the C_s).

Equation 1.5 is the external voltage, *V,* which depends on the voltages applied to the system and the coupling of the molecule in the junction. This can be simply added into the electrochemical potential, μ_N (*Equation 1.3),* as an extra energy, giving:

$$\mu_N = U(N) - U(N-1) = E_N + \frac{(N-1/2)e^2}{C_t} + eV \tag{1.6}$$

This is the new electrochemical potential in the molecule and from *Equation 1.6* we can determine that the number of electrons, *N*, is not affect by *V*, meaning that the charge addition energy ($E_C + \Delta E$), for two specific levels, remains always the same, whether or not more electrons are added to the system. However, the relative energy difference between electrochemical potential of the molecule, μ_N, and the two electrodes, μ_S and μ_D, is modified and becomes proportional to the ratio between the total and the individual capacitances of the electrodes.

Finally, when an electron is promoted to a new molecular orbital, the electrochemical potential of the *N+1* electron state, μ_{N+1}, in terms of bias and gate voltage, becomes:

$$\mu_{N+1} = E_0 + eV \tag{1.7}$$

where E_0 defines the electrochemical potential when V_{bias} and V_{gate} are initially equal to zero, *Equation 1.4*.

1.4.2. Gate Coupling and Charge Degeneracy Point

At this point, I would like to introduce a new term based on the efficiency of the gate. As mentioned in *Section 1.2.*, the gate voltage will add energy (in the form of electric field) to the levels within the molecule shifting (gating) them up or down. The magnitude of the electric field decreases with the square of the distance, therefore, the efficiency of the gate is related to the positioning of the molecule in the junction and thus to the capacitive coupling of the molecule to the gate. The capacitance created by the gate electrode, C_g, over the total capacitance of the system, C_t, gives the total efficiency of the gate, or gate coupling, $\beta = C_g / C_t$. This term acts as a

conversion factor from the energy value of the gate voltage, eV_{gate}, into the real energy applied to the molecule, $\beta\, eV_{gate}$.

In *Section 1.2.*, we defined that the conduction through the device can be achieved in two ways, and one of them was by fixing the V_{bias} value and then sweeping V_{gate}. In that case the energy produced by the gate should be greater than the electrochemical potential when V_{bias} and V_{gate} are initially equal to zero, $\beta\, eV_{gate} > E_0$. Thus, the LUMO level aligns with the Fermi energy of the source/drain electrode and conduction is allowed in the device. This alignment at zero bias is called the charge degeneracy point or Coulomb peak (as the transport differential conductance displays a peak). This point separates two different charge states within the molecule and it is defined as:

$$V_C = \frac{E_0}{|e|}\frac{1}{\beta} \tag{1.8}$$

1.4.3. Capacitances and Tunneling Rates

So far, we have seen how the disposition of the molecule in the junction controls the tunneling conduction depending on the capacitances that the molecule forms with the electrodes. The Coulomb blockade theory explains all the details extracted from the SET spectroscopy such as the interpretation of the diamond slopes in Figure 3c-d. These slopes are related to the coupling of the molecule with the electrodes based on the ratio between the capacitances of the system and the tunneling probability rates.

The conformation of the molecule defines the tunnel probabilities or tunnel equations (number of electrons tunneling per unit of time), whose derivations are detailed in *Appendix C* as formalism of the theory of the *Chapter 3*.

For deriving the ratio of the capacitances in the system we need to go to the moment when the conductance is allowed in the system. As explained before, this occurs when the molecular level aligns with the electrochemical potential of the source, $\mu_{N+1} = \mu_S$. Solving *Equation 1.7* using *Equation 1.5* and *Equation 1.8*, we obtain:

$$\mu_{N+1} = E_0 + e\frac{(V_{bias}C_s + V_{gate}C_g)}{C_t} = e\frac{(V_{bias}C_s + (V_{gate} - V_C)C_g)}{C_t} = eV_{bias} = \mu_S \tag{1.9}$$

in which solving for V_{bias}:

$$V_{bias} = \frac{C_g}{C_t - C_s}(V_{gate} - V_C) = \frac{C_g}{C_g + C_d}(V_{gate} - V_C) \tag{1.10}$$

And in the same way, solving *Equation 1.7* when the alignment is produced between the LUMO and the electrochemical potential of the drain electrode ($\mu_{N+1} = \mu_D$), for V_{gate}, we obtain:

$$V_{drain} = -\frac{C_g}{C_s}(V_{gate} - V_C) \tag{1.11}$$

These two *Equation 1.10* and *Equation 1.11* give the shift of the conducting resonance as V_{gate} is applied, which follows a linear behavior (see Figure 3c and Figure 3d). This simple analysis brings two formulas and three variables for the capacitances in the system, therefore, only a ratio in between the three capacitances can be extracted from the SET spectroscopy.

1.4.4. Change in Spin, ΔS

To finish with this short review of the theory for single-electron transistors, I would like to add one more feature that can be extracted from the spectroscopy. This is the change in the spin of the molecule when one electron is promoted or removed from a molecular level. The change can be extracted by the movement of the charge degeneracy point when a magnetic field is applied, since this is the transition between two consecutive charge states and its position depends on the energy difference between them. After applying a magnetic field this energy difference is modified and, if the molecule is isotropic, the electrochemical potential depends linearly with the magnetic field. Then, the Zeeman effect allows to extract the change in spin and infer the oxidation states of the molecule [32].

$$\Delta E(B) = \big(E_{N+1}(B) - E_N(B)\big) - \big(E_{N+1}(0) - E_N(0)\big) = -g\mu_B B\Delta S \tag{1.12}$$

$$\Delta E(B) = \beta e \Delta V_C(B) = -g\mu_B B\Delta S \tag{1.13}$$

here, β is the gate coupling, e is the electron charge, g is the electron Lande factor, μ_B is the Bohr magneton, B is the magnitude of the magnetic field and ΔS is the changing in spin from S_{N+1} to S_N.

NOTE: At the end of Appendix B, two codes for Wolfram Mathematica facilitate the application of these formulas for the extraction of the principal parameters analyzed in this section.

1.5. Molecular Diodes

Ferrocene-based molecules are presented as realistic candidates for molecular diodes in the future implementation of molecular circuits thanks to their high current rectification ratios

between forward and reverse bias [16-25,33]. They are composed of an iron atom sandwiched by two benzene rings. The ferrocene molecules were synthesized differently by our collaborator group in Singapore depending on the different studies for the work in this thesis. Figure 4a shows the schematic view of the molecules chosen for temperature-dependent measurements (*Chapter 4*) in which the molecular junctions measured were formed by *S-$(CH_2)_4$-Fc-$(CH_2)_4$-S* (*Fc* : ferrocene) molecules (*Appendix D* for synthetic details), where the two thiol terminations (*S*) help the molecule connect to the opposite SET bias leads, and the four saturated carbon groups $(CH_2)_4$ on each side of the ferrocene unit help isolate the molecular conduction level (localized at the ferrocene) from the leads, with gold as the metal for the electrodes. The reason behind choosing these molecules for the temperature-dependent studies resides in that only the ferrocene participates in the conduction, while the saturated carbon groups in the alkyl linkers (molecule backbone) are passive elements providing isolation from the leads (tunnel barriers).

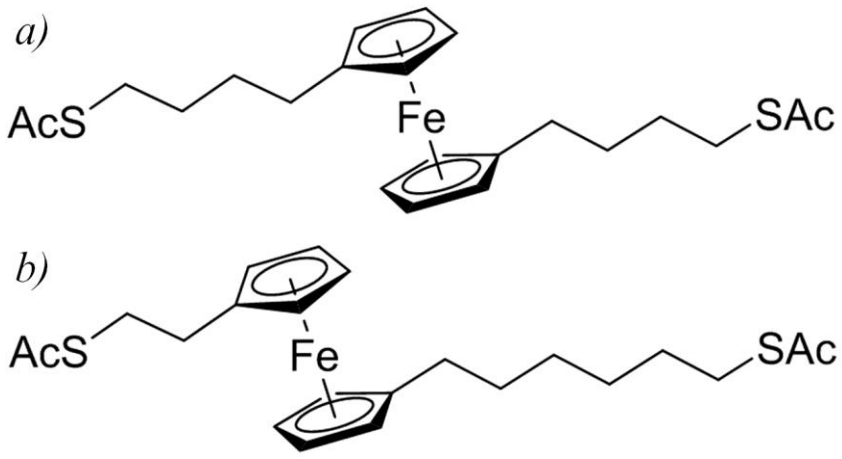

Figure 4: a) S-$(CH_2)_4$-Fc-$(CH_2)_4$-S (Fc:ferrocene) molecules. Two thiol terminations (S) protected by Acetate, and the four saturated carbon groups $(CH_2)_4$ on each side of the ferrocene. b) S-$(CH_2)_2$-Fc-$(CH_2)_6$-S (Fc:ferrocene) molecules. Similar molecules than (a) with two saturated carbon groups $(CH_2)_2$ in the left side and six $(CH_2)_6$ at the right side of the ferrocene unit.

Slightly different molecules were also synthesized for future experiments where the ferrocene unit was displaced by two carbon groups (CH_2) to one end creating asymmetry in the geometry of the molecule, Figure 4b. The difference between the molecules in Figure 4a and Figure 4b is expected to result in different conduction behaviors in the single-electron spectroscopy, since the ferrocene would have a stronger coupling with one electrode, creating the necessary asymmetry in the electrostatic potential to enable the rectification of electrical current through the junction. This is an on-going study, thus, not discussed in this thesis.

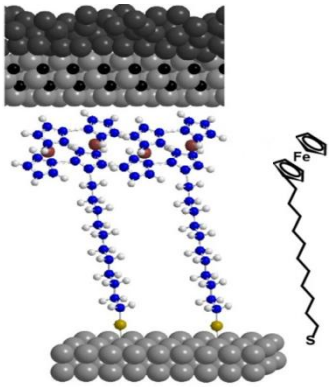

Figure 5: *S-C_n-Fc_2-C_{13-n}* (Fc:ferrocene) molecules. The double-ferrocene unit placed at the upper side of the molecule with the iron atoms in red. Then thirteen saturated carbon groups $(CH_2)_{13}$ (blue carbon and white hydrogen) in the lower side of the ferrocene finishing with the thiol terminations (S) in yellow.

Figure 5 shows a sketch of a molecular junction formed by a SAM of $S(CH_2)_{11}Fc_2$ molecules (with Fc_2 representing a biferrocenylene (Fc = Fc) head group) sandwiched in between two electrodes [24,34], which is another molecular junction studied in this thesis. In these junctions, the Fc_2 lies at the end of a long insulating alkyl chain, providing a non-covalent (van der Waals) coupling to the top electrode. This results in a highly asymmetric drop of electric potential at both sides of the Fc_2 (where the frontier orbitals are located) enabling large rectification ratios.

Another ferrocene-based molecule studied in this thesis has the form of *S-C_n-Fc-C_{13-n}*, where C_n represents the number of aliphatic carbons (CH_2 or a terminal CH_3), with n = 0 to 13, Figure 6. These molecules reported electrical rectification in *EGaIn* SAM-based junctions where the Fc unit was placed at 14 different positions within a SAM. When the ferrocene is positioned more than two carbon groups away from the electrodes the molecular level remains localized in the Fc unit, with the highest rectification ratios found for highly asymmetric molecules (Fc close to the electrodes), and with almost no rectification for symmetric molecules (Fc in the middle of the junction) [33].

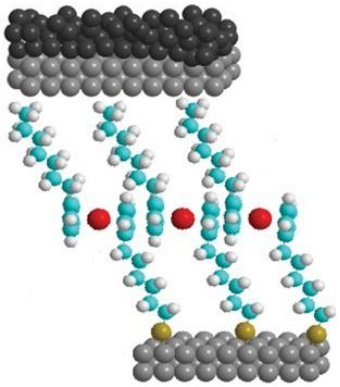

Figure 6: Sketch representation of the EGaIn SAM-based junctions formed by an Fc unit in red within the alkyl chain (carbon atoms in green and hydrogen in white), S-C_n-Fc-C_{13-n} molecule with n=7.

The control in the number of carbons at each side of the *Fc* unit allows to quantify the rectification response for different energetic symmetries in the junction, since the electric potential at both sides of the conduction unit will strongly depend on its position along the chain. This enables sampling the electrostatic potential profile along the junction's gap, which was found to be highly non-linear for this molecular junction [33].

CHAPTER 2:
FABRICATION AND METHODOLOGY

2.1. Fabrication of Single-electron Transistors

Single-electron transistors consist of three metal electrodes. Two of them are the conducting leads (source/drain or left/right), which are separated by a gap and carry the conduction through the device. This conduction occurs on top of the third electrode (back-gate electrode) electrically isolated from the other two at the surface and conducting at the inner part (Figure 7). The challenges in fabricating these transistors reside in that the gap between source/drain electrodes cannot be larger than a few namometers and that the thickness of the isolating layer in the gate electrode has to be minimum for maximizing the gate electric field on the molecules. Therefore, single-electron transistors belong to nanofabrication techniques where the whole process has to be spotless and mechanically exact.

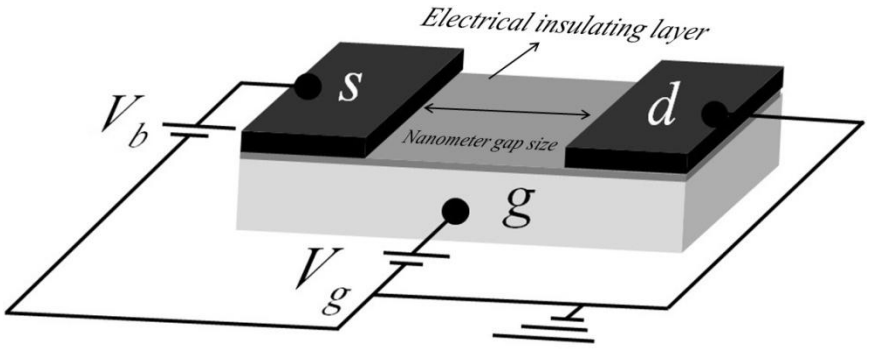

Figure 7: Sketch of a SET with two electrodes (source, s, and drain, d) separated by a gap, on top a thin insulating layer separating it from the gate electrode (g).

This section is allocated to explain the full fabrication of functional single-electron transistors. This fabrication is also explained in my M.S. thesis "*Development of and Efficient Molecular Single-Electron Transport Spectroscopy*" April 2013. In this thesis, I have updated this information including advances achieved since then in the optimization of the fabrication and electromigration-breaking processes.

NOTE: Appendix A contains the corresponding recipes for this fabrication process.

The single-electron transistors fabricated for the purpose of this thesis are a combination of both optical and electron-beam (e-beam) lithography processes [35,36]. The optical lithography creates three different metal layers configuring the basis of the circuit and the aluminum gate electrode (35 nanometers thick, 8 microns wide). On the other hand, the e-beam lithography fabricates thin gold nanowires (15 nanometers thick, 50 nanometers wide) on top and across the gate electrode in two separated metal layers. After the fabrication of the thin nanowires, these are forced to break in an electromigration-induced breaking procedure creating a small gap of a few nanometers. Figure 8 shows optical images of finished chips as an overview of the fabrication process and a closer view to two gates electrodes with nanowires on top.

The whole process of fabrication starts on a commercial Si/SiO_2 wafer (Table 3) cut in *1.8* square inches for fitting accommodations. Eventually, the fabrication process will lead to the creation of *1440* single-electron transistors, distributed in *36* chips, where each chip will contain *8* gates (connected in series) and each gate will have *5* nanowires with a common drain.

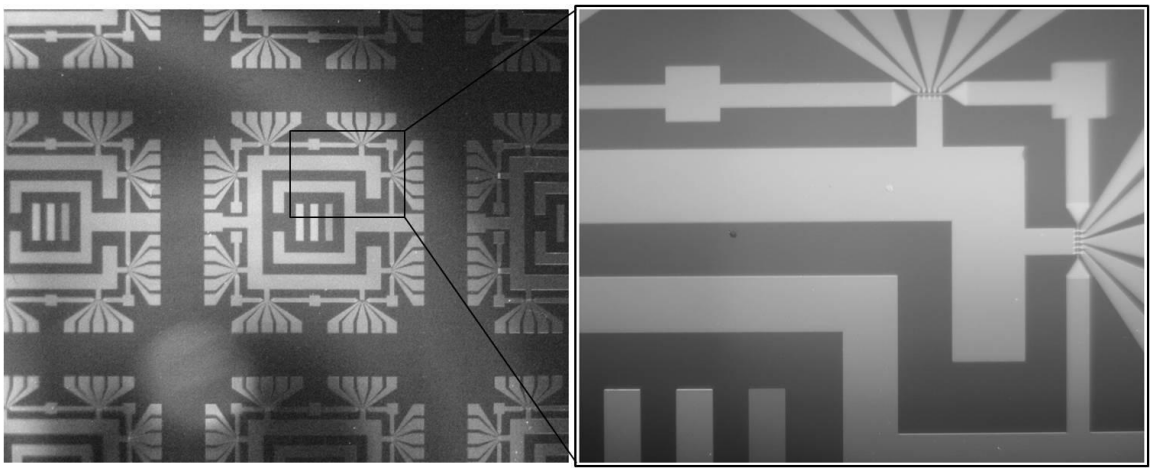

Figure 8: Pattern of the chips fabricated on top of the Si/SiO_2 wafer, one chip occupies 6 mm^2. A closer look into two back-gate electrodes with 5 nanowires on top of each.

2.1.1. Photolithography

Optical lithography is a very well-known procedure for device fabrication which, down to a few micrometers, can pattern with certain facility and low cost production. For these reasons, in the fabrication of these transistors, photolithography has the main goal of creating the larger parts of the circuit (major paths for wire bonding) and the gate electrode in a high production rate.

Spin-coating

Starting with the fabrication, the substrate needs to be cleaned by rinsing acetone, ethanol and isopropanol (IPA), in that order, and then blow dry with nitrogen gas. Then, the sample is spin-coated with *LOR 3A* and *Shipley S1813*, and baked in a hot plate for *5 minutes* at *175°C* and *2 minutes* at *120°C*, after each coating respectively. The specifications for spin coating these two photoresist are given in Table 4. The Shipley photoresist generates a layer of ~ 1.2 μm while the

LOR generates a layer of ~310 nm in thickness. The LOR helps in the lift off processes as undercutter, improving the final pattern.

UV Exposition

Once the sample is spin-coateded, it is properly patterned with a Fe/Fe_2O_3 photomask, manually aligned and exposed to ultraviolet (UV) light. $126\ \frac{mJ}{cm^2}$ is the exposing relation to UV light for the photoresists in this fabrication process. Then, the sample is developed with *CD-26 Developer* for *45 seconds* removing the damaged photoresists and, finally, submerged into *DI water*. The signature to recognize a success photolithography process resides in finding a spotless chip with sharp edges, in the features patterned, and a uniform color through the whole chip. After approving the lithography, the sample is baked at *130°C* for *5 minutes* and developed again in *CD-26* for *1 minute* followed by *DI water* in the undercut process.

At this point, the sample is ready for the evaporation of the different metals. It is highly recommended to O_2 plasma clean the sample, for a few seconds, right before introducing it into the vacuum chamber for the evaporation. This will remove the remaining residues of chemicals and water from the developing process leaving a cleaner surface and improving the adhesion of the metals. The parameters for this plasma cleaning are showed in Table 5.

Metal Lift-off

After the evaporation the next step is to lift off the metals from the sample. For this purpose the sample is introduced in *PG Remover* for a *few hours* for the two first layers. It may be possible to have to gently spray the sample with the PG itself or heat the PG with the sample up to *80°C* to help in this process. In the aluminum layer (back-gates in the transistor) the lift off

is made by dipping the sample in *Acetone* for a *few hours*, checking periodically, followed by *1 minute* in *PG*. Here, it is attempted to minimize the time of PG use since problems with the oxide layer were reported when using PG for this step. Therefore, as acetone will not remove the LOR, the PG will be still necessary in this process.

First Layer

Figure 9 is an example of the first thin layer of ~ 20 nm of thickness that sets the base of the chips and creates the contacts for the gate and source/drain electrodes. This layer has a combination of two layers on top of each other; 5 nm of titanium (Ti), as adhesion layer, and 15 nm palladium (Pd) as a conducting stainless metal, although gold could be use instead of palladium with the same results. The parameters given in Table 6 give the evaporation details.

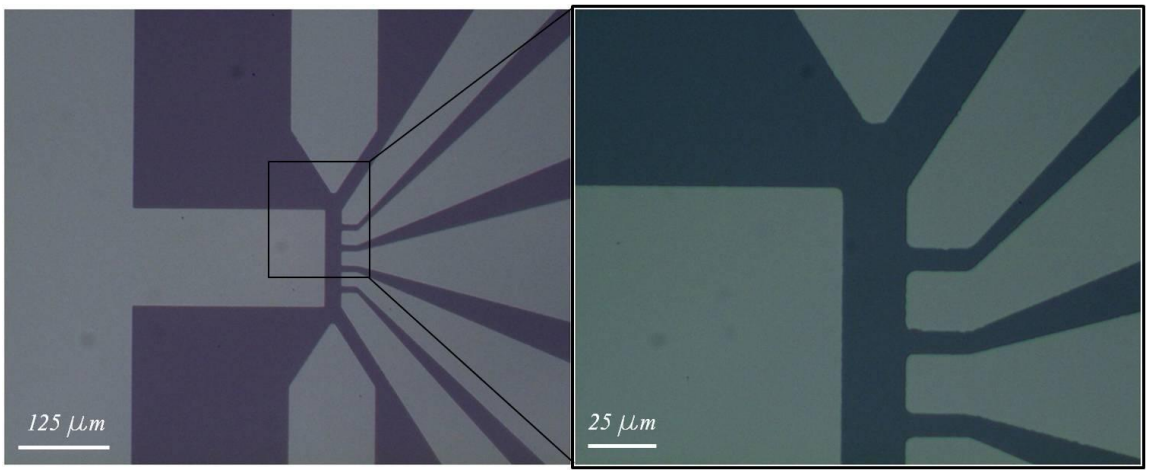

Figure 9: Optical images of the first layer. A layer of Pd (15nm) on top of another one of Ti (5nm) shown in light areas and evaporated on the Si/SiO_2 wafer as dark areas.

Second Layer

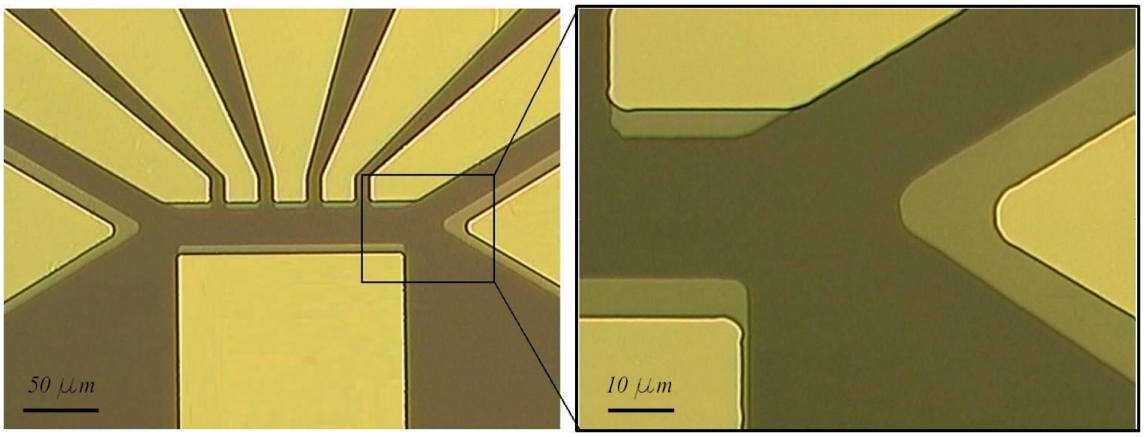

Figure 10: Optical images of the second layer e-beam evaporated of Ti (10nm) and Pd (70nm). In between the first layer (dark yellow) and the second layer (light yellow) there is a step with the first layer underneath.

Figure 10 shows optical images of the final result in the second layer deposited on top of the first one (dark shadows) which protrudes out of the edges of the second layer (light areas). The metal layer consists in 10 nm of titanium followed by 70 nm of palladium. The aligning of the second layer needs to coincide with the center of the first one, leaving out these few micrometers of the first layer at the edges in order to make the first layer contact the final electrodes with the overall circuit. The titanium and palladium layers are evaporated following the parameters given in Table 7. For this layer, gold can also replace palladium.

Third Layer

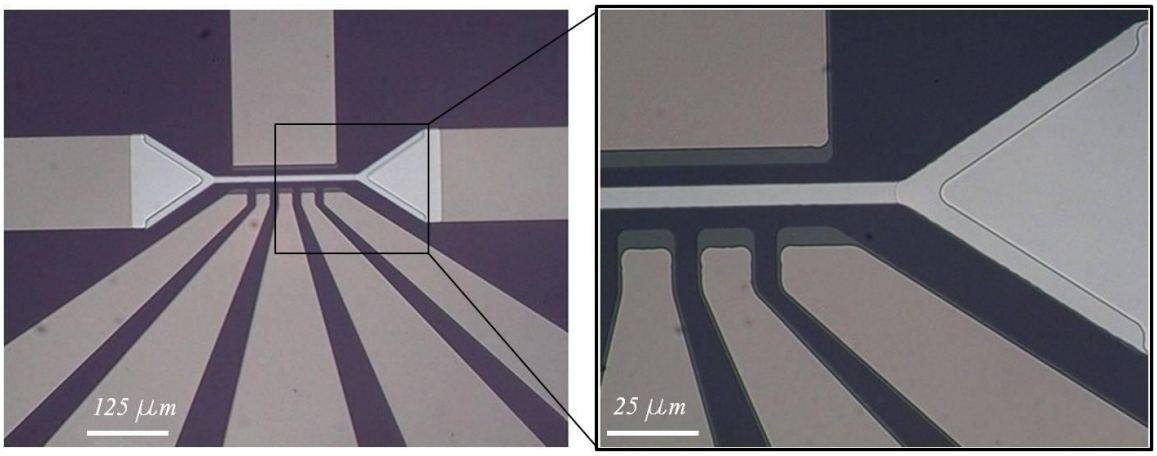

Figure 11: Optical images of the aluminum gate (35nm) in gray. The gate stands at the center of the pattern formed by the first two layers, first layer (Ti/Pd 5/15nm) in dark green and second layer (Ti/Pd 10/70nm) in light brown, as seen in the figure on the right.

The third layer forms the back-gate electrode in our SETs, therefore, it needs to display a thin insulating layer at the surface while maintain its high conductivity properties underneath. Aluminum is the metal chosen for providing these properties. 35 nm of aluminum are e-beam evaporated according to the parameters given in Table 8. The conduction properties of the aluminum can be checked at the probe station where it should give a final resistance of ~ 100 Ω. Optical images of the result in which the gate is aligned in the middle of the first two layers are shown in Figure 11.

After the aluminum evaporation and with the sample still inside the evaporation chamber, oxygen is introduced for *~45 minutes* at *~250 mTorr* for a homogeneous creation of the oxide layer at the surface and after the especial *Metal Lift-off*, mentioned above, the sample is forced to another oxidation with O_2 plasma with the specifications shown in Table 9.

2.1.2. E-beam Lithography

Electron-beam lithography is a sophisticated technique for nanofabrication in which a beam of electrons write detailed patterns with sizes that the photolithography cannot reach. This is the reason for which this process is selected for the conducting leads of the SETs producing thin nanowires of 50 nm wide which after an electromigration-induced breaking process create the nanogaps. Two superposed metal layers will create this step consisting on a set of 5 independent nanowires crossing on top of each of the 8 aluminum gates of each chip.

As mentioned before the nanowires will be the source and drain electrodes in our SETs. They will be 50 nm wide (minimum resolution of our e-beam writer at UCF CREOL) and 15 nm thick which results an optimized thickness for the electromigrating breaking process. At the same time, 15 mn will be the maximum distance for the molecule to the gate electrode once this one is in the gap creating a functional gate coupling in the spectroscopy.

The two superposed metal consist in a first layer of 15 nm that will go on top a 35 nm gate and consequently disconnected from the circuit. Then, a second layer is deposited on top, in order to connect the first nanowire layer with the overall circuit, except at the center of the nanowire which is left at 15 nm.

Spin-coating

First, the sample is spin-coated with *MMA (8.5) EL 6* and *950 PMMA C 2* e-beam resists and baked for *5 minutes* at *175°C*, in both cases. The parameters needed for this spin coating are given in Table 10.

E-beam Exposition

Once the sample is written by e-beam lithography it is developed in a solution composed of *3 IPA : 1 MIBK* for *45 seconds* and then rinsed with IPA.

Metal Lift-off

The lift-off process can take a long time and it needs to be performed carefully. It is very important to only use acetone and check it frequently. The solution has to be covered with Parafilm in a Petri dish to avoid the evaporation of the acetone.

First Layer

Figure 12 shows the results of the first thin nanowires layer (15 nm thick) following the parameters shown in Table 11. The nanowires land in the middle of the gate and in the thinnest part (50 nm wide), which will not be covered by the second thick nanowire layer, is where the electromigration-breaking process will occur.

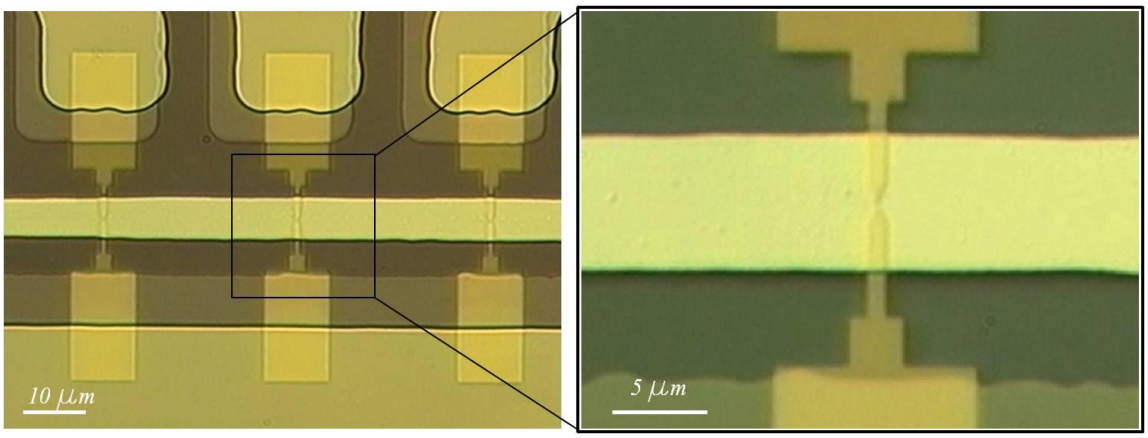

Figure 12: Optical images of the first nanowire layer. An overview of the nanowire in the circuit. Zoon into one single nanowire (15nm thick) observing the thinnest part at the center of 50nm wide.

Second Layer

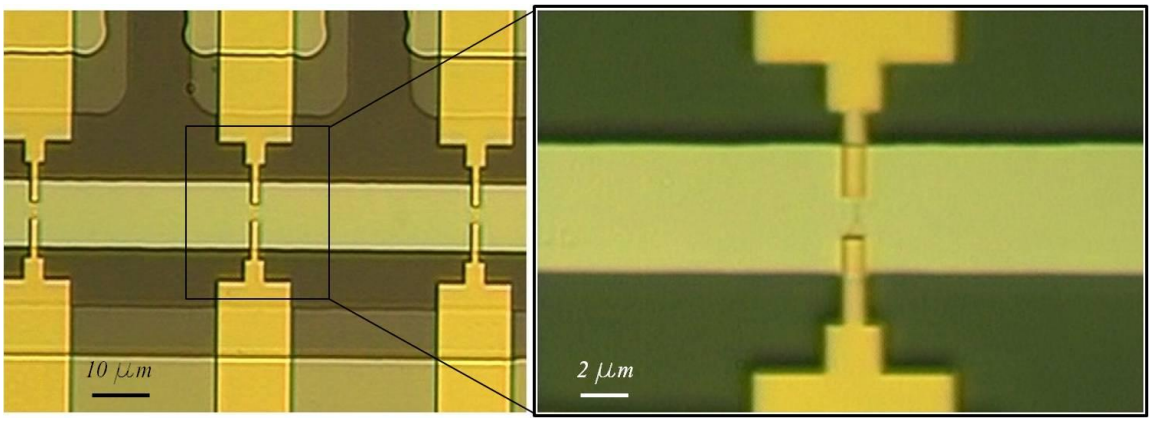

Figure 13: Optical images of the final nanowires lying on top of the Al gate. Zoom into a single wire, where the thinnest central part (nanowire) is left untouched by the second nanowire layer.

Figure 13 is the final result in the nanowire fabrication process showing the final aspect of the two layers of nanowires evaporated across the gate. This evaporation is divided in two steps of 25 nm where the current is driven to zero in between the steps for avoiding heating the sample and improving the lift off. The parameters for the e-beam evaporation of this last layer are given in Table 12.

Once the nanowires are finished, their resistances are measured in order to determine their quality. Usual resistances found in our devices are ~50 Ω. Figure 14 shows a SEM image of one single nanowire with a zoom in to the narrowest part of it.

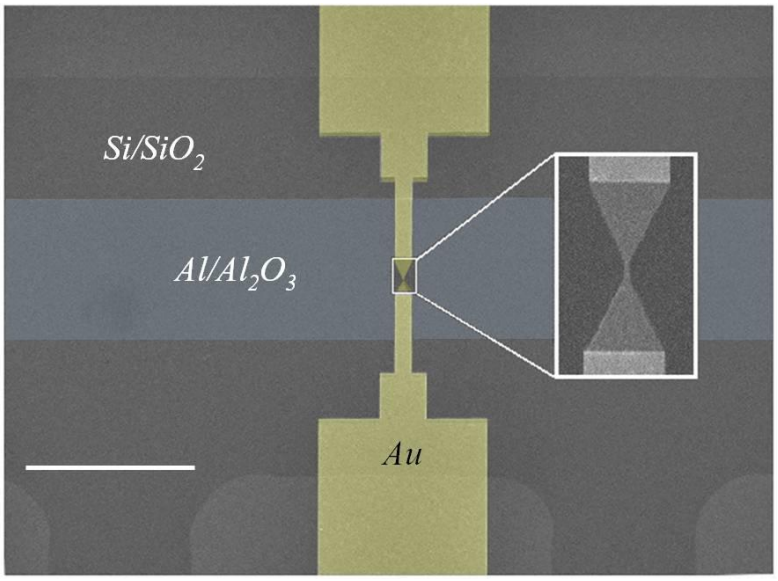

Figure 14: SEM image of the one gold nanowire on top of the Al back-gate. The gate across from left to right in false blue and the nanowire is composed of two layers (false yellow): one of 50nm thick and another 15nm as seen in the insert. The scale bar is 10µm.

2.1.3. Electromigration-induced Breaking Process

The breaking process is intended to create the final nanogap in the nanowires and both conducting electrodes (source/drain). For this purpose a feedback-controlled electromigration-induced breaking process is used at room temperature. The electromigration process consists on applying an electric potential difference to both sides of the nanowire until the gold maximum current density is reached (j_b = ~$5 \cdot 10^{12}$A/m^2 [37]), forcing gold atoms to drift under the action of electric wind forces caused by the strong local electric field and narrowing the nanowire. During the process, the conductance through the nanowire is monitored at any time and once the current dropped close to the universal single-channel conductance (G_0), the current flow is stopped. At this point, the devices are left untouched for a few hours during which the gold atoms reorganize

due to surface tension, finally creating stable gaps of a few nanometers and leaving no evidence of gold nanoparticles formation in the gaps [38].

The approach consists on a customized Labview program with which, in a feedback process, several parameters can be adjusted for the rupture of the nanowire. Figure 15 is an example of the electromigration-breaking process. The program increases the voltage across the nanowire while monitoring the current though it. Once the program detects that the percentage of change in current associated to the device decreases by certain amount, it recoils the voltage avoiding an abrupt break of the nanowire. This is achieved by monitoring the resistance of the wire during the breaking until it grows close to the quantum resistance associated to conduction to a single atom or one channel transmission $R_0 = 1/G_0 = h/e^2 = 25.8\ k\Omega$ [39].

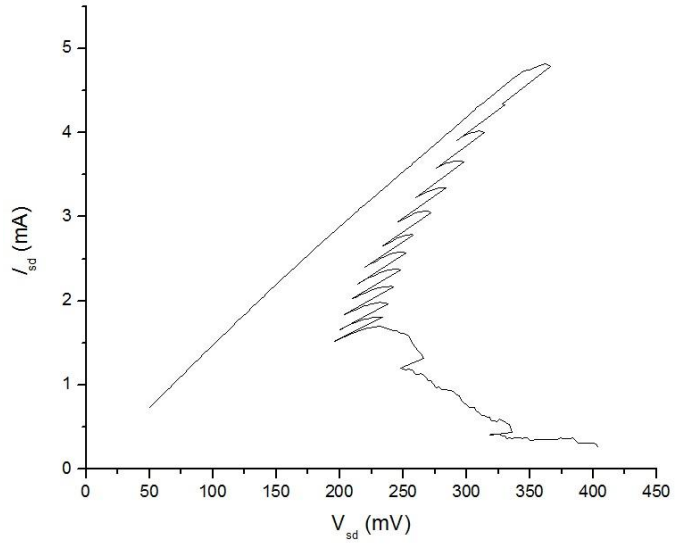

Figure 15: *I-V* graph of the feedback-controlled electromigration-induced breaking process at room temperature in the nanowire breaking box without solution of molecules. The process stopped when the program read a resistance through the nanowire approached the universal resistance, 25.8kΩ (38.7μS).

The percentage of breaking can be tuned at will and it is chosen to achieve a complete rupture in the shortest time possible. As this process is run at room temperature with the thermal energy associated to it, the optimized target resistance for nanowires (approximately 15 nanometer thick 50 nanometers wide) is ~5 to 25 kΩ, which, after approximately two hours, forms the desired gap. This process is carried in a homemade low-resistance breaking box which is connected to a 50 pin measuring BNC coaxial box for facilitating the access to the nanowires in the chips, previously wire bonded.

In about 30 seconds a nanowire is narrowed down to the edge of the rupture and leaved intact to complete the breaking process itself with help of the surface tension of gold. This technique allows the deposition of the solution of the molecules at room temperature once the gaps have formed, allowing them to sit in the gaps and avoiding damage to the molecules during the electromigration process and preventing the formation of gold nano-islands that could be mistaken by molecules in the measurements (*Section 2.3.*).

Figure 16 shows the statistics corresponding to the wires, prepared for the studies of the present thesis. Figure 16a represents the resistance of percentage of devices right after the feed-back breaking program and Figure 16b after approximately two hour of leaving the nanowires untouched. Nanowires display ~1GΩ resistance at room temperature translate into gaps of 1-3 nanometers.

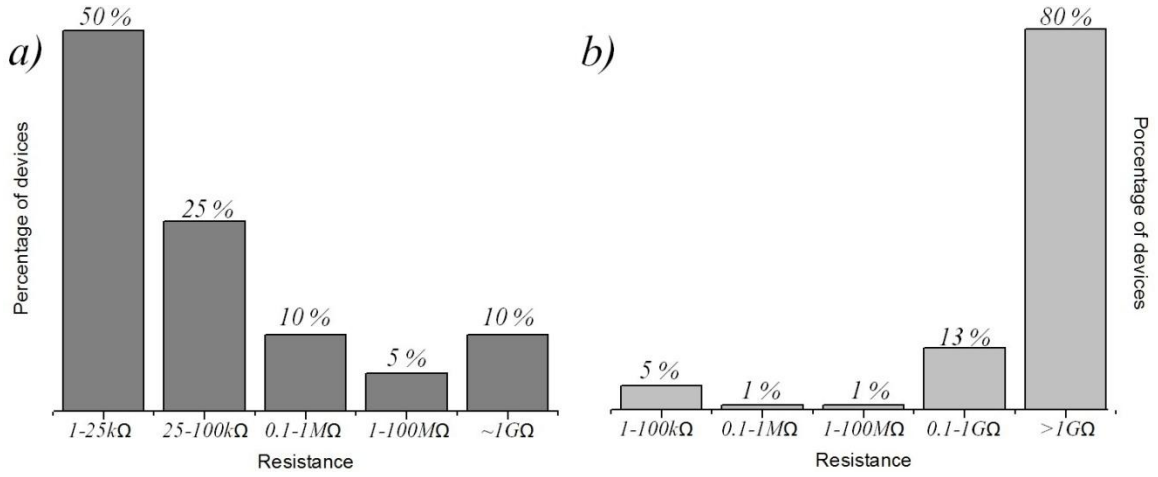

Figure 16: a) Graphic showing in columns the resistance and percentage of devices after the electromigration-induced breaking process without molecules during the breaking process. b) Graphic showing in columns the evolution of the nanogap in terms of resistance and the percentage of devices two hours after the electromigration-breaking process.

Figure 17 is an SEM image of a nanowire with inserts showing it before and after the feedback-controlled electromigration-induced breaking process at room temperature. This procedure finalizes with the creation of the source and drain electrodes of the single-electron transistor. Figure 18 shows a set of five nanowires on top the gate electrode in the final shape of one of our chips.

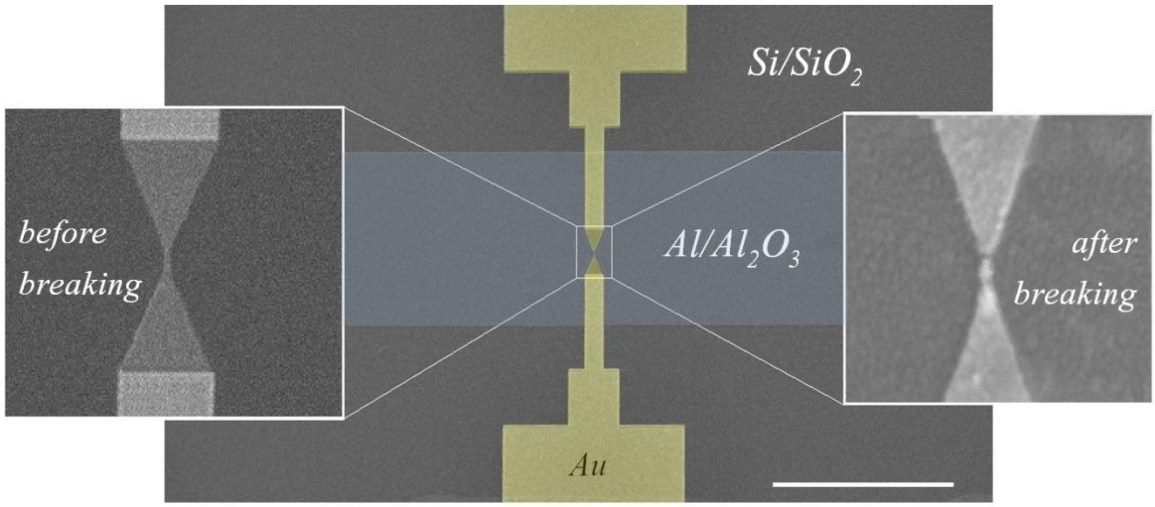

Figure 17: The single molecule junction. False color scanning electron microscopy (SEM) image of one of the SETs showing the gold nanowire on top of the Al/Al_2O_3 back gate. The insets show the thinnest part of nanowire before (left) and after (right) the feedback-controlled electromigration-induced breaking. Scale bar is 10μm.

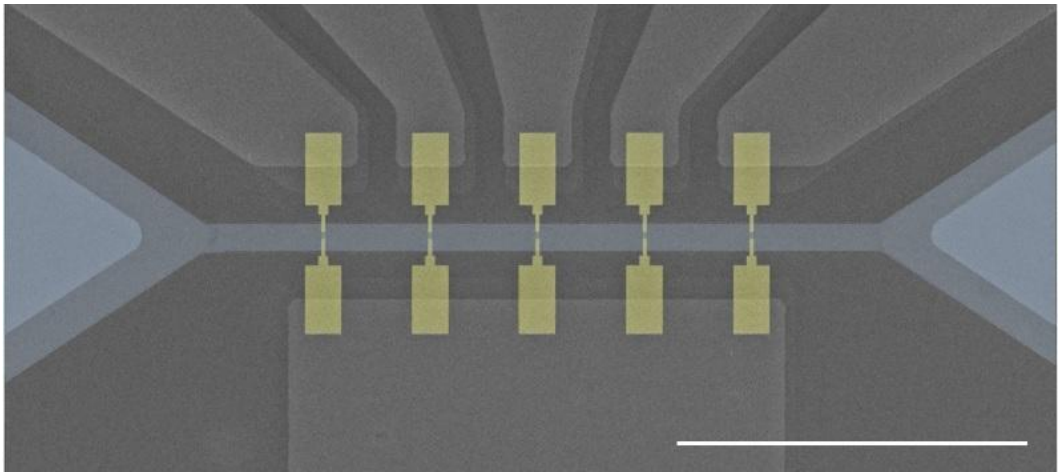

Figure 18: SEM image of finished SET devices. The back-gate electrode (aluminum 35nm, false blue) goes underneath of 5 nanowires (gold 15nm, false yellow). Scale bar is 100μm.

2.2. Control Experiments

Control experiments are necessary to ensure that SETs are properly fabricated and, once measuring, being able to claim that the response is derived from the target molecule. Therefore, the devices are checked for the proper creation of the gap by running *I-V* measurements through the tunnel junction and fitting them to the Simmons model (*Appendix B)* in order to get an approximation of the gap size. Figure 19 shows two *I-V* tunneling curves of our empty junctions and their fit to the Simmons model. The *I-V* curves measured fit in the model accounting for several different characteristic parameters of the conduction through the tunnel junction such as: the size of the gap, the cross section of the conduction wire and the work function of the metals configuring the electrodes. The broken nanowire in Figure 19a had a resistance of ~50 MΩ at low bias voltages and the fitting parameters that best account for the tunneling barrier in this case were: 50 nm^2 of current area, 1.6 nm for the length of the gap, 0.29 *eV* for the work function of the conducting metal and 0.40 in the ratio of asymmetry between the positive and negative bias. In a second nanowire, Figure 19b, the measured resistance was ~800 MΩ at low bias voltages and the fitting parameters were: 50 nm^2 of current area, 2.2 nm for the length of the gap, 0.30 *eV* for the work function of the conducting metal and 0.45 in the ratio of asymmetry. Although the cross section at the narrowest part of the nanowire was meant to be 50 nm wide and 15 nm thick, after the electromigration-induced breaking process (*Section 2.1.3.*) the gap can acquire a not uniform size and the effective shape of the lead can vary. For the tunneling curves in Figure 19, a cross-sectional area of 50 nm^2 fitted well the measurements.

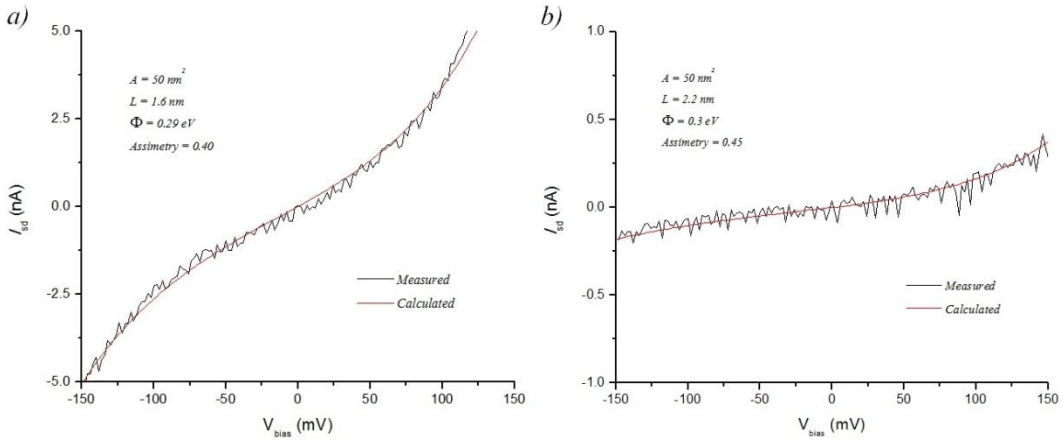

Figure 19: Tunneling current through gold nanogaps, black curves are the measure values and red curve the fittings to Simmons model. a) Fitting parameters in the Simmons model: cross sectional area = 50nm^2, length of the gap = 1.6nm, work function = 0.29*eV* and asymmetry = 0.40. The resistance for (a), at low bias, was ~50MΩ. b) Fitting parameters in the Simmons model: cross sectional area = 50nm^2, length of the gap = 2.2nm, work function = 0.3*eV* and asymmetry = 0.45. The resistance for (b), at low bias, was ~800MΩ.

These two empty junctions (resistances of 50 and ~800 MΩ) were tested for their evolution of I_{sd} vs. V_{sd} with temperatures from T = 80 to 260 K. In Figure 20a the junction with ~50 MΩ resistance shows an increase in current with temperature. This is probably produced by readjustments of the gold atoms with temperature which result in reducing the size of the gap, increasing the tunnel current. For Figure 20b, the junction with ~800 MΩ resistance shows no appreciable changes within the range of temperatures. Most importantly, these results show the absence of sharp features that could be mistaken by the transport excitations expected from molecules deposited in the gaps when the temperature is varied.

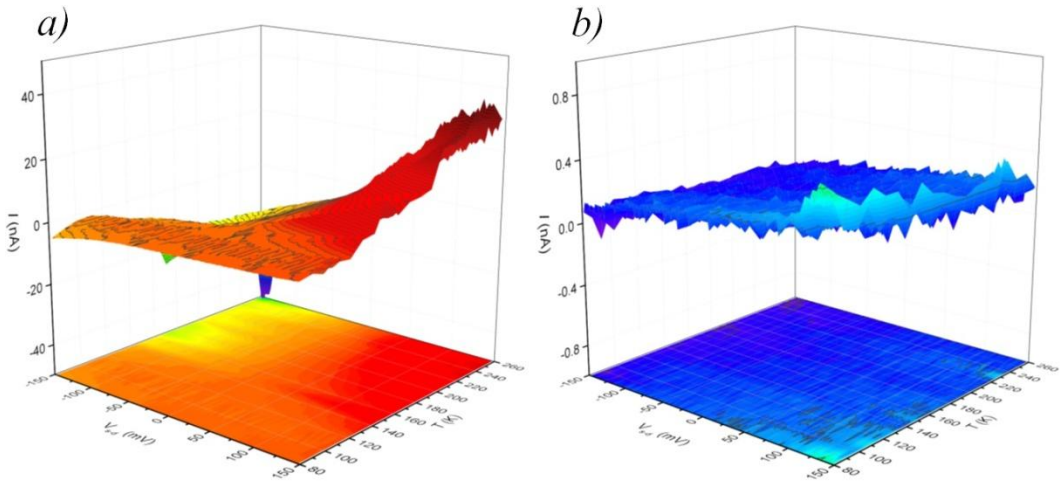

Figure 20: 3D contour-color plots of the evolution of the in the *I-V* curves through empty SET gaps with temperature. a) Evolution of a ~50MΩ tunneling resistance at low bias voltages. b) The same for a ~800MΩ junction.

Moreover, the devices are always checked for leaks between the source/drain and the gate electrode. The isolation between them is achieved by a thin (1 to 2 nm) Al_2O_3 layer which is fragile and sensitive to drastic electrostatic changes. These barriers are routinely characterized any time a new fabrication batch of SETs is obtained. An example of the breaking point of an aluminum oxide barrier between the conducting and gate electrodes is shown in Figure 21 with the current in the *y-axis* (logarithmic scale) and voltage in *x-axis*. Voltages above 5 to 6 volts are necessary to break the barrier, giving a safe gate voltage window of -3 to +3 V. The resulting leaks, after the break, are easily identifiable during the SET measurements where the rupture sometimes occurs unexpectedly while measuring due to an electrostatic discharge.

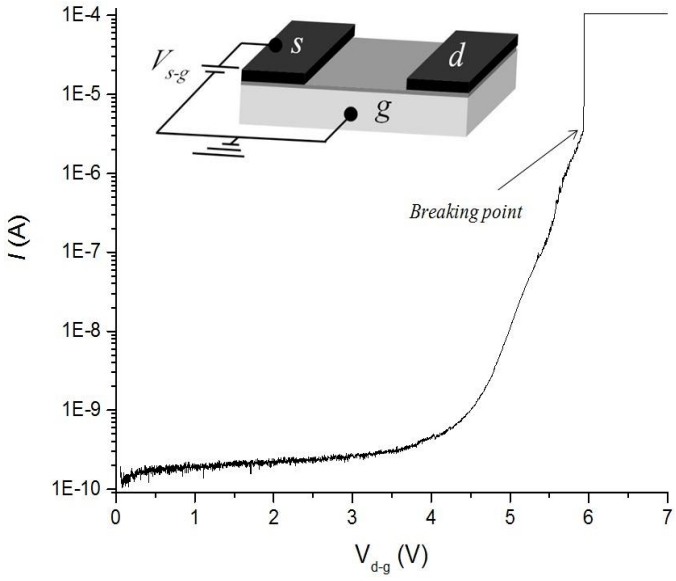

Figure 21: Log scale graph of the breaking point for a Al_2O_3 tunnel barrier between the aluminum oxide layer. The breaking point was found for several different devices at ~6V. The schematic of the circuit is given in the insert.

It is also important to verify that the small tunneling current between the source/drain leads and the gate is not compromised when varying temperature. To evaluate this, the tunnel current between the source and gate electrodes in several empty junctions was measured between liquid nitrogen temperatures and 260 K and the results in one of the devices displayed in Figure 22. Basically, the tunneling current is negligible (<< 0.1nA) when compared to the usual current through the molecular junctions reported in this work (which is typically of several nA [1-9]), and does not display any appreciable change with increasing temperatures.

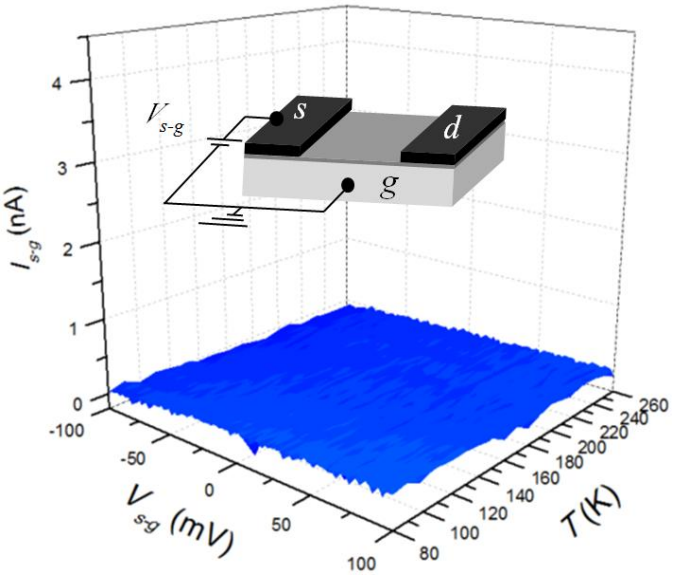

Figure 22: Tunnel current between the source and gate electrodes as a function of source-gate voltage V_{s-g} and temperature. The same result is obtained between the drain and gate electrode. The schematic of the circuit is given in the insert.

Nonetheless, it also important to check the temperature behavior in empty junctions and examine them upon changes in temperature. The results of one empty junction are shown in Figure 23 (similar results were observed in the other junctions examined). At all gates and temperatures (in the case of the empty junction up to 260K) the current through the empty junction remains negligible (I_{sd} < 0.1nA in all examined empty junctions) when compared to the current through the molecular device.

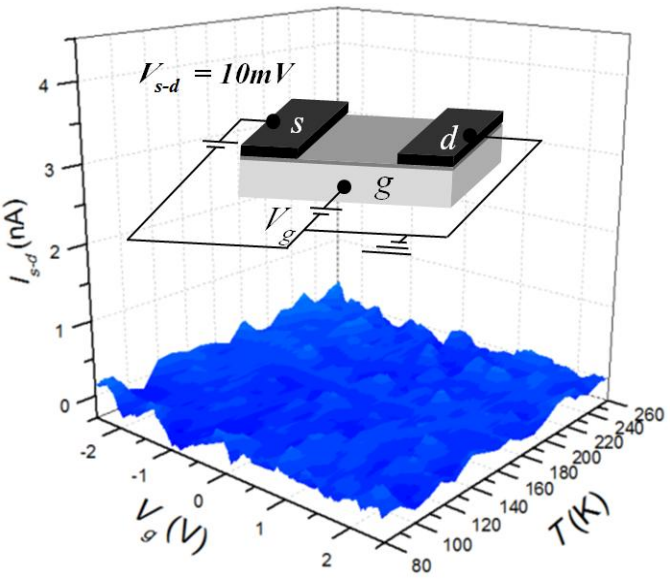

Figure 23: 3D plot of the evolution of the tunnel current through an empty junction vs. gate voltage as the temperature is increased from 80 to 220K for V_{sd} = 10mV. The schematic of the circuit is given in the insert.

Note that although the current magnitude in a molecular junction depends greatly on its coupling to the electrodes, it is always expected to be substantially larger than that flowing across an empty gap. But, most importantly, the absence of prominent features in the temperature and gate voltage responses of the empty junctions provides the distinct behavior observed in the molecular junctions a strong proof of their molecular origin.

2.3. Deposition of Molecules

Molecular deposition into the nanogaps of the SETs is as important as any fabrication step. In the past, there were methods where the transistors were introduced in the target molecular solution for a given period of time and then at low temperature the nanowires were broken expecting that a molecule in the vicinity would fall into the gap [28,30,35,36]. Now, with the breaking of the nanowires at room temperature the molecular solution can be deposited once

the gap is created and mount the devices into the probes with the molecules already bridging the gaps [38]. This increases the yield and makes this technique more efficient, which can be shown in *Chapter 4*, where the yield of finding a molecule with this technique was ~ 3.5%.

When depositing molecules on a device, first that device has to be characterized in a probe station to certify that the nanowires and gates have the expected resistance (~50 Ω for nanowires and ~100 Ω for gates) and that there is no current leak between drain and gates. After characterization, the chip is cut with a diamond cutter into the right dimensions of the chip carrier and cleaned with acetone, ethanol and isopropanol and then with O_2 plasma (Table 5 in *Appendix A*). Finally, the chip is wire bonded with the parameter of Table 13. The wire bonder is grounded and the bonding is started with drains, and after bonding all the nanowires, the process is finished with gates (first bonding on the chip carrier and then on the sample).

Immediately after the wire bonding, the chip is taken to the low resistance breaking box connected to the 50 pin measuring BNC coaxial box. It is very important that all the connections in the measuring BNC box are connected to ground to avoid any electrostatic potential difference that can blow the nanowires away. The connections for the chip carrier in the breaking box are inside a Teflon reservoir that can hold up to 3 mL of any solution. After the chip is placed in position, all the connections are floated one by one, finishing with the gate and drain connections, in that order. Then the chip is rechecked (~50 Ω for nanowires and ~100 Ω for gates) and finally the molecular solution is dropped in the reservoir and covered with a plastic lid. At that point, the electromigration-induced breaking process (explained in *Section 2.1.3.*) can

take place, if the breaking is to be done with molecules present. Otherwise, the molecules need to be deposited after the breaking process.

For the results in this thesis the chips were kept in the breaking box reservoir with the molecular solution for two hours after the breaking process. Then the chips were cleaned with ethanol and dried out with nitrogen gas.

2.4. Setup for Measurements

The transport measurements in our SET spectroscopy consists of *I-V* characterization performed in DC by applying bias voltage and measuring the current via the PreAmp of a Keithley 6430 sub-femtoamp remote sourcemeter, while a Keithley 2400 is used to gate the transistor (Figure 24a). Moreover, these measurements can be duplicated using a lock-in amplifier which measures the differential conductance (dI/dV). In this case the lock-in controls both bias and gate voltages as seen in Figure 24b. For the bias voltage the lock in applies an AC and DC signals which are added in a voltage divider to increase the resolution (10:1 for DC and 100:1 for AC) [28]. The gate voltage is controlled by one of the four outputs of DC in the back of the lock-in.

The output voltage in Keithley 6430 ranges from ±5 μV to ±210 V with a limit in current from 1 fA to 105 mA. Keithley 2400 has a resolution of ±5 μV. The lock-in SR830 can output ±10 V with 1 mV resolution in DC and the AC signal ranges from 1 mHz to 102 kHz with 5 V max output and resolution of 1 mV. All the power connections output from a low noise transformer isolating the building ground and letting the instruments to connect to a cleaner lab

ground. The acquisition of the data was driven by customized Labview programs through GPIB connections to a computer.

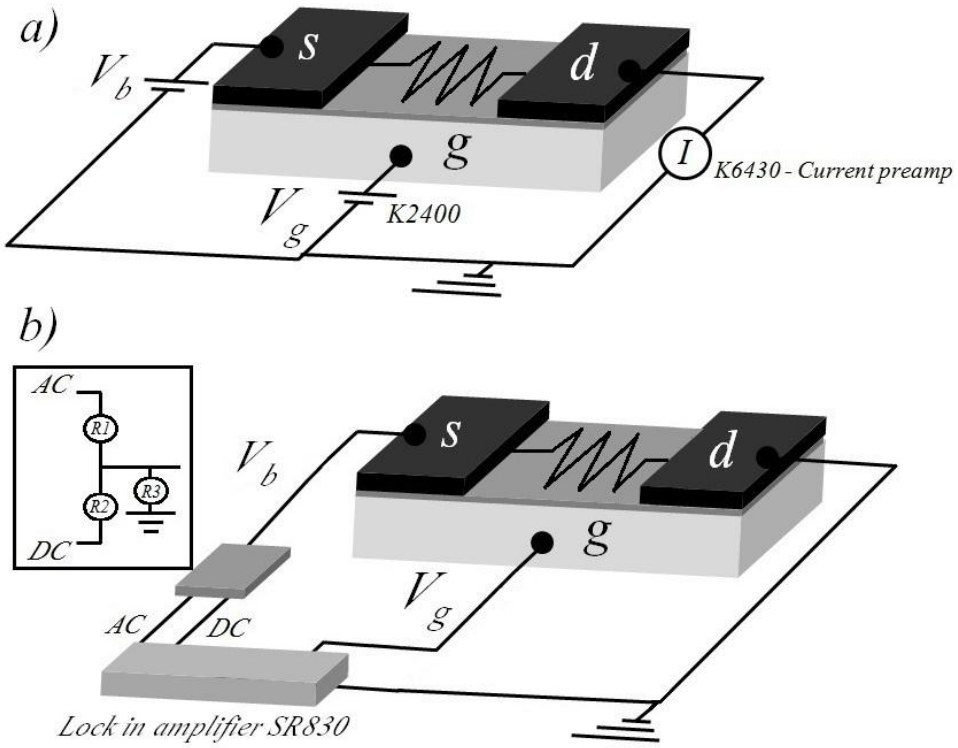

Figure 24: Measurement setups for a single-molecule (represented as a resistor) SET. a) Using a Keithley 6430 as current preamplifier and Keithley 2400 as gate voltage generator. b) Using a lock-in amplifier SR830 as current amplifier, bias voltage and gate voltage generator. Inset in b) shows the sum of two signals from the lock-in in a voltage divider before going into the circuit. R denominates resistor being R1 = 1MΩ, R2 = 10kΩ and R3 = 1kΩ.

The devices can be mounted on the sample holder of two of our low-temperature probes: the OXFORD ^{3}helium cryostat and a home-made dipping probe. The ^{3}helium cryostat was employed for characterization of our molecules at temperature down to 240 mK, while the dipping probe was used on a liquid nitrogen dewar for temperature-dependence measurements in the 80-260 K range. In these low-temperature probes the transistors are connected to a 50 pin connector (25 L and 25 O connections, for reference) getting into a measurement box.

The dipping probe was customized with a two-wire CERNOX thermometer (connected to O1 and O2 connectors in our probe) and a heater made by a 50 Ω Nichrome wire (connected to O3 and O4). Another Keithley 2400 was used to control temperature during the measurements, where the control current at the heater was increased in 0.1 mA steps, avoiding electric shock to the device. A Keithley 2000 was used for reading the resistance of the thermometer.

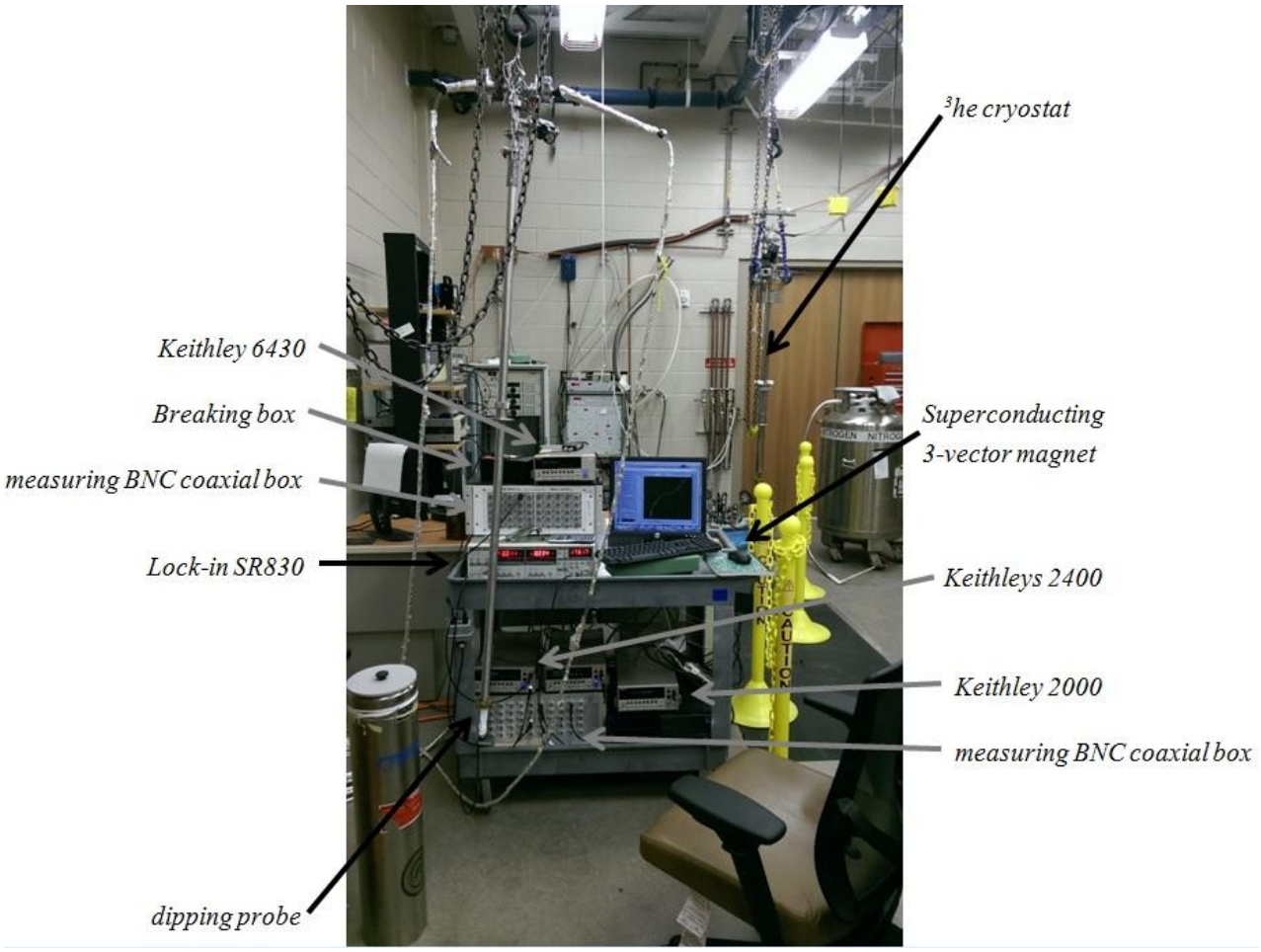

Figure 25: Mobile cart with all the setup for measuring molecules at low-T.

Figure 25 shows the transport measurements mobile cart (*Alvar's cart*) with all the necessary equipment. The cart transports a computer connected to 4 Keithley boxes and one lock-in amplifier, interconnected by two measuring BNC coaxial boxes, one connected to the breaking box and other connected to the probe. In front of the cart there is our dipping probe and behind these is our ^{3}He Oxford Instruments Heliox cryostat, next to our superconducting 3-D vector magnet.

CHAPTER 3:
TEMPERATURE-DEPENDENT SINGLE-LEVEL TUNNELING MODEL

3.1. Introduction to Temperature-dependent Transport

Understanding the electrical tunneling transport for temperature dependence characterization of molecular tunnel junctions allows studies of individual molecules in the presence of a gate voltage within a wide range of temperatures. It is typically observed in such systems a transition between a temperature insensitive regime, governing conduction at sufficiently low temperatures (usually below of 100-150 K), and a thermally-assisted transport regime, commonly displaying an exponential dependence with temperature (although this is not always the case with several observations of temperature-independent conduction close to room temperatures [10-22], or more complicated transport regimes particularly relevant in complex/large molecules, where hopping may become the dominant mechanism determining conduction [40-43]).

In general, the temperature-independent conduction in a molecular junction, dominant at low temperatures, is associated to coherent sequential tunneling between the transistor leads and the molecular level (e.g., HOMO/LUMO) involved in the single-electron transport. The exponential increase of current at high temperatures is usually associated to classical interaction processes involving molecular vibrations and/or polaron excitations of neighboring solvent molecules, i.e., inner- and outer-sphere reorganization processes, respectively, according to Marcus theory [44]. From the latter it follows fitting the temperature dependence to an Arrhenius law ($I = I_0 e^{-E_a/k_B T}$, where k_B is the Boltzmann constant and I_0 is a pre-exponential factor), to

extract the corresponding activation energy (E_a) associated to the excitation processes into play [45]. Although this is definitively the most likely scenario governing charge transfer in wet electrochemistry processes, where the presence of polar solvent molecules facilitates transfer of electrons, and for which Marcus theory was developed, its relevance is less clear in solid state ("dry") molecular junctions, where solvent molecules are absent.

Alternatively, a natural explanation for the transition between the two conduction regimes arises from the thermal broadening of the Fermi occupation distribution of electrons in the leads and its overlapping with the molecular level responsible for conduction through the junction. Only one work has shown how a single-level model accounting for the Fermi broadening can easily explain the temperature dependence of the current in the Coulomb blockade regime of an individual tercyclohexylidenes molecule bridged between the two bias leads of a three-terminal SET [9]. In that work, the temperature dependence for two gate voltages corresponding to having the molecule in the Coulomb blockade regime, and a few bias voltages, for which a clear transition from temperature-independent to exponential-dependent current was clearly observed. However, the temperature behavior of the conduction in the transport regime (i.e., when the molecular level lies within the conduction window of the transistor) was limited to a single voltage value (for which no temperature dependence was observed). In addition, in the molecule studied in that work the electronic density is expected to be delocalized within the junction, which could lead to complex interactions with the electrodes.

It was therefore necessary to expand such temperature-dependent measurements in individual molecules by: a) studying molecules that have been well characterized with other

techniques (e.g., SAM-based junctions), for comparative analysis; b) employing molecules where the conduction level is well localized within the molecule and properly isolated from the electrodes; and, c) performing experiments within a wide range of gate and bias voltages to study conduction in all possible transport regimes.

3.2. The Single-level Transport Model

In the simplest approximation, a molecular junction can be represented by the schematic diagrams shown in Figure 26, where the molecule, sandwiched between three electrodes (two in the case of SAMs), is represented by a discrete set of levels (with N representing the number of electrons in each level) separated from the electrostatic potential in the electrodes by tunnel barriers, as explained in *Chapter 1*. The molecular levels closest to the electrostatic potentials of the leads at zero bias are known as the HOMO (highest occupied molecular orbital, N) and LUMO (lowest unoccupied molecular orbital, $N+1$) levels and are well separated in energy (~1 eV), although energy renormalization effects could bring this value down to a few hundres of milli-electronvolts. The level closest to the Fermi energy of the electrodes governs the electrical conduction through the junctions for moderate bias potentials.

NOTE: For the temperature-dependent theory the name of the source and drain electrodes have been modified for right and left and the tunnelling rates as γ, instead of Γ used in Chapter 1.

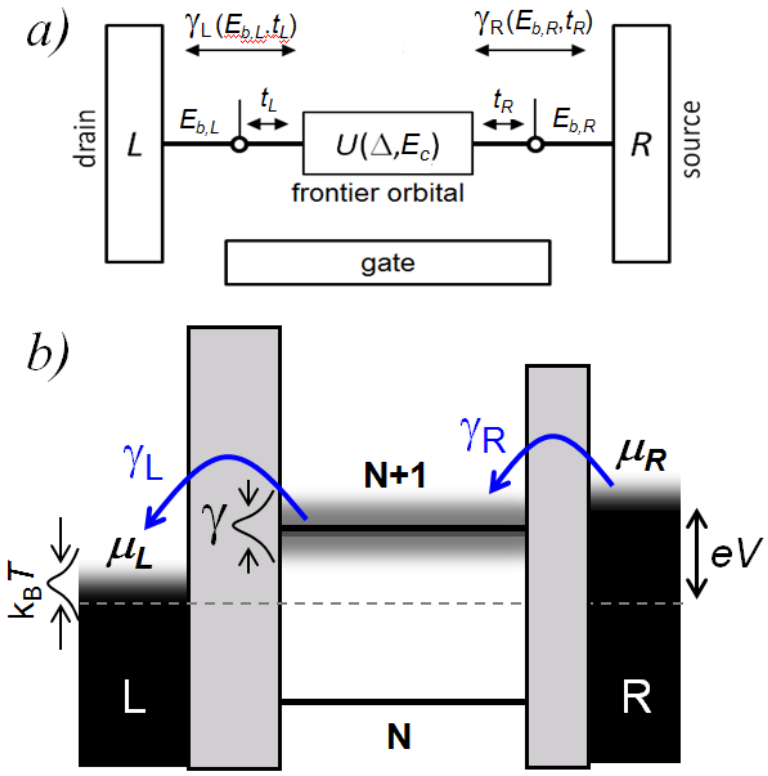

Figure 26: a) Schematics of the electrical coupling in SETs. b) Corresponding energy level alignment in a molecular junction composed of a molecule with multiple electrostatic levels sandwiched in between two electrodes (L, left: drain and R, right: source). $\gamma_{L/R}$ are the tunneling rates, $E_{b,L/R}$ are the binding energies, and $t_{L,R}$ are the intermolecular couplings between the molecule and left and right electrodes, with $\gamma = \gamma_L + \gamma_R$ being the level width. Δ represents the intramolecular level spacing, E_c the charging energy, and $\mu_{L/R}$ the electrostatic potentials of the leads.

Conduction through a molecule can, in principle, be understood in terms of sequential tunneling (either coherent or incoherent) involving one molecular level. In such a process, the electron tunnels from the source into the molecule at a rate γ_R and then out into the drain lead at a rate γ_L. The ratio between these rates and the characteristic intramolecular relaxation times determine whether the electron transport occurs coherently or incoherently. This means that if the electron spends sufficient time inside the molecule to significantly couple with internal/external degrees of freedom (*i.e.*, short relaxation time and short decoherence time

relative to the tunneling rates) then the process will become incoherent, with an associated loss of phase in the case of elastic tunneling, and loss of both phase and energy in the case of inelastic tunneling.

In wet electrochemical molecular charge-transfer processes, energy relaxation is usually facilitated by intramolecular vibrational modes and polaron excitations in the surrounding solvent molecules. In terms of Marcus theory, these are known as inner- and outer-sphere molecular reorganization processes, respectively, and are characterized by an activation energy arising from the classical energy barrier governing the process. At sufficiently high temperatures, these processes lead to an exponential increase of the charge transfer (accompanied by an Arrhenius law and incoherent tunneling). However, in the junctions discussed in this thesis, where the molecules are present in solid-state devices and charge transport is studied in the absence of solvent, outer-sphere reorganization processes do not likely play an important role in the electrical conduction through the junction. This is not necessarily the case in all SAM-based junctions, since even in the absence of solvent molecules, neighbouring molecules can play this role, particularly when considering complex molecules with high degrees of polarizability.

It can be expected that inner-sphere reorganization will always be important, and can be related to intra-molecular vibrational modes with energy usually below a few tens of milli-electronvolts (<30 *meV*), which is smaller than or comparable to other energy scales relevant to the conduction process, such as thermal broadening at high temperatures. Thus, when only one level participates in the conduction though the junction (which may be the case in many molecular junctions), the vibrational modes can be formally incorporated into an effective temperature-dependent level broadening (the higher the temperature the more vibrational modes

will be sampled), which means that it is reasonable to still treat the transport process with simple single-level transport models.

Note the different causes of level broadening, which can be separated into two main contributions: i) broadening due to the coupling of the molecule to the electrodes, $\gamma = \gamma_L + \gamma_R$, and, ii) broadening arising from the coupling of the electron to other degrees of freedom of the molecule, γ_0. Of course, this is just a simplification (virtual transitions to high-energy molecular states take place during the conduction process, leading to renormalized parameters) and should be taken as such. However, this picture can be justified from a more fundamental calculation involving a non-equilibrium quantum mechanical treatment of the response of the molecule to its coupling to the leads. When a single energy level is active in the molecule, and the coherent interactions between electrons in the molecule and those in the leads are negligible, the non-equilibrium expression for the current reduces to an expression similar to the Landauer-Buettiker formula [46], namely,

$$I = \frac{2q}{h}\int dE \left[f\left(\frac{E-\mu_L}{k_BT}\right) - f\left(\frac{E-\mu_R}{k_BT}\right)\right] Tr\left\{\frac{\gamma_L(E)\gamma_R(E)}{\gamma_L(E)+\gamma_R(E)} Im[G^r(E)]\right\} \qquad (3.1)$$

where $f(x) = 1/(e^x + 1)$, μ_L and μ_R are the chemical potential at the leads, $\gamma_L(E)$ and $\gamma_R(E)$ are the partial level widths due to the coupling to right and left leads, respectively, and G^r is the molecule's single-particle retarded Green's function, which contains a self-energy that takes into account the coupling to leads and to other degrees of freedom as an imaginary part, namely, a total level width. In fact, this has been the starting point of several successful theoretical descriptions of molecular electronic transport experiments [47,48].

As well, there may be other processes playing important roles in the transport through solid-state junctions, such as intermolecular interactions or electrostatic potential changes due to electron charging or image-charge effects [49], among others. Some of these could be incorporated into simple single-level transport models. As shown below, for a single-level junction system the coherent and incoherent tunneling treatments provide identical predictions of the current at all temperatures, provided that one incorporates into the level broadening the two effects discussed above concerning outer-sphere reorganization and vibrational modes.

Therefore, even a single-level coherent transport model can explain the exponential thermal enhancement of the conductance through a molecular junction without the need to invoke Marcus relaxation processes, since the temperature dependence of the conductance naturally arises from the thermal broadening of the energy of the electrons in the leads (see, *e.g.*, the work by van der Zant *et al.* [9]). In other words, a transition between a plateau-like to temperature-dependent conductance in a molecular junction should not be immediately taken as a sign of inelastic incoherent processes. Sequential tunneling may well be coherent and one simply cannot distinguish them when transport involves a single energy level without considering the ratio of the relaxation rates involved.

3.2.1. Capacitive Couplings of the Frontier Orbital with the Electrodes

The transition between coherent and incoherent tunneling is determined by the tunneling rates in and out of the molecule (when compared with the intrinsic molecular relaxation rates). As explained by Moth-Poulsen and Bjørnholm in their review article [50], the tunneling rates for a complex molecule usually depend on the strength of the bond of the molecule to the electrodes,

$E_{b,i}$, and on the intramolecular coupling, t_i, between the electrode and the molecular frontier orbital (Figure 26a), and are, in general, difficult to engineer. The molecule-electrode couplings result in broadening of the molecular levels ($\gamma = \gamma_L + \gamma_R$). The capacitive couplings of the frontier orbital with the electrodes determine the electric potential drops at both sides of the active conduction unit (V_L and V_R) and provide asymmetry to the junctions when $L_L \neq L_R$. This asymmetry is parameterized by the dimensionless division parameter $\eta = V_R/(V_L + V_R)$, which gives the ratio of the voltage drop between the molecule and the right electrode with respect to the total voltage drop in the junction.

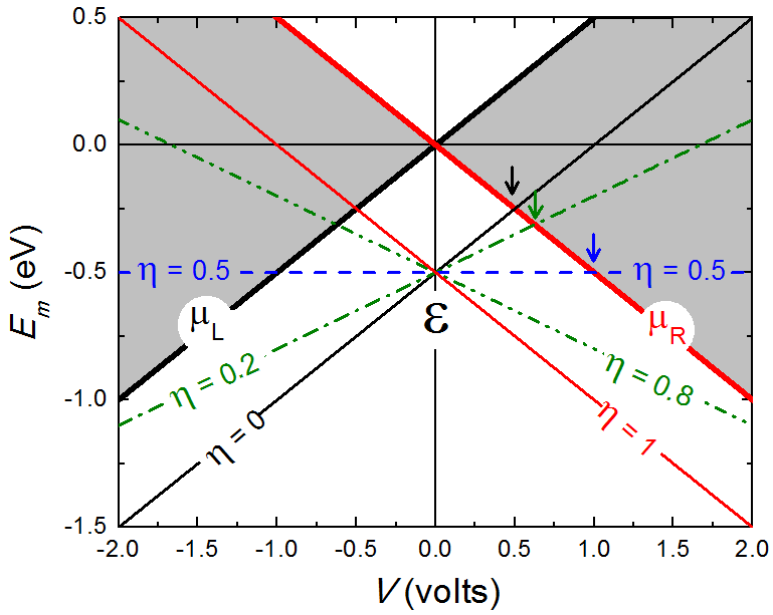

Figure 27: Voltage dependence of the energy of the molecular frontier orbital for different values of the voltage division parameter η, with respect to the electrochemical potentials μ_L and μ_R of the electrodes in the junction. ε is the zero-bias energy offset between the molecular orbital and the electrodes. The arrows show when the molecular level enters the conduction window (grey areas).

The molecular frontier orbital follows the average effective potential within the molecule and its energy can be expressed as $E_m = \mu_R(V) + \varepsilon + \eta qV$, where ε is the zero-bias energy offset between the molecular orbital and the electrodes, q is the electron charge, and μ_R is the electrochemical potential of the right electrode. The behaviour of E_m, μ_L and μ_R with the bias potential V is shown in Figure 27 for different values of η. For η ~0.5 the energy of the level remains constant as the bias potential is increased, while for η ~0 or ~1, the molecular level closely follows the right or left potentials, respectively.

3.2.2. Thermal Broadening of the Fermi Occupation Distribution

Thermal broadening of the energy of the electron in the leads also greatly affects conduction through the junction and needs to be taken into account. When a bias potential is applied, two distinct Fermi distributions need to be used, one for each lead:

$$f_{L,R}(E) = \frac{1}{1+exp\,[(E-\mu_{L,R})/k_BT]} \tag{3.2}$$

In the case of a single conduction level, the electrical current can be calculated by solving the rate equations for each side of the molecule. In the limit of very small broadening ($\gamma \ll k_BT, |\varepsilon|, |\mu_L - \mu_R|$) one obtains the following electrical current expression (see detailed discussion in the *Appendix C*) [47,51]:

$$I_{L,R}(E) = (-q)\frac{\gamma_{L,R}}{\hbar}(f_{L,R}(E) - N) \tag{3.3}$$

where N is the occupation number or average number of electrons in the steady state. By definition, in this state there is no net transfer of electrons in or out of the junction (*i.e.*, $I_L + I_R = 0$), from which one can extract an expression for N:

$$N = \frac{\gamma_L f_L(E) + \gamma_R f_R(E)}{\gamma_L + \gamma_R} \tag{3.4}$$

Substituting this functional for *N* in *Equation 3.3* one obtains the steady-state current through the junction (without taking into account the spin) as

$$I = I_L = -I_R = \frac{2q}{\hbar}\frac{\gamma_L \gamma_R}{\gamma_L + \gamma_R}[f_L(E) - f_R(E)] \tag{3.5}$$

Note that this treatment accounts for sequential tunneling of the electron from one of the leads and into the molecule and further into the opposite lead and is incoherent in nature. In other words, the rate equations formulation assumes that the electron's phase memory is completely lost once it tunnels into the molecule. That can only happen through relaxation processes, purely elastic in the case of a single level (no other levels to transit into), but possibly even inelastic.

Apart from this, the first conclusion that one can extract from *Equation 3.5* is that current will only flow through the junction if a molecular level lies between the electrochemical potentials of the left and right electrodes (*i.e.*, within the conductance window) explained in *Section 1.2*. Of course, this approximation fails when the level width surpasses such energy separation, since it will partially lie out of the conductance window. In other words, the current will not increase indefinitely by simply increasing the level width (*i.e.*, increasing the coupling to the electrodes). On the contrary, the resistance has a quantum mechanical limit, which for a single transport channel translates into a universal quantum of conductance, G_0, as originally predicted by Landauer [39].

3.2.3. Broadened Density of States

Interestingly, it is possible to relax the condition $\gamma \ll k_B T, |\varepsilon|, |\mu_L - \mu_R|$ and incorporate the effect of a finite level broadening into the rate equation calculation by introducing a broadened density of states (DOS) in the shape of a Lorentzian centered at the energy level ε,

$$D_\varepsilon(E) = \frac{\gamma/2\pi}{(E-\varepsilon)^2+(\gamma/2)^2} \tag{3.6}$$

The result is

$$I = \frac{q}{h}\int_{-\infty}^{\infty} dE\, D_\varepsilon(E)\frac{\gamma_L\gamma_R}{\gamma_L+\gamma_R}[f_L(E) - f_R(E)] \tag{3.7}$$

This expression matches exactly the one derived by Jauho, Wingreen, and Meir in 1993 [46] using a fully coherent formulation based on the Keldysh Green's function formalism (see *Appendix C* for a detailed analysis). This may seem remarkable but for a single channel and a single level in the molecule, interference plays no role in the electron conduction through the molecule. As a result, coherent and incoherent sequential tunneling cannot be distinguished at a formal level. Both models provide the same level of accuracy in describing transport at low bias through a single level, as was verified in a pioneer experiment by the Saclay group [52]. While in the coherent derivation of *Equation 3.7* the level broadening is entirely given by the sum of the partial broadenings due to leakage through the leads ($\gamma = \gamma_R + \gamma_L$), in the incoherent case one can introduce an additional source of broadening unrelated to leakage, namely, $\gamma = \gamma_R + \gamma_L + \gamma_0$. Other than that, the two results are formally identical at any temperature or bias voltage.

3.2.4. Landauer Formalism

Landauer derived an equation similar to *Equation 3.7* under the assumption that the entire system (leads and "molecule") were one dimensional. Now we know that the validity of *Equation 3.7* does not depend on the spatial dimensions, but rather on the number of channels involved. Namely, it is a correct description only in the case of a single channel in and out of the molecule on each lead. The derivation presented here is also only valid in the case of spinless charge carriers. It is straightforward to extend it to include spin ½ carriers: provided that coherence does not extend beyond the molecule, both rate equation and fully-coherent formulations yield again identical results. When the charging energy is strong and forbids double occupancy of the molecular level (that is, $E_c \gg k_B T, |\mu_L - \mu_R|$, which is typically the case for solid-state molecular junctions), the expression for the current becomes

$$I = \frac{2q}{h} \int_{-\infty}^{\infty} dE\, D_\varepsilon(E) \frac{\gamma_L \gamma_R}{\gamma_L + \gamma_R + \Gamma_{0\to 1}} [f_L(E) - f_R(E)] \tag{3.8}$$

where

$$\Gamma_{0\to 1} = \int_{-\infty}^{\infty} dE\, D_\varepsilon(E)\, [\gamma_L f_L(E) + \gamma_R f_R(E)] \tag{3.9}$$

In the linear regime and when the molecular level falls within the bias voltage window, $\Gamma_{0\to 1} \approx \gamma_R + \gamma_L$ and one finds that the current matches closely that of *Equation 3.7*, with the prefactor of 2 cancelling out. Notice that, in the opposite limit, when charging energy is weak and double occupancy is permitted, one can simply adopt *Equation 3.7* and account for spin degeneracy in the conduction process by multiplying the r.h.s by a factor of 2 (see *Appendix C* for details).

Thus, *Equation 3.7* can be formally taken as a good approximation to describe conduction through a molecular junction at all temperatures provided that: i) Electrical conduction through the junction is mainly governed by a single level (no transitions to high-

energy states); and, ii) that intra- and inter-molecular interactions can be incorporated into the level width (elastic processes). These conditions are likely to be applicable to solid state molecular junctions, where interaction with solvent molecules is not possible and Marcus-like energy relaxation processes are unlikely.

Moreover, it is easy to see from *Equation 3.7* that at low temperature ($f_L(E) - f_R(E) = 1$ if $\mu_L < E < \mu_R$, $= 0$ otherwise) and low bias ($\mu_L \sim \mu_R$), the maximum conductance (occurring when the energy level coincides with the average electrochemical potential, $\varepsilon = \mu$) will be

$$G_{max} = \frac{I}{V} = \frac{q^2}{h}\frac{4\gamma_L\gamma_R}{(\gamma_L+\gamma_R)^2} \tag{3.10}$$

coinciding with the universal conductance $G_0 = \frac{q^2}{h}$, if the two rates are equal ($\gamma_L = \gamma_R$), for the spinless case.

As a side note, one can break up the Landauer conductance into two contributions, since

$$G^{-1} = \frac{h}{q^2 M}\frac{I}{T} = \frac{h}{q^2 M} + \frac{h}{q^2 M}\frac{I-T}{T} = G_C^{-1} + G_T^{-1} \tag{3.11}$$

with M representing the number of channels and the characteristics of the junction (*Equation 3.8* when $\gamma_L \neq \gamma_R$). This is convenient in order to separate the contact resistance (G_C^{-1}) from the tunneling resistance (G_T^{-1}) in a molecular junction, and particularly relevant for AC impedance transport measurements, where one can distinguish experimentally from capacitive and resistive contributions in the transport through the junction [53].

An interesting exercise within the context of the discussion is to solve the asymptotic limit of *Equation 3.7* at high temperatures. To be more explicit when $\gamma \ll |\varepsilon| \ll k_B T \ll qV$ (*Appendix C* for detailed derivation). In this case, *Equation 3.7* reduces to:

$$I = \frac{2q}{\hbar}\frac{\gamma_L\gamma_R}{\gamma_L+\gamma_R}\left(\frac{qV}{k_B T}\right)e^{-\varepsilon/k_B T} \tag{3.12}$$

The current in this case shows an activation behaviour, with the "activation energy" ε being the offset between the energy level in the molecule and the Fermi energy in the leads. Note that a similar behaviour is expected from classical Marcus charge transfer processes, for which the activation energy has a completely different origin (described in *Sections 3.1. and 3.2.*).

The activation energies arising from these two very different mechanisms may display different dependencies with the electric potentials applied to the junction, which therefore become powerful sampling tools to discern its origin. From *Equation 3.12* it follows that the activation energy ε would decrease in increasing the bias voltage, as the electrostatic potential of the lead approaches the molecular level. This does not need to be the case in, *e.g.*, polaron-assisted conduction, where polarization of neighbouring molecules may be affected by the applied bias in intricate ways, resulting from its direct effect on the polaron dynamics.

3.2.5. Coherent versus Incoherent Tunneling

Figure 28 shows tunneling calculations using *Equation 3.5* and *Equation 3.7*, to solve for the electrical current through a single molecular level described with the following characteristic parameters: $\varepsilon = 0.4$ eV, $\eta = 0.5$, $V_G = 0$, and $\gamma_L = \gamma_R = 1\ meV$ (in Figure 28a-c) and 10 *meV* (in Figure 28d) and with different bias voltages: $V \in$ 400 - 700 mV. As can be clearly seen, there are two distinct regimes: decaying and saturated currents. The temperature where there is a transition between the two regimes (namely, the inflexion where the plateau starts to develop) depends on the bias voltage: the lower the bias the higher that transition temperature is (compare Figures 28a-c). The same correspondence is observable for the slope in the thermally activated regime. As determined from *Equation 3.12*, the "activation energy" decreases with increasing

bias (since the separation ε between the molecular level and the electrochemical potential of the leads decreases with increasing bias).

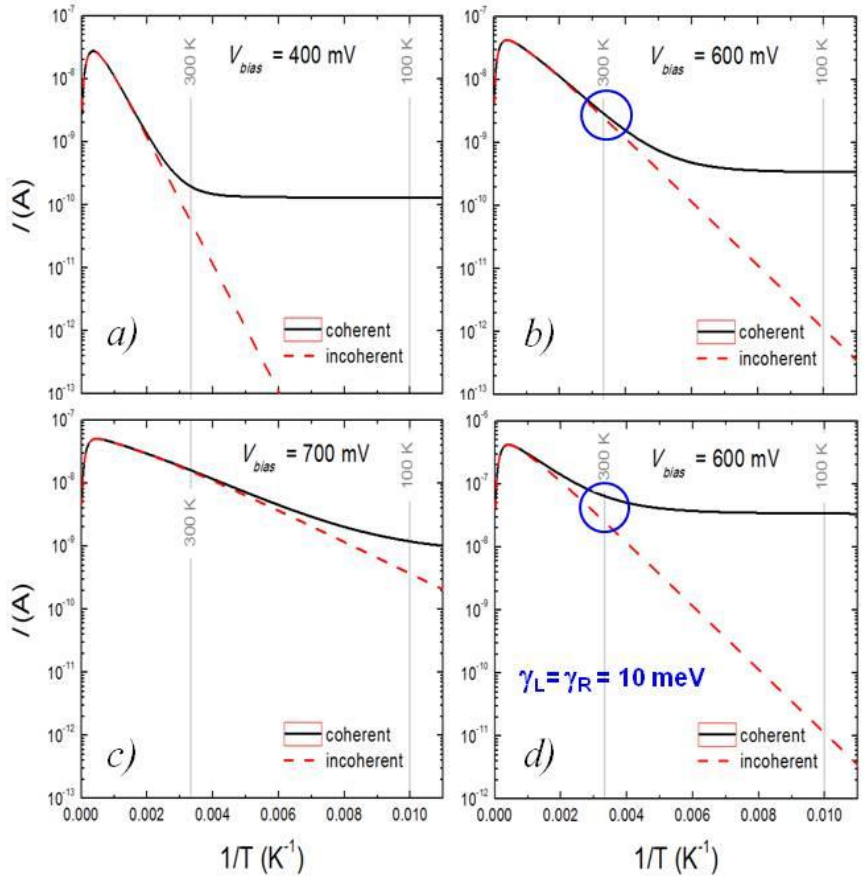

Figure 28: The electrical current through a single-level molecular junction as expressed by *Equation 3.7* (coherent, broadened molecular level) and *Equation 3.5* (incoherent, zero-width molecular level). The parameters used in the calculations are ε = 0.4*eV*, η = 0.5, V_G = 0, and $\gamma_L = \gamma_R$ = 1*meV* for (a-c) and $\gamma_L = \gamma_R$ = 10*meV* for (d), which are typical values in the molecular junctions studied in this work. The plateau at low temperatures is a direct consequence of the broadening of the molecular level as given by *Equitation 3.6*, which sets a maximum for a conductance at low temperatures.

In addition, one can observe that increasing the level width smears out the difference between the two regimes (compare Figure 28b and 28d). Important for the discussion is the fact that one can explain temperature-dependent electrical conductance in a molecular junction with the same functionality (exponential) and within the common temperature range of existing

experiments without the need of a thermal activation derived from Marcus-like energy relaxation processes in the molecules (also possible but less likely in many solid state junctions).

Indeed, this approach has been successfully employed to explain the temperature dependence of the conductance through an individual sulfur end-functionalized tercyclohexylidene molecule in a SET device [9]. In that case, the width of the molecular level had to be adjusted for different bias voltages, from a few *meV* at low bias up to 30 *meV* as the system was approached into resonance for larger bias. As discussed above, this effect can be understood in terms of a broadening of the molecular level width as a result of internal molecular vibrations excited by the increasing current when the system is brought closer to resonance.

CHAPTER 4:
TEMPERATURE-DEPENDENT TUNNELING ACROSS SINGLE-MOLECULE JUNCTIONS

4.1. Ferrocene Connected to Molecular Junctions

The molecular junctions measured were formed by S-$(CH_2)_4$-Fc-$(CH_2)_4$-S (Fc:ferrocene) molecules (*Section 1.5.*). The three-terminal SETs were fabricated following the instructions in *Chapter 2*. Figure 29 reflects the schema of the target molecule bridging the two gold leads on top of the aluminum gate electrode in one of our SETs. For depositing the molecules, during self-rupture of the wires, the chips were immersed in a 1 mM solution of $AcS(CH_2)_4Fc(CH_2)_4SAc$ in 20 mL toluene and 5 mL methanol along with 10 mg of n-Bu_4NCN. Where the n-Bu_4NCN in this toluene/methanol mixture deprotects the thioacetate mildly [40,54]. Finally, the devices were mounted in the low temperature dipping probe and cooled down to liquid nitrogen temperatures.

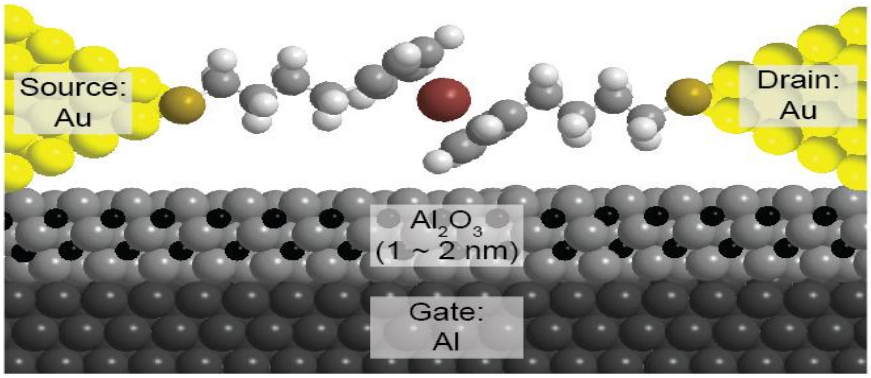

Figure 29: Schematic of a S-$(CH_2)_4$-Fc-$(CH_2)_4$-S molecule bridging the nanogap between two gold leads (source/drain electrode) on top of an Al/Al_2O_3 back-gate.

A total of 322 devices were measured, 60 of them (~19%) gave appreciable conduction of which 36 (~11%) showed gate dependence behavior. Out of these, 11 junctions (~3.5%)

presented electric transport characteristic of molecules, although some of them were too unstable to be measured, with molecular conformational changes as the most possible cause for device instability, and in others the molecular charge degeneracy points lied out of our gate range (-3 V to +3 V).

Out of the molecules which show evidence of Coulomb blockade, two molecules were stable enough for studies as a function of temperature (80-220 K in one case, and 80-250 K in the other case), displaying addition energies above $\Delta\varepsilon$ ~150 *meV*, with two or three degeneracy points characteristic of several other Fc-based molecules measured in our lab. The motion of the degeneracy points with magnetic field were studied in the same molecules at sub-Kelvin temperatures (Figure 30) allowing the determination of the oxidation states of the Fc, which are usually found to transit from Fe^{3+}(S=1/2) to Fe^{2+}(S=0) and Fe^{+} (S=1/2) within the measuring range of gate voltage.

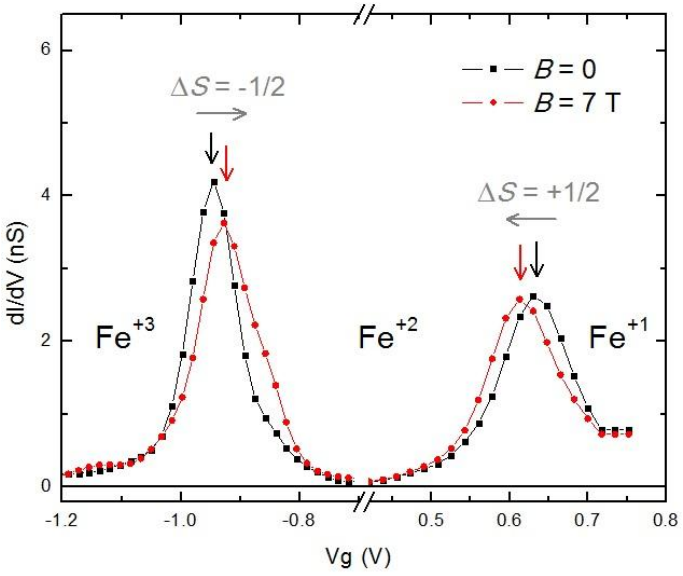

Figure 30: *dI/dV* vs V_g measured at T = 4K and V_{bias} = 10mV with and without a 7 Tesla magnetic field applied to another ferrocene molecule.

4.2. Charge Transport Measurements

Figure 31a shows a contour color-code diagram of the differential conductance (*dI/dV*) of the molecule at 80 K in the following ranges of bias and gate voltages: V_g (-2.5,+3.5 V) and V_b (-150,+150 mV). Closed diamonds characteristic of Coulomb blockade are clearly observed, with two degeneracy points at V_g = +0.25 and +2.5 V, and a third one lying outside the gate voltage window (V_g ~ -3.5). The corresponding characteristic addition energies are $\Delta\varepsilon$ ~180 and 110 *meV*, as observed from the crossings of the respective excitations in bias voltage. The ratio for the capacitive coupling between the ferrocene and the electrodes is: $C_g : C_s : C_d = 1 : 11 : 13$, with a gate coupling parameter of β ~ 0.05. A subsequent measurement of the same junction, after a fist cycle of temperature measurements, showed the degeneracy points displaced slightly to lower gate voltages.

Figure 31b shows the corresponding electrical current as a function of gate voltage for different bias voltages at 80 K. The two degeneracy points appear now at V_g = -0.3 and +1.7 V. As we show later from the results of the fittings, the addition energy associated to the transition between these two states had increased to $\Delta\varepsilon$ ~140-160 *meV*, with a gate coupling parameter changed to β ~ 0.07, which can be associated with a conformational adjustment of the molecule within the junction [55]. This configuration did not change again while performing the temperature dependent measurements.

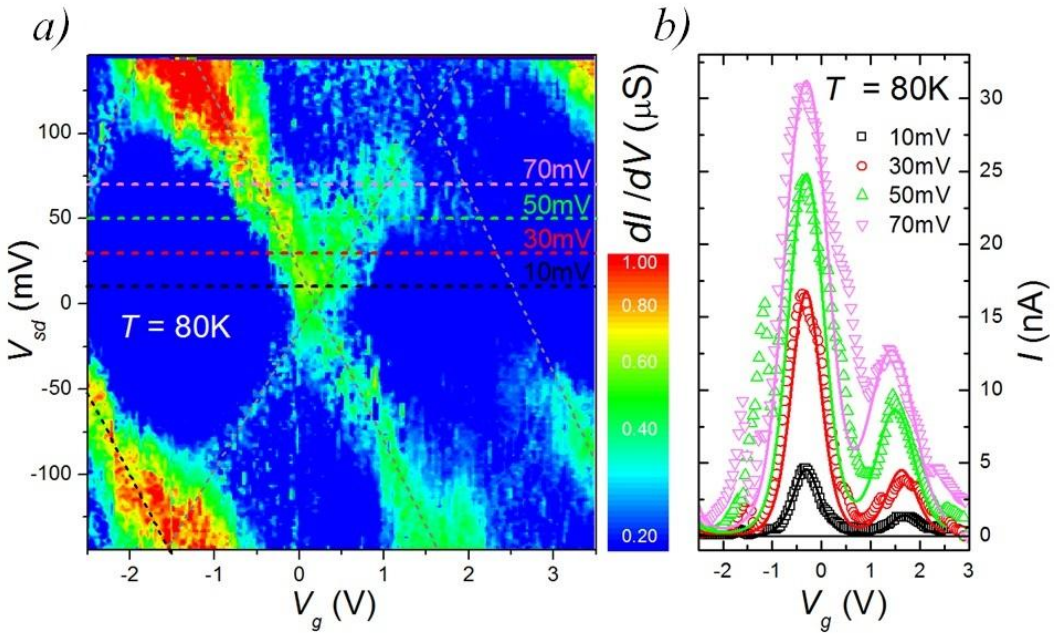

Figure 31: a) Differential conductance of a junction with S-$(CH_2)_4$-Fc-$(CH_2)_4$-S at T = 80K. Differential conductance (*dI/dV*), color-code, through the SET as a function of V_{sd} and V_g. The grey dashed lines indicate the main resonant excitations, crossing at two visible charge degeneracy points at V_{sd} = 0 (i.e., V_g = 0.25 and 2.5V) and separating the Coulomb blockade areas. A third charge degeneracy point is estimated to lie around -3.5V. b) Current vs. gate voltage for four different bias voltages (10, 30, 50 and 70mV). Symbols represent experimental values and solid lines are fits to the single-level tunneling transport model *Equation 3.7* using the parameters given in Table 1. The color code corresponds to the horizontal dashed lines in panel (a). The molecule changed its conformation within the SET electrodes between both measurements resulting in a shift in the position of the degeneracy points (new positions: V_g = -0.3 and 1.7V).

Another interesting characteristic that can be extracted from the spectroscopy measurement in Figure 31 is the similitude between the opposite slopes of the transport excitations, which symbolize the nature (in this case symmetric) of the capacitive coupling of the molecule with the left and right electrodes, respectively. The observation is consistent with the high symmetry of our molecules, with equal numbers of carbon groups (4) at both sides of the Fc unit, and agrees with previous observations in this family of ferrocene-based molecules [33], and explained in *Section 1.5*.

4.3. Temperature-dependent Transport Measurements

Figure 32 shows a 3D plot of I vs. V_g as a function of temperature for a bias voltage of 10 mV (basically a cut of the differential conductance plot in Figure 31a by the line representing V_b = 10 mV). The data was collected as the gate voltage was continuously swept for four different bias voltages for each temperature, and the process repeated at different temperatures from 80 to 220 K. Figure 33 is the corresponding theoretical plot using the single-level model described in *Chapter 3* using *Equation 3.7*. These results allow following the behavior of the current when changing the temperature within the full range of gate voltage, which enables the understanding of the tunneling conduction through the junction at all transport regimes, including the Coulomb blockade regimes, the charge degeneracy points and the transitions regimens. It is clearly appreciable the opposite temperature dependencies of the current in the Coulomb blockade regimes and the charge degeneracy points. The conduction at gate voltages corresponding to the respective degeneracy points decreases as the temperature increases (follow red arrows in the 3D data and its projection in the lower V_g-T panel in Figure 32). On the other hand, in the Coulomb blockade regimes (blue arrows) the current increases with an exponential trend as the temperature is raised.

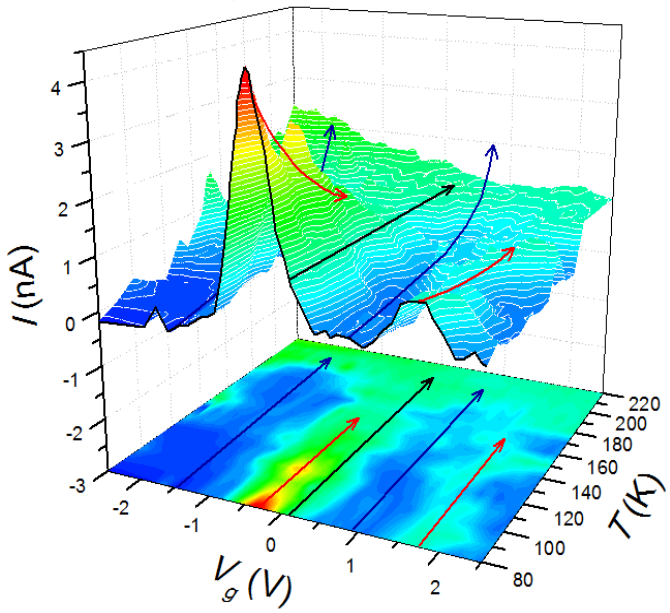

Figure 32: 3D plot of the evolution of the tunnel current through a S-$(CH_2)_4$-Fc-$(CH_2)_4$-S junction vs. gate voltage as the temperature is increased from 80 to 220K and bias voltage of 10mV. The evolution of the two charges points (-0.3V and 1.7V), whose magnitude decreases in increasing temperature, red arrows. Similarly, the increase in the Coulomb blockade areas can be seen by following the blue arrows.

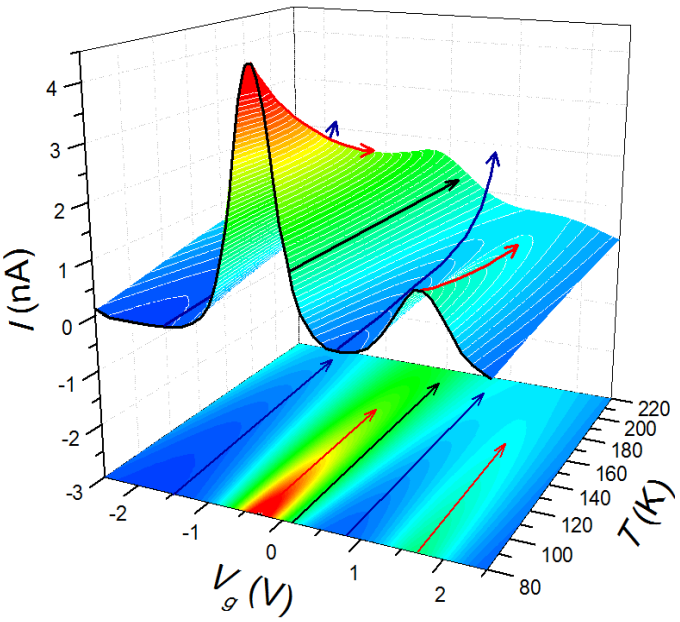

Figure 33: Corresponding response of Figure 32 as calculated from the single-level tunneling transport model in *Equation 3.7* using the parameters given in Table 1.

Similar behaviors were reproduced for all the different bias voltages recollected in our measurements. The results are shown from Figure 34 to Figure 36 for V_b = 30, 50 and 70 mV, respectively. As the bias voltage increases the transport excitations at the degeneracy points broaden (as expected from the different horizontal cuts of the Coulomb blockade diamond plot in Figure 31a), with the two consecutive charge states starting to intermix for the highest bias voltages (this end can be more clearly seen in Figure 31b for V_b = 50 and 70 mV).

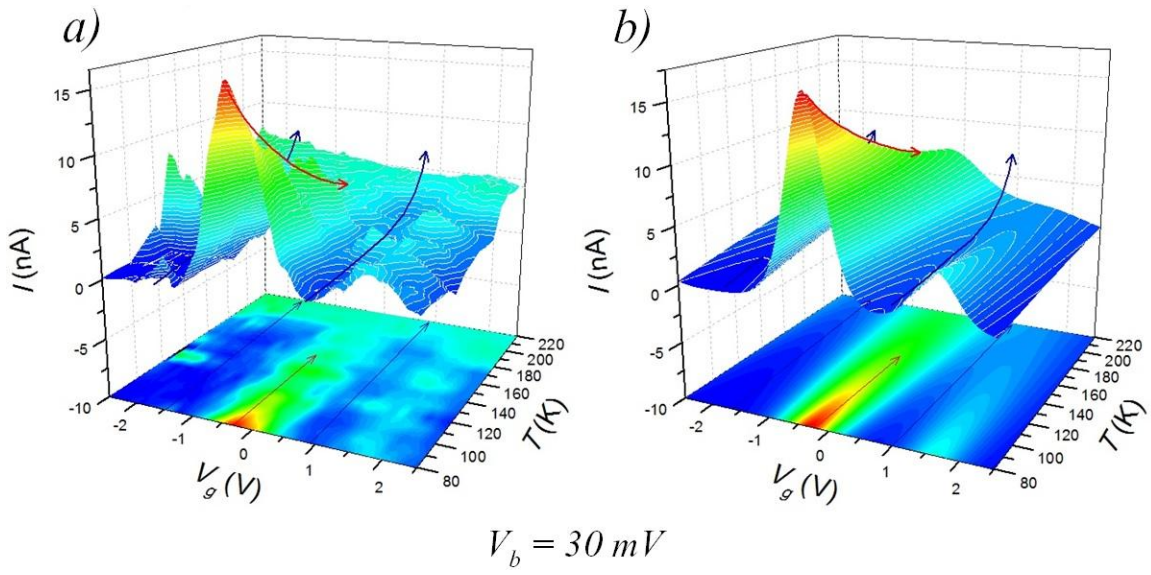

Figure 34: 3D plot of the evolution of the tunnel current through a S-$(CH_2)_4$-Fc-$(CH_2)_4$-S junction vs. gate voltage as the temperature is increased from 80 to 220K and with an applied bias voltage of 30mV.

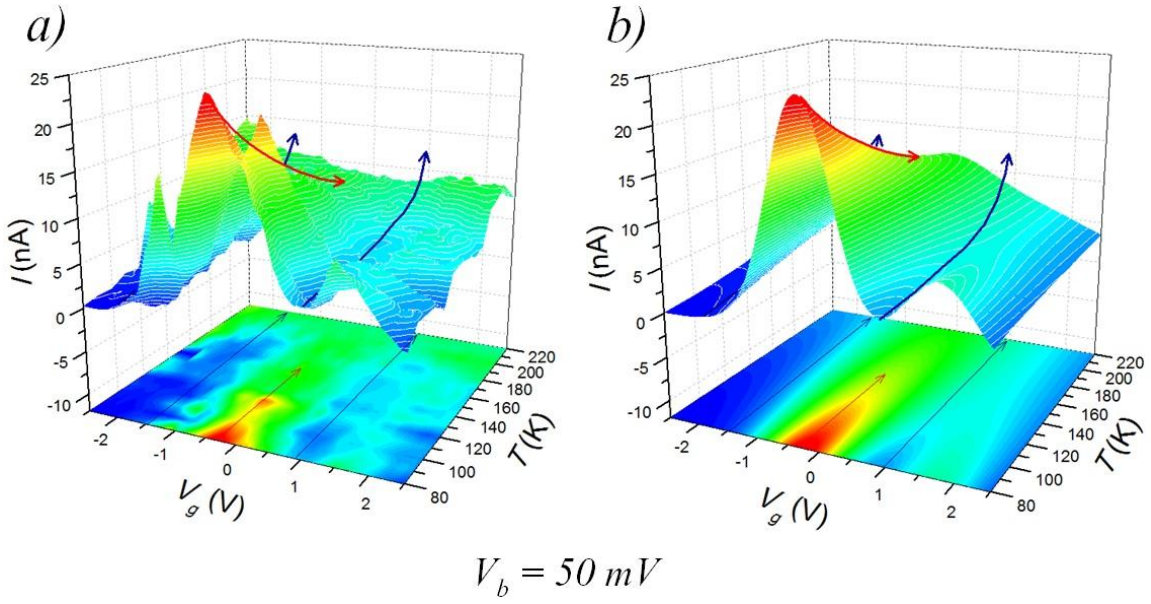

Figure 35: 3D plot of the evolution of the tunnel current through a S-$(CH_2)_4$-Fc-$(CH_2)_4$-S junction vs. gate voltage as the temperature is increased from 80 to 220K and with an applied bias voltage of 50mV

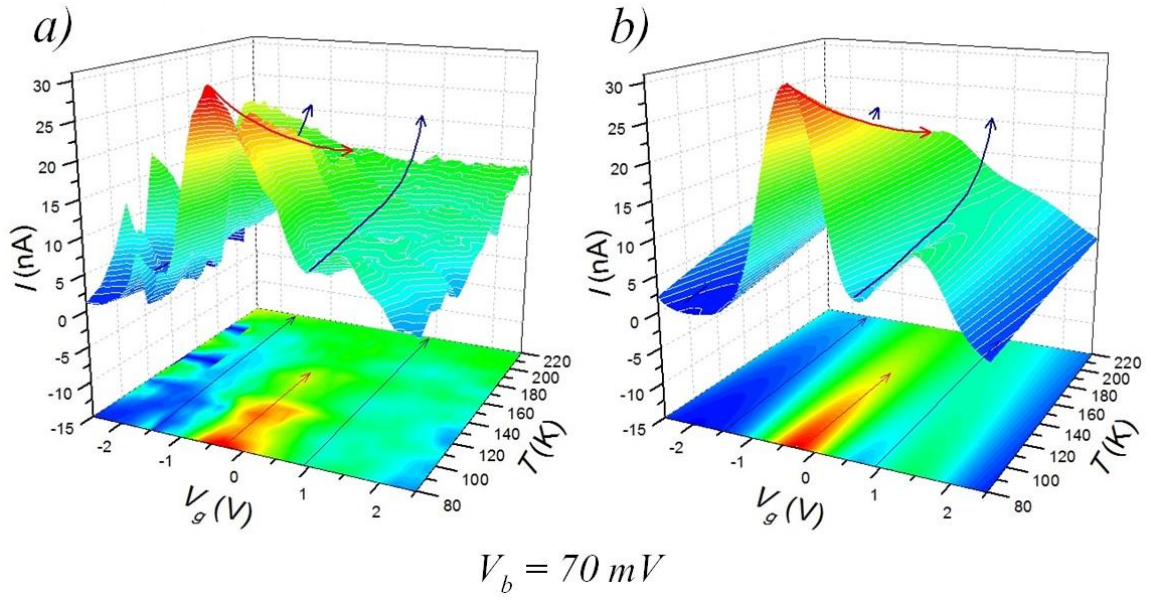

Figure 36: 3D plot of the evolution of the tunnel current through a S-$(CH_2)_4$-Fc-$(CH_2)_4$-S junction vs. gate voltage as the temperature is increased from 80 to 220K and with an applied bias voltage of 70mV.

The tunneling current magnitude exhibits an overall increase as the bias voltage is increased. Still, the temperature dependences in the different conduction regimes remain the same for all measured bias. This can be clearly observed in Figure 37, which displays the behavior of the tunneling current through the molecular junction as a function of temperature for two different bias voltages, 10 and 50 mV (Figures 37a and 37b, respectively) and for four different gate voltages.

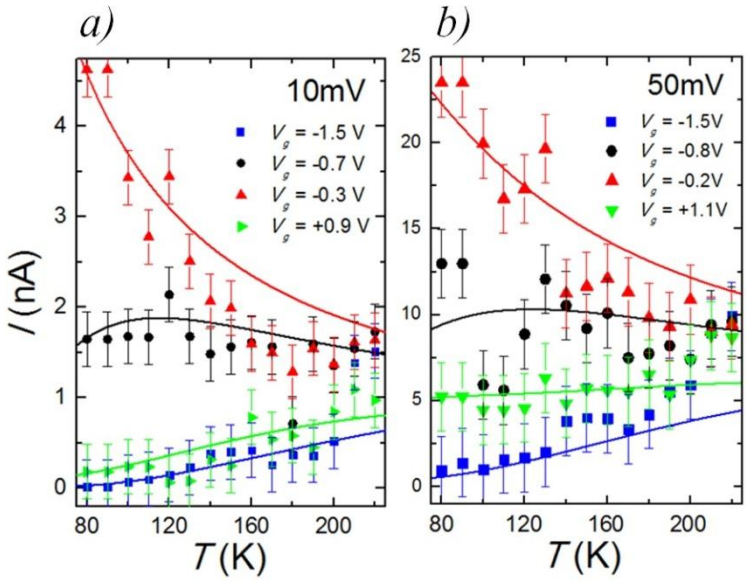

Figure 37: a) Evolution of the tunnel current with temperature at 10mV for four different gate voltages (Vg = -1.5, -0.7, -0.3 and +0.9V). b) Same for 50mV (Vg = -1.5, -0.8, -0.2 and +1.1V). The solid lines in both panels represent fittings to the single-level tunneling transport model in *Equation 3.7* with the parameters given in Table 1. Error bars represent the uncertainty in the determination of the value of the tunneling current due to the noise of the measurements.

Different gate voltages for each bias voltage are specifically selected, in Figure 37, to sample the different conduction regimes observed in the data. Specifically, V_g = -1.5 (blue squares) and +0.9 V (green triangles) in Figure 37a (V_g = -1.5 and +1.1 V in Figure 37b) represent the Coulomb blockage regimes, with the current increasing as a function of

temperature. V_g = -0.3 V (red triangles) in Figure 37a (V_g = -0.2 V in Figure 37b) represents the charge degeneracy point, with the current markedly decreasing as temperature is raised. Finally, V_g = -0.7 V (black circles) in Fig. 37a (V_g = -0.8 V in Figure 37b) represents the coordinates of bias and gate voltage for which the molecular conduction level matches in energy (resonance) of the Fermi energy of one of the electrodes, for which only a slight overall change in current is observed for the measured range of temperatures.

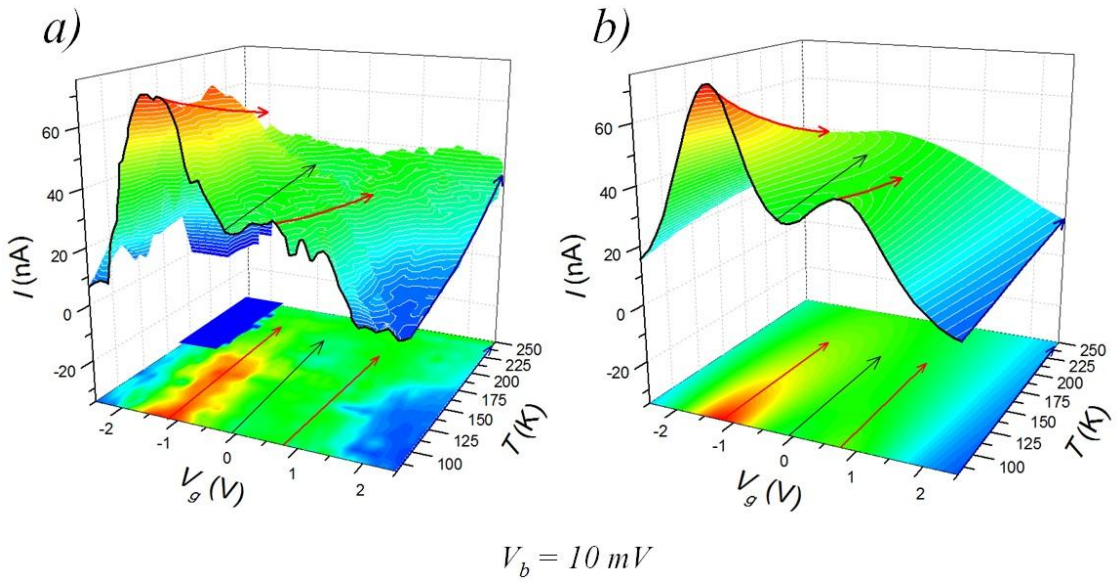

Figure 38: a) 3D plot of the evolution of the tunnel current through a second S-$(CH_2)_4$-Fc-$(CH_2)_4$-S junction vs. gate voltage as the temperature is increased from 80 to 250K and with an applied bias voltage of 10mV. The evolution of the two charge points (Vg = -1.25 V and 0.8V), whose magnitude decreases with increasing temperature are indicated with red arrows in both the 3D data and the corresponding 2D horizontal projection in the *Vg-T* plane. Similarly, the increase of the current in the Coulomb blockade area is indicated with the blue arrow. b) Corresponding response of the junction as calculated from the single-level tunneling transport model in *Equation 3.7* using the parameters given in Table 2.

Similar results were obtained in a second molecule. Figure 38 shows a 3D plot of I vs. V_g as a function of temperature for V_{sd} = 10 mV in the same ferrocene-based molecule measured for this study. The data were collected as the gate voltage was continuously swept from -2.5 to

+2.5 V at each temperature ranging from 80 to 250 K. Figure 38a shows the experimental data and Figure 38b shows the modelling results. Similar to the previous one, this one shows: *i*) the Coulomb blockade regime, with *I* increasing exponentially with temperature (follow blue arrow at V_g = 2.5V and its projection in the lower V_g-*T* panel in Figure 38a); *ii*) the degeneracy points, with *I* decreasing markedly with *T* (red arrows); and, *iii*) intermediate zones, with just a slight variation of *I* with *T* (black arrow) when the molecular level matches the electrostatic potential of one of the leads (resonances).

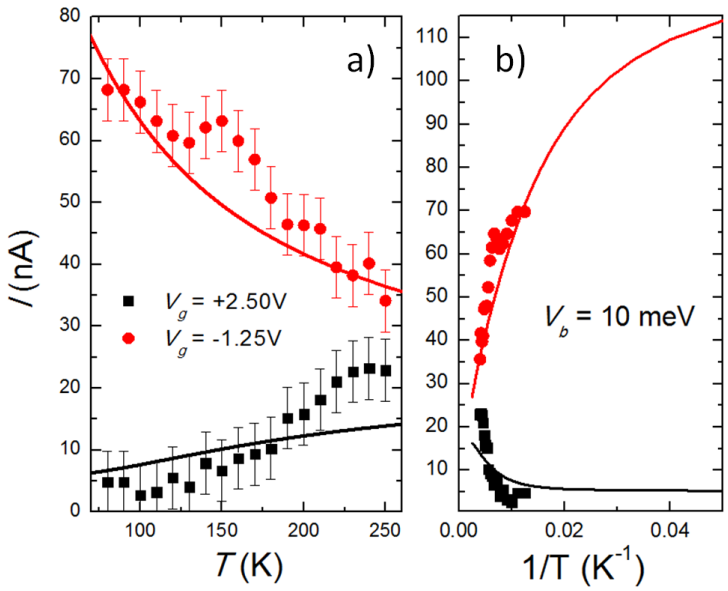

Figure 39: a) Experimental and calculated evolution of the tunnel current with temperature at 10mV for two different gate voltages, Vg = -1.25V (charge degeneracy point) and +2.5V (Coulomb blockade regime). b) The same results shown as a function of the inverse temperature in an extended range of temperature to visualize the transition between the temperature-independent and -dependent conduction regimes, which for this molecule occurs at ~100K. Error bars represent the uncertainty in the determination of the value of the tunneling current due to the noise of the measurements.

Figures 39a and 39b display the behavior of *I* as a function of *T* for two values of V_g specifically selected to sample the coulomb blockade regime, V_g = 2.5 V (black squares), and the charge degeneracy point, V_g = -1.25 V (red circles), for V_b = 10 mV. With the same overall

behaviors as those found in the previous molecule. Specifically, with *I* increasing with *T* in the Coulomb blockade regime and *I* decreasing with *T* at the charge degeneracy point. The transition between the temperature-dependent and temperature-independent behavior of the current in the Coulomb blockade regime can be clearly seen in Figure 39b (black squares) to occur at about 100 K for this molecule. The continuous lines in Figure 39 represent the fittings to the model (*Chapter 3*), in good overall agreement with the data, with the exception of the data at the highest temperatures. This is likely due to a molecular conformational change (e.g. a slight displacement of the molecule with respect to the SET leads) or a bond-fluctuation due to a change in the molecular attachment to the electrodes [55] occurring at ~175 K which shifted the charge degeneracy points ~1 V towards positive gate voltages, also affecting the overall conduction through the junction for higher temperatures. To correct this displacement, the data above ~175 K was correspondingly shifted to higher gate voltages, as can be observed in the horizontal projection of the data in Figure 38a, with no data in the $T > 175$ K – $Vg < -1.5$ V area (dark blue area).

4.4. Interpretation of the Temperature Dependencies

Table 1 shows the parameters used to fit all the experimental results on the first molecule, as shown in Figures 31b, 33,34b, 35b, 36b and 37. The agreement is good in explaining the temperature, bias and gate voltage dependences of the tunneling current through the molecular junction within the different conduction regimes, including the Coulomb blockade regimes and the charge degeneracy points, as well as in resonance areas. Note that three molecular levels were taken into account as contributing to the conduction within the experimental window of

electrical potentials. A first estimate of the energy distances between the respective levels is made from the position of the degeneracy points observed in Figure 31a, and then adjusted to fit the data in the subsequent measurements for varying temperatures and bias potentials, since a small conformational change in the molecule had affected the coupling to the gate for the latter (as mentioned above).

Table 1: The fitting parameters to model the experimental data. [a] The model is given by *Equation 3.7* (*Chapter 3*). [b] The values of the three molecular levels ε_1, ε_2 and ε_3, were experimentally determined from *I* vs. V_g-V_{sd} data.

V_{sd} (mV)	ε_1 [b] (mV)	γ_{1L} (mV)	γ_{1R} (mV)	ε_2 [b] (mV)	γ_{2L} (mV)	γ_{2R} (mV)	ε_3 [b] (mV)	$\gamma_{3L,R}$ (mV)
10	25	1	0.120	185	3	0.040	-225	0.20
30	25	4	0.155	180	7	0.042	-225	0.24
50	25	7	0.160	170	15	0.060	-225	0.27
70	25	10	0.170	165	20	0.075	-225	0.30

In essence, only three free-fitting parameters are used per molecular level to fit the results with *Equation 3.7*, *i.e.*, the level position ε_i and the respective tunneling rates ($\gamma_{L,R}$) associated to the flow of electrons from the electrodes into/out of the molecule. The distance between the main two levels (ε_1 and ε_2) whose degeneracy points are observed within the gate voltage window in Figure 31b varies slightly with the applied bias, decreasing from 160 *meV*, for V_b = 10 mV, down to 140 *meV*, for V_b = 70 mV. The shift of the molecular levels in response to applied bias has been predicted and observed in other molecular tunnel junctions [9], and is associated with the static Stark effect [56]. This shift was taken into consideration in the fitting procedure. The third level, ε_3, responsible for the degeneracy point lying off the gate voltage window (V_g ~3.5 V) is

included to account for the increase in conduction for V_g < -2 V, but since it is not clearly visible for all bias/gate voltages, its position with respect to ε_1 has been left unaltered by the applied bias.

The tunneling rates used for each level are also found to depend on the applied bias, increasing as the bias voltage increases, thus leading the overall increase of width and current with increasing bias. Highly asymmetric tunneling rates for the main two levels had to be employed to fit the results. The reason lies in the fact that these rates present two main effects on the conduction through the junction. On the one hand, the sum of the right and left tunneling rates determines the zero-temperature width of the level at each bias, and therefore the highest rate is fixed by the experimental widths of the transport excitations. On the other hand, the lowest rate limits the current through the junction, and therefore is fixed by the experimentally observed value (For the same reasons mentioned above, just a single value of $\gamma_{3L} = \gamma_{3R}$ for each bias is used in level ε_3).

Table 2: Parameters employed in fitting the experimental data in Figures 38 and 39 to the single-level model (*Equation 3.7*)[a]. [a] Two molecular levels with energies ε_1 and ε_2 with respect to the Fermi energy of the electrodes at zero bias were determined from the experimental data.

V_b (mV)	ε_1 (mV)	γ_{1L} (mV)	γ_{1R} (mV)	ε_2 (mV)	γ_{2L} (mV)	γ_{2R} (mV)
10	62.5	30	3	165	45	1.9

The results for the second molecule (Figure 38b and Figure 39) were fitted to the model given by *Equation 3.7* using the parameters listed in Table 2. Figure 38b shows a 3D plot of the calculated current through the junction. Two molecular levels were employed to account for the

two degeneracy points observed within the window of electrical potentials. Again, only two free-fitting parameters were used per molecular level to fit the results with *Equation 3.7, i.e.,* the respective tunneling rates ($\gamma_{L,R}$) associated to the flow of electrons from the leads into/out of the molecule. Here, the values of $\gamma_{L,R}$ are ~10 times larger than those used to fit the experimental data discussed in the previous molecule; these large values of $\gamma_{L,R}$ are in agreement with the larger current magnitude (~10 times larger) and excitations widths observed in the second molecule, and can be associated to a stronger connection of the molecule with the transistor leads.

The model explained in *Chapter 3* accounts for the temperature dependence within the different conduction regimes in our molecular junctions, and remarks the fact that it naturally arises from the thermal broadening of the Fermi electronic occupation distribution in the leads. The theoretical results closely follow the experimental observations within the whole range of temperatures and different bias of this study (the same degree of agreement is found with the other measured bias). The model accounts for the temperature dependence of the current in different conduction regimes, a decrease, with temperature, at the charge degeneracy point, an increase in the Coulomb blockade regime and constant at resonances.

The junctions presented clear evidences of the transition between the thermally assisted and the coherent tunneling regimes in the Coulomb blockade regime (*e.g.*, V_g = -1.5 V in Figure 37a), with the data/calculation bending as the temperature is close to 80 K. Figure 40 extends the calculations presented into lower temperatures to give a better idea of the crossover between the temperature-dependent and -independent conduction regimes. This transition

depends strongly on the applied gate and bias voltages. Figure 40 shows the case for V_b = 10 mV, where the crossover temperature in the Coulomb blockade regime (V_g = -1.5 V) lies at ~65 K, which is slightly lower than the lowest temperature used in the experiments. Figure 41 shows a log-plot of the calculated current for V_b = 10 mV and the behavior of the crossover temperature with the applied gate voltage; this crossover linearly increases with bias.

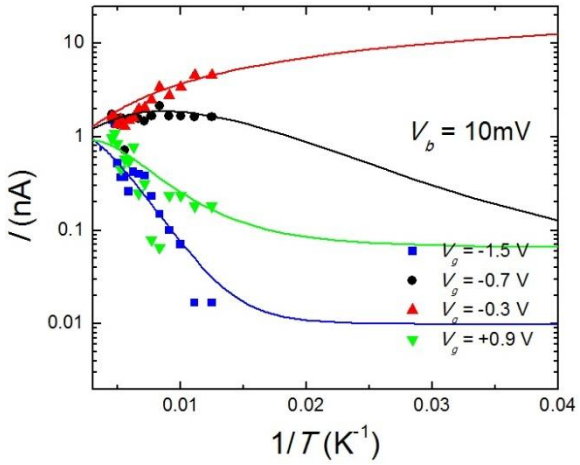

Figure 40: Experimental (symbols) and calculated (lines) current versus the inverse of temperature for four different gate voltages, V_g = -1.5, -0.7, -0.3 and +0.9V, at V_b = 10mV, from 25 to 300K.

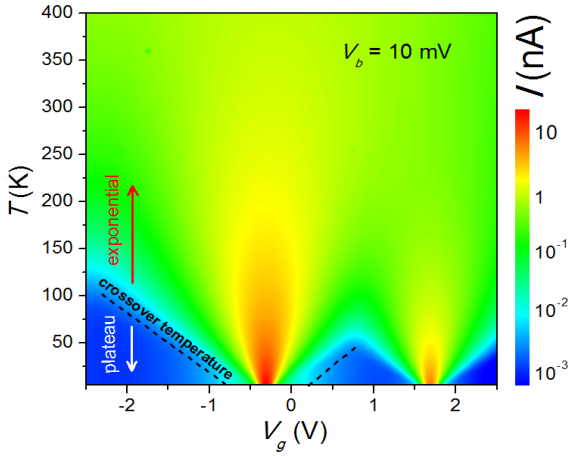

Figure 41: Contour color-code plot of the temperature behavior of the current (in log-scale) with respect to gate voltage for V_b = 10mV.

4.5. Reversibility of the Temperature Behavior of the Tunnel Current through the SET

Figure 42 shows measurements of the tunneling current through the molecular transistor obtained at different times between which the temperature of the sample had been raised to ~200 K. Figure 42a contains the same data shown in Figure 31a, corresponding to the preliminary characterization of the Coulomb blockade response of the molecular SET at ~80 K, with the two charge degeneracy points at V_g = 0.25 and 2.5 V (V_{sd} = 0), and an energy separation between the corresponding charge states of $\Delta\varepsilon$ ~110 *meV*. After that preliminary characterization, the temperature was raised to ~200 K, while taking some sample I_{sd} -V_g curves at V_b = 10 mV at a few intermediate temperatures as a quick check of the temperature behavior of the device and to test its stability (procedure repeated with all detected molecules).

After that, the temperature was decreased back to ~80 K. Figure 42b shows the I_{sd} -V_g curve at V_b = 10 mV obtained after that (same data in Figure 31b). Only a small change in the position of the degeneracy points (now at V_g = -0.3 and 1.7 V), and a change in energy difference between the two charge states (now $\Delta\varepsilon$ ~140 *meV*) was observed, while the overall behavior of the molecular SET was unaltered. As mentioned in *Section 4.1*, this may be associated to small conformational changes of the molecule within the transistor leads or bond-fluctuations due to alterations in the attachment of the molecule to the electrodes [55]. Subsequently, the temperature behavior of the device was studied while slowly increasing the temperature up to 220 K, from which the central results of this work were obtained. At the conclusion of the study, the temperature was decreased again back to ~80 K and a new Coulomb blockade contour plot was measured (Figure 42c), which shows that the molecule behaved similarly after the thermal

cycling (with V_g = -0.4 and 2.2 V, and Δε ~140 *meV*), demonstrating the reversibility of its temperature behavior.

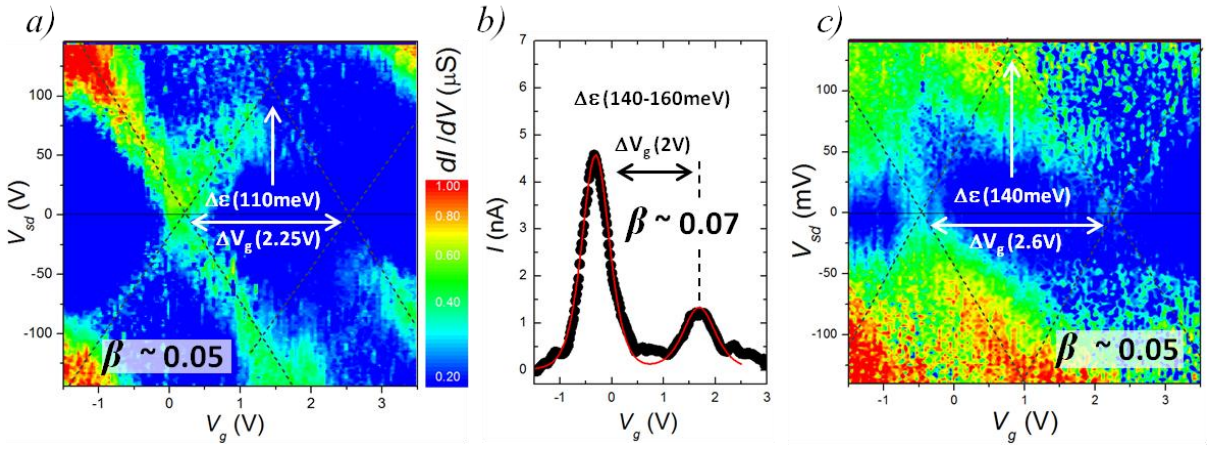

Figure 42: a) Differential conductance of a junction with S-(CH2)4-Fc-(CH2)4-S at T = 80K (same data as in Figure 31a for (a) and (b)). The color code represents the conductance (*dI/dV*) through the SET as a function of V_{sd} and V_g. b) Current vs. gate voltage for V_{sd} = 10mV at T = 80K obtained after the first thermal cycling (same data than in Figure 31b). c) Differential conductance of the same junction at T = 80K after the temperature dependency study had been completed (using the same color code scale than in (a) for the conductance).

CHAPTER 5:
TEMPERATURE-DEPENDENT TUNNELING ACROSS SELF-ASSEMBLED MONOLAYERS

This chapter focuses on some recent experiments on SAM-based two terminal molecular junctions, where a record-high rectification ratio of three orders of magnitude was achieved [24]. The experimental data presented in this chapter can be well explained by the theory exposed in *Chapter 3*.

5.1. A Two-level SAM-based Molecular Junction

Let us first review the molecule chosen for these experiments. Figure 43a shows a sketch of the molecular junction formed by a SAM of $S(CH_2)_{11}Fc_2$ molecules (with Fc_2 representing a biferrocenylene (Fc=Fc) head group) sandwiched in between GaO_x^{cond}/EGaIn (top) and Ag (bottom) electrodes (see Refs. [24,34] for synthesis and experimental details). In these junctions, the Fc_2 lies at the end of a long insulating alkyl chain, providing a non-covalent (van der Waals) coupling to the top electrode. This results in a highly asymmetric drop of electric potential at both sides of the Fc_2 (where the frontier orbitals are located) enabling large rectification ratios. In particular, the Fc_2 presents two distinct conduction levels (HOMO and HOMO-1, see Fig. 43b) separated by an energy of 0.6 *eV*, as measured by cyclovoltammetry (CV) in solution and ultra-violet photoemission spectroscopy (UPS) in vacuum, which is much smaller than the HOMO-LUMO gap (which is approx. 2.0-2.5 *eV*).

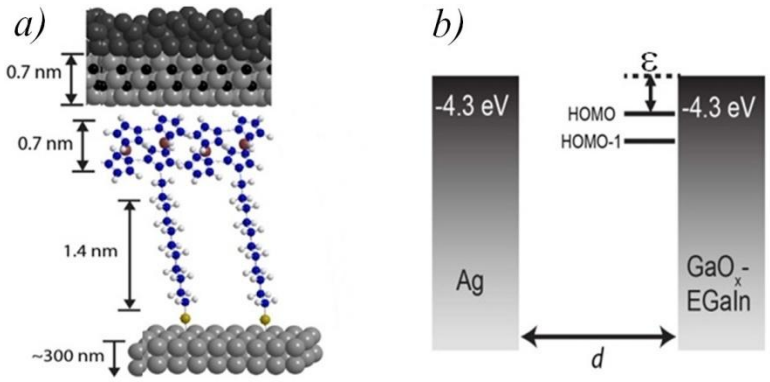

Figure 43: ***a) S-C_n-Fc_2-C_{13-n}*** **(Fc:ferrocene) molecules. The double-ferrocene unit placed at the upper side of the molecule with the iron atoms in red. Then thirteen saturated carbon groups $(CH_2)_{13}$ in the in the lower side of the ferrocene finishing with the thiol terminations (S) in yellow. b)** ***GaO_x^{cond}/EGaIn*** **and** ***Ag*** **electrodes with two distinct conduction levels of HOMO and HOMO-1, resulting from the two active Fc units.**

Room-temperature rectification ratio (defined as $R = |I(-V)|/|I(V)|$) is shown in Figure 44 as a function of the bias voltage applied to the junction (these measurements were done by our collaborators at the National University of Singapore). Apart from the high rectification ratio of 1.1×10^3 reached at $V = 0.875$ V, the *R*(V) plot shows two clear kinks at around 0.35 and 0.75 V which were ascribed to the HOMO and HOMO-1 levels associated to the double-ferrocene unit (see Figure 43) subsequently entering the conduction window defined by the difference in electrochemical potential of the top and bottom electrodes [24].

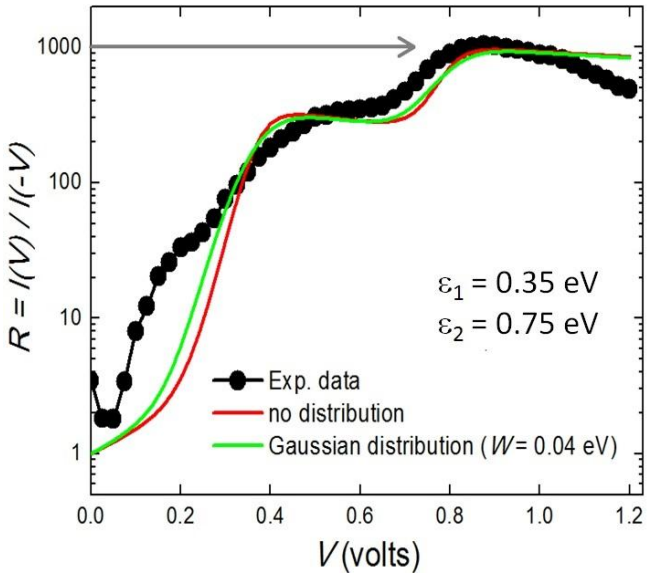

Figure 44: Room-temperature electrical current rectification as a function of bias voltage in a SAM-based junction of $S(CH_2)_{11}Fc_2$ molecules. Two distinct jumps in the rectification at 0.35 and 0.75V can be understood in terms of the HOMO and HOMO-1 levels entering the conduction bias window (as depicted in the sketch on the right), after which a record-high rectification ratio of 10^3 is achieved [24]. The solid lines are fits to a double-level transport model given by *Equations 3.5 and 3.7*, with (green) and without (red) the energy distribution of ε_1 and ε_2 given by *Equation 5.1*.

These results can be easily explained by incorporating a second level into the single-level transport model to account for the two Fc_2 levels, *i.e.*, the HOMO and the HOMO-1. The results of the calculation using *Equation 3.7* are shown in Figure 44 (continuous red line) for the following characteristic parameters: $\varepsilon_1 = 0.35\,eV$, $\varepsilon_2 = 0.75\,eV$, $\eta = 0.95$, and $\gamma_{1,L} = 3\,meV$, $\gamma_{1,R} = 1\,meV$, $\gamma_{2,L} = 5\,meV$, $\gamma_{2,R} = 2\,meV$. Note: the same results are obtained by *Equation 3.5* at room-temperature. The agreement is significant given the approximations in the model and the inherent degree of dispersion in the SAM-based molecular junctions.

The theory recovers the voltage position of the two kinks, supporting their association with the HOMO and HOMO-1 levels of the Fc_2 group, as well as the overall value of the rectification for most of the bias voltage range, including the maximum rectification of three

orders of magnitude. The separation between the levels in the *R-V* plot (0.4 *eV*, Figure 44) is smaller than that measured by CV and UPS (0.6 *eV*), which can be ascribed to an energy-renormalization of the molecular levels as a result of charge-image effects by the electrodes [24]. This effect should also decrease the HOMO-LUMO gap (estimated to be > 2 *eV*), allowing it to play some role in the conduction at large bias voltages (reverse polarity), which is likely responsible for the decrease of the rectification ratio above 1 V (Figure 44).

Given the fact that molecules are not all identically placed with respect to the electrodes and that their position may actually change during the course of a complete measurement, a Gaussian distributions for the energies of the HOMO and HOMO-1 levels to account for the degree of dispersion in the system can be used. To do so, *Equation 3.7* is modified as follows (note once again that *Equation 3.5* can be treated in the same way to give the same results at high temperature):

$$I = \frac{q}{h}\iint_{-\infty}^{\infty} dE dE'\, D_{\varepsilon}(E)\frac{\gamma_L\gamma_R}{\gamma_L+\gamma_R}[f_L(E) - f_R(E)]g_{\varepsilon}(E'), \tag{5.1}$$

where,

$$g_{\varepsilon}(E) = Exp\left[\frac{(E-\varepsilon)^2}{2W^2}\right] \tag{5.2}$$

The best results are obtained for a width of the Gaussian distribution $W = 0.04\ eV$ for each level (green line in Figure 44). This small dispersion in the position of the energy of the molecular levels (<10%), *i.e.*, injection gap, is indicative of the high degree of order in these SAM-based molecular junctions.

5.1.1. Maximum Rectification Ratio for a Single-level Junction

The rectification ratio of three orders of magnitude observed in Figure 44 for this molecular junction (with typical level widths $\gamma \sim$1-10 *meV*) is at the theoretical maximum limit expected from a single-level transport mechanism for characteristic positions of the frontier orbital with respect to the Fermi energy (ε ~0.5-1 *eV*) and operating voltages ($V \sim 1$ V). This is easy to see by looking in Figure 45 at the current and rectification ratios calculated from *Equation 3.7* for a molecular junction, where the parameters have been chosen to be representative of these kinds of junctions (*i.e.*, derived from experimental data). In particular, the calculations have been obtained for a single-level positioned at $\varepsilon = 0.5$ *eV*, and with a maximised asymmetric voltage divider parameter $\eta = 0$, to maximize the rectification ratio. Obviously, the rectification will be maximum for a bias voltage larger than -0.5 V, which is the forward voltage needed to bring the molecular level into resonance when $\eta = 0$ (as obtained from the definition of E_{m} and illustrated in Figure 27.

Figure 45a shows the behavior of the room-temperature electrical current with γ_i (with $\gamma_L = \gamma_R$) for both polarities of the bias voltage ($V = \pm 1$ V). As expected, the difference between the forward and reverse currents increases as the tunneling rates (and consequently the level width) decrease. Both currents reach the same saturation value for sufficiently high tunneling rates (*i.e.*, $\gamma_i \gtrsim 1$ *eV*), when the level width is larger than the separation between electrochemical potentials in the leads and the conductance becomes constant, as discussed in *Section 3.2.2.* and *Section 3.2.4*. The corresponding *R* for these voltages is shown in Figure 45b for different temperatures, to emphasise that it does not vary below room-temperature.

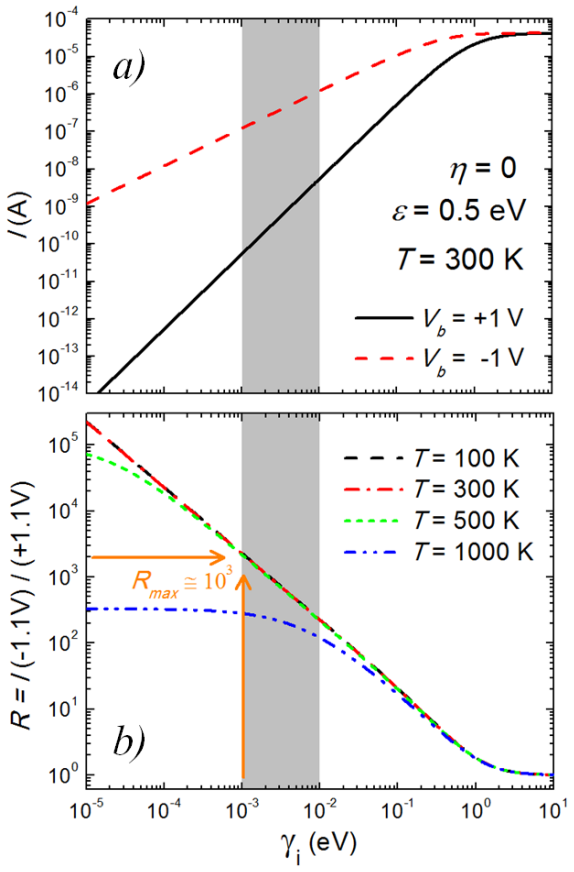

Figure 45: a) Electrical current and b) rectification ratio as a function of γ_i (with $\gamma_L = \gamma_R$) calculated solving *Equation 3.7* for a single-level molecular junction with the following parameters: $\varepsilon = 0.5eV$ and $\eta = 0$. For the typical smallest values of $\gamma_i = 1meV$, the rectification originated from a single level (*e.g.*, the HOMO orbital) in a molecular junction is theoretically limited to about three orders of magnitude.

In the range $10^{-5} < \gamma_i \lesssim 1\ eV$ the electrical rectification decreases exponentially at room-temperature and below, saturating at $R = 1$ (no rectification) for $\gamma_i \gtrsim 1\ eV$, corresponding to the behavior of the current in Figure 45a. From these results one can conclude that in molecular junctions of this kind, where the γ_i takes values typically above 1 *meV*, the rectification ratio will be limited to three orders of magnitude when a single electrostatic molecular level contributes to the conductance through the junction, which is the value found in the reported experiments [24] and marked by the arrows in in Figure 45b.

This result is found for voltage conditions that maximize the rectification efficiency (*i.e.*, $\eta = 0$) but with an experimentally relevant energy location of the frontier orbital ($\varepsilon = 0.5\ eV$) and values of γ_i. Larger ε values and, consequently, larger voltages will increase this limit, but not substantially. Evidently, if more than one molecular level is involved in charge transport the rectification can be improved by a factor proportional to the total number of levels involved. However, since it is unlikely to find molecular junctions with more than a few levels in the vicinity of the electrochemical potential of the leads, it is unwise to expect substantially higher electrical rectification ratios originating from the molecular level structure. Imaginative ways should be explored in order to overcome this limit in practice, perhaps by engineering junctions that mix high single-level rectification properties with conformational changes in the molecule that can build up to increase the overall rectification of the junction.

5.2. Determination of the Electrostatic Potential Profile in a Molecular Junction

A recent collaboration between our group and the group of Dr. Nijhuis at NUS resulted in a report of a study of electrical rectification in EGaIn SAM-based junctions where the Fc unit was placed at 14 different positions within the SAM. The molecules have the form of S-C_n-Fc-C_{13-n}, where C_n represents the number of aliphatic carbons (CH_2 or a terminal CH_3), with n = 0 to 13 (*Section 1.5.*). Controlling the position of the Fc unit (where the molecular HOMO level is localized) along the alkyl chain for different values of n (see sketches in Figure 46) allows us to quantify the rectification response for different energetic symmetries in the junction (values of η), since the electric potential at both sides of the conduction unit (*i.e.*, Fc) will strongly depend on its position along the chain. This enables sampling of the electrostatic

potential profile along the junction gap, founding to be highly non-linear in this particular molecular junction [33].

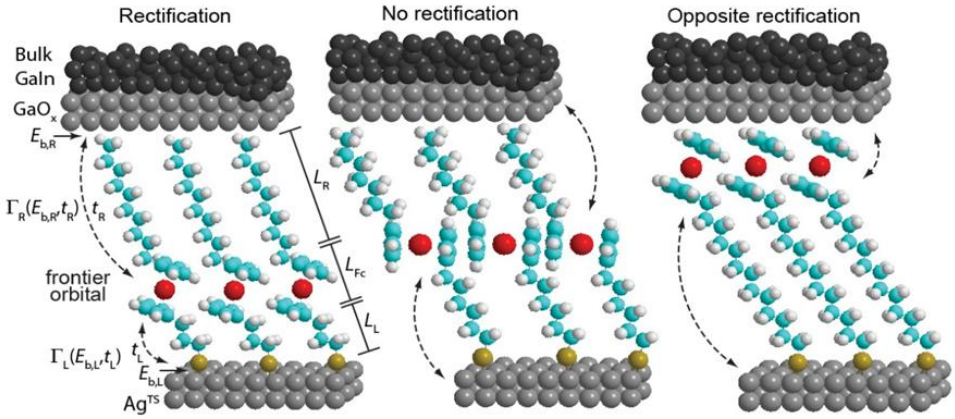

Figure 46: Sketch representation of the EGaIn SAM-based junctions formed by S-C_n-Fc-C_{13-n} molecules for three different positions of the Fc unit within the alkyl chain.

Figure 47 shows R as a function of n measured at room-temperature and calculated by comparing the electrical currents at $V = \pm 1$ V in S-C_n-Fc-C_{13-n}. As can be clearly observed, the rectification behavior is highly non-linear, with several distinct areas, and with the maximum rectification values achieved when the Fc unit is placed close to one of the electrodes (*i.e.*, n = 3 and n > 10), as expected from the asymmetry in the potential drops at both sides of the Fc. For n < 3 the strong hybridization between the Fc and the bottom electrode (chemisorbed contact) leads to large level broadenings and leakage currents, this turns results in lower rectification ratios. A similar effect (*i.e.*, R saturates), although weaker, arises for n > 10 due to proximity to the top electrode, where the coupling between the molecule and the lead is non-covalent (van der Waals interactions). The intermediate range of Fc positions ($4 < n < 11$) is the most interesting in the context of the analysis of the electrostatic potential profile, since coupling between the Fc

unit and the electrodes is non-covalent, and the molecular level responsible for conduction is well defined, with a width that can be considered constant.

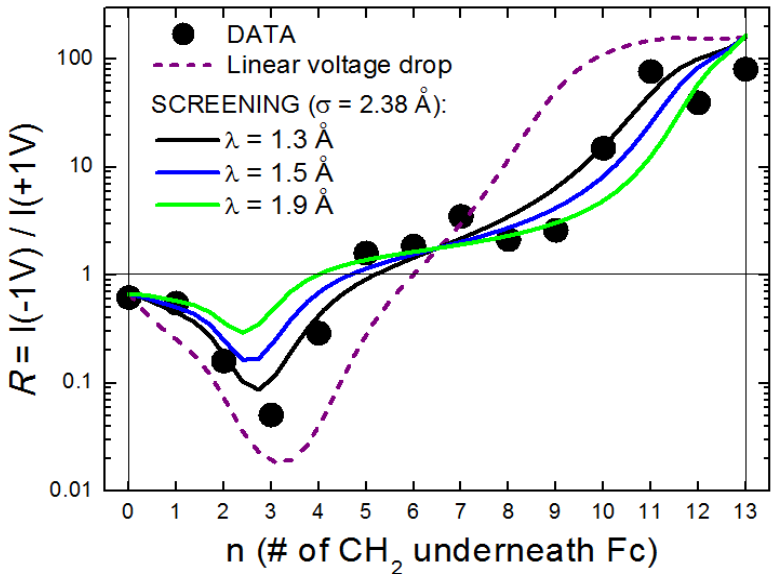

Figure 47: Measured rectification ratio of the junctions [33] as a function of the position n of the Fc unit within the chain (solid circles). The lines represent fittings to the data using the single-level transport model in *Equation 3.7* using different shapes for the electrostatic potential profile in the junction, including linear (dashed purple line) and non-linear as derived from a model that assumes the molecule a cylinder of radius σ and takes into account screening of the electric field by the molecule (with screening length λ).

The results in Figure 47 have been fitted to the single-level model given in *Equation 3.7*. *Equation 3.5* will give the same exact results for this temperature and electric potential conditions. Before getting into the details of the calculations, the fitting results show that the distinct behaviour of *R* for intermediate n values, and particularly its small slope for n = 5 - 9 (Figure 47), can only be explained by taking into account screening effects, *i.e.*, a non-linear electrostatic potential profile. The single-level transport models together with a functional treatment to account for electric field screening proposed by Nitzan and collaborators [57] allow

determination of the electrostatic potential profile and extraction of a quantitative estimate of the screening length in a molecular junction, which has not been possible to date.

5.3. The Analytical Model of the Electrostatic Potential Profile in a Molecular Junction

Analytical models have been employed by means of *Equation 3.7* to fit the rectification data in Figure 47. First, for the distance dependence of the energy of the HOMO level, ε, the following "synthetic" function has been employed: $\varepsilon(n) = \varepsilon(n{\sim}13) - Ae^{-Bn}$, with $\varepsilon(n{\sim}13) = 0.75\ eV$ (see solid black line in Figure 48b). The rationale behind this selection is based on the n-dependence of ε^{exp} obtained from UPS data (see Figure 48a), which departs from its linear behavior for distances below n ~ 5. The solid black squares in Figure 48b, closely following the function used in the calculations (solid black line), represent the result of subtracting a linear function (dashed line in Figure 48a) from the experimentally obtained value of ε^{exp}.

The linear behavior is associated with the screening by the metallic electrodes and depends on the Fc-distance (thus the linearity). Therefore, for n > 5 the energy offset ε(n) is expected to be constant (*i.e.*, independent of n). Departures from linearity (as observed for n < 5) are ascribed to a real change in the distance between the molecular level and the Fermi energy of the electrode, which in this case decreases. Figure 48b shows the experimental data of Figure 48a after subtraction of the linear slope and shifting by 0.75 *eV* (black squares), together with the function used to fit the data (black line).

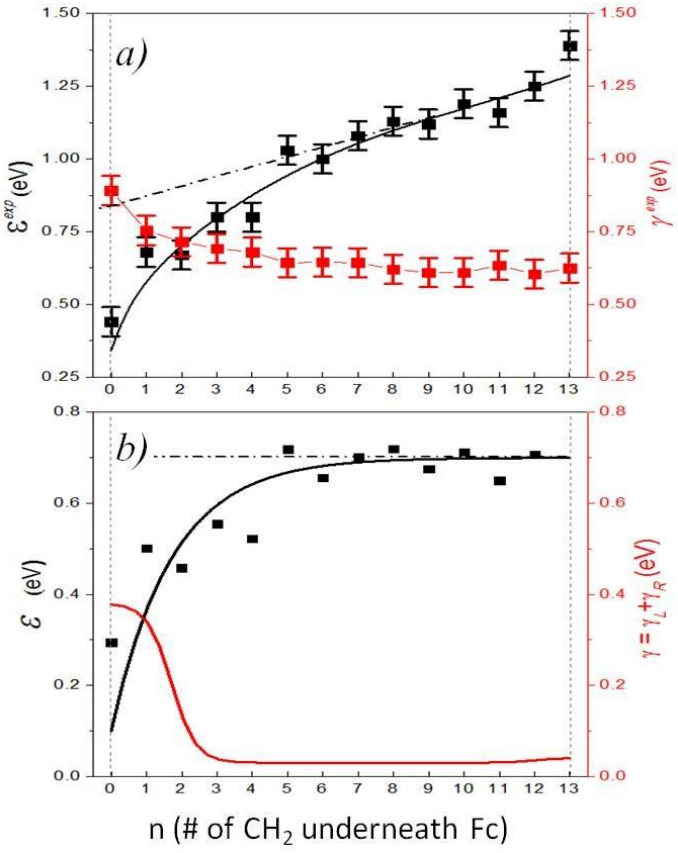

Figure 48: a) Experimental value of ε^{exp} (left axis) and γ^{exp} of the S-C_n-Fc-C_{13-n} SAMs on Ag^{TS} as a function of n. The lines are guides to the eye, with the dashed line representing the linear background expected from screening by the metallic electrodes, which is proportional to the Fc-electrode distance. b) Functions employed to represent ε and γ for different positions of the Fc within the alkyl chain (black and red lines, respectively). The solid squares are the data in (a) after subtraction of the observed linear slope in the UPS data caused by electron-hole screening effects. The resulting data have been shifted up in energy by 0.75eV to make it coincide with the function used to fit the experiments (black line).

Distance-dependence functions have been chosen to represent the coupling energies γ_L(n) and γ_R (n), and consequently the HOMO level width γ(n) = γ_L(n) + γ_R(n), and ε(n) in order to account for the effect of the coupling to the respective electrodes. Figure 48b shows the values of γ(n) and ε(n) used in the calculations (solid curves). The broadening of the HOMO level in proximity with the electrode is expected to increase exponentially with decreasing Fc-electrode distance. Fermi's golden rule gives $\gamma_{L,R} = t_{L,R}^2/D_{L,R}$, where $t_{L,R}$ is the effective coupling matrix

and $D_{L,R}$ the electron bandwidth in the electrodes [58]. In general, $\gamma_{L,R} \propto e^{-ekL_{L,R}}$, where *k* is the tunneling attenuation coefficient, proportional to $\sqrt{E_{barrier}-E_F}$, which for alkyl chains on Au and Ag is on the order of a few *eV*.

As observed in Figure 48b, the functions chosen to mimic this effect for γ_L and γ_R are not purely exponential with n close to the electrodes but saturate for distances below two CH_2 units (n < 2 and n > 12) from the respective electrodes. This has been done in order to account for the variability in Fc-electrode distances in the SAM. Basically, there are little differences observed in the spectroscopic results between SAMs with n = 0 and 1 (and 2 to some extent) [33]. As shown in Figure 48b (red curve), the used dependence for the level width reaches maximum values of γ_L(n<2) = 360 *meV* (due to strong hybridization with the Ag electrode) and γ_R(n>11) = 40 *meV*, and a base value of $\gamma = 30$ *meV* (with $\gamma_L = \gamma_R = 15$ *meV*) for intermediate distances, as obtained from the fitting of the rectification curves (see below). Note that taking the full width at half maximum from UPS data to estimate the molecular level broadening results in an overestimation of γ due to limitations of the technique (and therefore we only can derive the relative values of γ [33].

According to *Equation 3.5* and *Equation 3.7*, the only other ingredient for calculating the electrical current through the molecular junctions is the functional describing the electrostatic potential profile in the junction, which is represented by $\eta(n)$. Two different models has been employed to obtain this parameter: i) A simple linear electrostatic potential profile; and, ii) a correction to account for electrical screening in the alkyl chain.

5.3.1. Linear Electrostatic Potential Profile

Assuming a linear dependence of the voltage drop as a function of the distance between the Fc and the respective electrodes (*i.e.*, $V_L \propto L_R$), one can rewrite $\eta = V_R/(V_L + V_R)$ as $\eta \approx L_R/(L_L + L_R)$. To account for the voltage drop at the Fc, the expression above can be rewritten assuming a correction L_{Fc} for the respective lengths [49], and the expression for the dimensionless division parameter is:

$$\eta(L_R) = \frac{L_R+L_{Fc}}{L_L+L_R+2L_{Fc}} + \eta_{shift}\,, \qquad (5.3)$$

where η_{shift} is an effective shift introduced to account for the asymmetry generated by different couplings of the molecule with the two different electrodes and to explain the small rectification ratios ($R < 2$) observed in equivalent alkyl chains without the Fc unit, or when the Fc is placed in the middle of the chain. The corresponding η in the case of our molecule is given in Figure 49 (dashed purple line). Note that 8.7% [$= L_{Fc}/(L_A + 2\,L_{Fc})$] of the voltage drops in the Fc and remains unavailable for use in the rectification process. The strength of this correction is proportional to the size of the active unit employed to sample the electrostatic potential profile, which in this case is substantially larger than the adjacent CH_2 units. An ideal unit to sample the electrostatic profile would be one of negligible size (which is not possible, of course). That would also guarantee that the sampled molecule would remain undistorted when moving the active unit within the chain.

The resulting rectification curve obtained using the linear model defined by *Equation 5.3* (dashed purple line in Figure 47) does not give an overall good fit to the data but can explain some features. It quantitatively explains the high rectification ratios for $2 < n < 5$ and $n > 9$ and accounts for the abrupt decrease of rectification for $n < 3$ (resulting from a substantial level

broadening due to hybridisation with the left Ag electrode). However, it fails to explain the non-monotonic behaviour of the rectification for intermediate n values, and, particularly, the small slope for 4 < n < 10 (almost constant). This flat region is one of the main results arising from the sampling procedure to extract the exact shape of the electrostatic potential profile in these junctions, enabled by the capacitive nature of the Fc-electrodes coupling in this range of n values. This discrepancy presents a clear indication that the voltage does not drop linearly within the molecule, as it would be the case in vacuum.

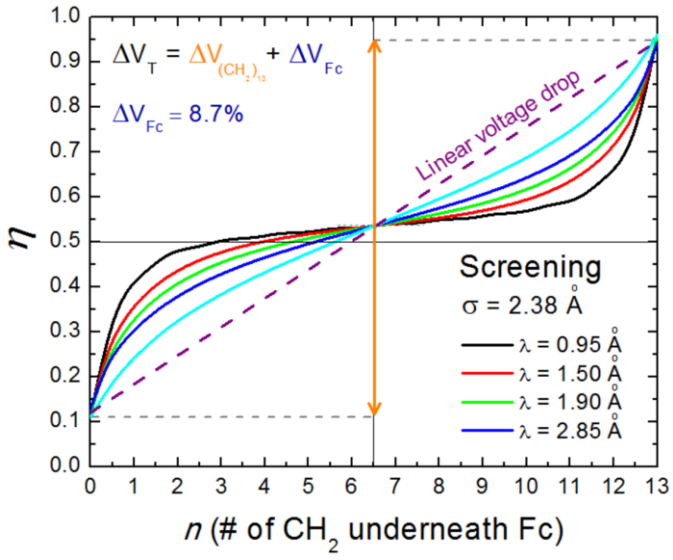

Figure 49: Electrostatic potential profiles in the molecular junctions as represented by the dimensionless voltage division parameter η. The curves represent the voltage drop within the alkyl chain on both sides of the Fc unit (totalling 91.3%), which is not the total voltage drop in the junction, since a substantial fraction decays in the Fc (8.7%). Also, the curves have been shifted from R = 0.5 in order to account for the different binding energies of the molecule with the left and right electrodes, which leads to a small rectification even in the absence of the Fc unit (or when it is placed at the center of the junction). The linear profile that would be expected in vacuum (red curve) is modified when accounting for electrical screening by the alkyl chain, idealized as a cylinder of diameter σ and electrical screening length λ.

5.3.2. Correction for the Screening of the Electric Field by the Molecule

The electrochemical potential in electrode-conductor-electrode junctions drops mainly at the contacts, but this is not applicable to the electrostatic potential, which may show profiles extending well into the low-dimensional conductor (e.g. molecule) for sufficiently long electric screening lengths, λ, which is the case in semiconductors and molecular insulators (Liang *et al*. [58]). It is therefore necessary to account for electrical screening effects when trying to explain our observations. For this, the theoretical formalism developed by Nitzan *et al*. [57] has been followed, in which the molecule is approximated by a cylindrical conductor of diameter σ, and electric field screening length λ. As discussed by the authors, the screening length in molecular conductors is an open question, and systems with small HOMO-LUMO gaps are expected to screen well. Assuming that screening over the characteristic length of our system can be described by a Poisson formalism, the voltage division parameter describing the electrostatic potential profile can be written as:

$$\eta(L_R) = \eta_0(L_R) + \frac{A}{\pi}\sum_{m=1}^{\infty}\frac{F_m}{m(1+F_m)} sin\left(\frac{2\pi m}{L_L+L_R}L_R\right) + \eta_{shift}, \quad (5.4)$$

where $\eta_0(z)$ is the linear profile given in *Equation 5.3*. *A* is a factor to correct for the voltage drop in the Fc. The coefficients F_m can be expressed analyticaly as:

$$F_m = \frac{1}{2}\left(\frac{\sigma}{\lambda}\right)^2 e^{\chi}\int_{\chi}^{\infty} du\,\frac{e^{-u}}{u}, \quad (5.5)$$

with,

$$\chi = \frac{1}{2}\left(2\pi m\frac{\sigma}{\lambda}\right)^2, \quad (5.6)$$

Using σ = 2.38 Å (= 0.125($L_L + L_R$)), which is taken as the effective diameter of the alkyl chain, the electrostatic potential profiles for different screening lengths (λ = 0.95, 1.50, 1.90 and

2.85 Å) are shown in Figure 49. It can be clearly observed that the departure from linear behavior is more pronounced as the screening length decreases. In the limit $\lambda \to 0$ the electrostatic potential will follow the electrochemical potential and drop entirely within the vicinity of the contacts.

The results of the corresponding fittings of the rectification data are shown in Figure 47 for three screening lengths: λ = 1.30 Å (black line), λ = 1.50 Å (blue line) and λ = 1.90 Å (green line). From the good quantitative agreement with the experimental results, where the small slope in the rectification ratio can be well accounted for at intermediated values of n, one can estimate the characteristic screening length to be approximately $\lambda = 1.50 \pm 0.2$ Å. These values of the screening length are comparable to the molecular diameter σ, indicating that the electric field lines from vacuum penetrate well into the molecule.

CHAPTER 6:
CONCLUSIONS

This thesis presents a complex temperature-dependent behavior of charge transport phenomena in molecular tunnel junctions over a wide range of bias and gate voltages. The results in *Chapter 4* demonstrate that a formal single-level transport model can satisfactorily explain the different conduction regimes, including the Coulomb blockade, the charge degeneracy points and intermediate situation between both.

These observations are rationalized by a Landauer-type single-level model, assuming coherent sequential tunnelling in electrode-molecule-electrode junction (*Chapter 3*). The thermal broadening of the Fermi distributions of the occupation energies of the electrons in the leads explains the complex temperature-dependent tunneling behavior without the need of invoking classical (Marcus-like) relaxation processes.

The work shows the validity of the analytical single-level tunneling model that uses experimentally obtained input parameters, such as γ, η, and ε, to calculate *I-V* curves. *Chapter 5* confirms the expectation that potential profiles in insulating molecules are neither linear (as in vacuum) nor follow the electrochemical potential profile, which would lead to flat profiles within the entire length of the molecule and would prevent the attainment of high rectification ratios by capacitive coupling with the active transport unit.

The single-level model is tested against well-characterized molecular diodes and faithfully recovers the temperature dependent behavior and the rectification ratio of the junctions. Thus, it is applicable to describe transport data from both single molecule and SAM-based junctions where intra-molecular collective behavior is not significant.

Finally, this thesis analyzes a simple single-level transport model that can account for the typical temperature dependencies of the conductance in solid state junctions and provide a powerful analysis tool to extract the characteristic parameters governing tunneling in these junctions in a consistent way. The results represent an important step forward in explaining the temperature-dependent charge transport measurements observed in single-molecule tunneling junctions and hopefully help to improve existing models of charge transport. In future directions, comparative measurements in SETs and SAM-based junctions for different kinds of molecules will stand as an essential tool to establish the nature of electrical conduction in molecular tunnel junctions for temperature-dependence behavior.

APPENDIX A:
TABLES FOR FABRICATION

A*ppendix A* wants to be a quick access to the tables for the nanobafrication detailed in *Chapter 2*.

NOTE: These are just the parameters, for the recipes see Chapter 2. All the metal depositions are conducted by electron-beam evaporation at high vacuum conditions (< 5 10^{-6} Torr).

Table 3: Specification for the Si/Sio2 wafers used in the fabrication of the Single-electron transistors.

3" N/Phosphorous (100) 1-10 ohm-cm 380um SSP Prime WITH 1 um (micron) of THERMAL OXIDE
From UniversityWafer.com

Photolithography

Table 4: Parameters for the spin coating of the photoresists: LOR 3A and Shipley S1813.

LOR 3A	Shipley S1813
2s at 500rpm / 30s at 3000rpm / 2s at 0rpm	**2s at 500rpm / 30s at 5000rpm / 2s at 0rpm**

Table 5: O_2 plasma parameters for the cleaning procedure before every evaporation in the photolithography process. SCCM stands for standard cubic centimeter per minute.

SCCM	Power	Pressure	Time
5	**50 W**	**200 mTorr**	**10 s**

Table 6: E-beam evaporation parameters for first metal layer in the photolithography process.

	Ti	Pd
Density	**4.5 g/cm^3**	**12 g/cm^3**
Z-ratio	**0.628**	**0.357**
Deposition Rate	**1 Å/s**	**0.4 Å/s**
Thickness	**5 nm**	**15 nm**
Current	**~30 mA**	**~30 mA**

Table 7: E-beam evaporation parameters for second metal layer in the photolithography process.

	Ti	Pd
Density	**4.5 g/cm^3**	**12 g/cm^3**
Z-ratio	**0.628**	**0.357**
Deposition Rate	**1 Å/s**	**1.4 Å/s**
Thickness	**10 nm**	**70 nm**
Current	**~30 mA**	**~40 mA**

Table 8: E-beam evaporation parameters for third metal layer in the photolithography process.

	Al
Density	**2.7 g/cm^3**
Z-ratio	**1.08**
Deposition Rate	**0.6 Å/s**
Thickness	**35 nm**
Current	**~200 mA**

Table 9: Parameters for the oxidation of aluminum gates in O_2 plasma. SCCM stands for standard cubic centimeter per minute.

SCCM	Power	Pressure	Time
12	**50 W**	**100 mTorr**	**10 min**

E-beam Lithography

Table 10: Parameters for the spin coating of the e-beam resists: MMA (8.5) EL 6 and 950 PMMA C 2.

MMA (8.5) EL 6	950 PMMA C 2
2s at 500 rpm / 60s at 4000 rpm / 2s at 0 rpm	2s at 500 rpm / 60s at 6000 rpm / 2s at 0 rpm

Table 11: E-beam evaporation parameters for first metal layer in the e-beam lithography process.

	Au
Density	**19.3 g/cm^3**
Z-ratio	**0.381**
Deposition Rate	**1.5 Å/s**
Thickness	**15 nm**
Current	**~ 50 mA**

Table 12: E-beam evaporation parameters for second metal layer in the e-beam lithography process.

	Au
Density	**19.3 g/cm^3**
Z-ratio	**0.381**
Deposition Rate	**1.5 Å/s**
Thickness	**50 nm**
Current	**~ 50 mA**

Table 13: Wire bonding (K&S 4123) parameters. 1st bond attaches to the copper (in the sample carrier) and 2nd bond to the main contacts in the SET. Search denominates the high difference between both surfaces. These are guidance starting parameters.

	Search (high at which the Bonding Head stops)	Force (by the electromagnetic coil)	Time (10 maximum bonding time of 1000 ms)	Power (0 LOW -100 HIGH vibration amplitude)
1st bond	**000**	**4.6**	**5.2**	**456**
2nd bond	**020**	**0.9**	**1.1**	**100**

APPENDIX B:
THE TUNNEL EQUATION

The Tunnel Equation - Simmons Model

The Simmons model applies to thin tunnel junctions making an approximation to the actual thickness of the insulating film in the junction based on *I-V* curves [59]. This is a model in which parameters such as the cross-section area, metal work function, asymmetry of the potential barrier and length of the barrier have to run comparatively with the measurements taken in the lab, being very useful to characterize broken nanowires and have a better understanding of the breaking process.

To check a proper functional nanogap for the SET, it is necessary to solve the physics problems associated to the single-barrier problem. Figure 50 shows an energy diagram of a single barrier schematic where the black area denominates the insulating film with a thickness, s. The barrier is sandwiched by two metal electrodes (source and drain), in grey, whose Fermi energy is represented by its electrochemical potential (μ_S and μ_D, respectively). The minimum energy required to remove one electron from the electrodes is the work function, represented by Φ, which the model assumes that is the same for both electrodes. Although, for this scenario it is clear that the work function is lower than the potential barrier in the junction, at the nanoscale this does not mean that the probability of having an electron tunneling through the potential barrier is zero.

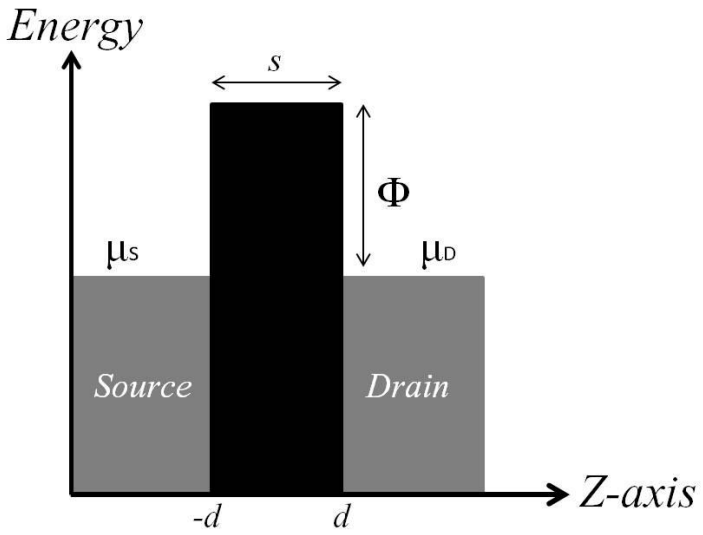

Figure 50: Schematic diagram of a thin insulating film acting as a potential barrier. The potential barrier distance, s, is the separation between the source and the drain electrodes. The energy difference between the source/drain Fermi energies (represented by its electrochemical potentials, μ_S and μ_D, respectively) and the potential barrier is the work function, Φ.

Solving Schödinger's equation for the wave function of a conduction electron, in the three regions of the space in Figure 50, gives the solution:

$$\Phi(z) = \begin{cases} \Phi_1(z) = I_1 e^{ik_1 z} + R_1 e^{-ik_1 z} & z \leq -d \\ \Phi_2(z) = I_2 e^{k_2 z} + R_2 e^{-k_2 z} & 0 < z < d \\ \Phi_3(z) = I_3 e^{ik_1 z} & x \geq d \end{cases} \quad \text{(B.1)}$$

with $k_1 = 8\pi^2 mE/h^2$ and $k_2 = 8\pi^2 m(V-E)/h^2$

With *Equation B.1* and applying the continuity conditions between the regions, we can extract the coefficient of transition or tunnel probability:

$$T = \frac{|I_3|^2}{|I_1|^2} = \left[1 + \frac{1}{4}\left(\frac{{k_1}^2 + {k_2}^2}{k_1 k_2}\right)^2 sinh^2(k_2 d)\right]^{-1} \quad \text{(B.2)}$$

The coefficient of transition is a quantum effect only and it is due to the wave nature of microscopic systems. So, the electron can jump from one electrode to the other through the potential barrier with a certain probability.

Now, reviewing the model of tunnel conduction (Simmons original article) two different work functions are expected for the two electrodes. In our derivation the terms $\Phi_1 + \Phi_2 \pm eV$ are replaced by $\Phi \pm eV/2$, since we assume the same work function for both electrodes. Moreover, Simmons derives the equation for three different scenarios depending on the voltage range compared to the work function value of the metal. In solid state devices the work function of the metals ranges between 0.1-1 *eV* due to energy renormalization effects in the junction. Consequently, using the WKB approximation for only the intermediate-voltage range ($V < \Phi/e$) [59], the current flowing through the barrier is:

$$J = \left(\frac{e}{2\pi h s^2}\right)\left\{\left(\Phi - \frac{eV}{2}\right) e^{\left[-\frac{4\pi s}{h}\sqrt{2m}\sqrt{\Phi - \frac{eV}{2}}\right]} - \left(\Phi + \frac{eV}{2}\right) e^{\left[-\frac{4\pi s}{h}\sqrt{2m}\sqrt{\Phi + \frac{eV}{2}}\right]}\right\} \qquad \text{(B.3)}$$

and by expanding the square root in the same voltage range for *Equation B.3*, the current density tunneling through the junction (plotted in Figure 51) is given by:

$$J \approx \left(\frac{e}{\pi h s^2}\right) \Phi e^{-\frac{2\pi s\sqrt{2m\Phi}}{h}} sinh\left(\frac{2\pi e s}{h}\sqrt{\frac{m}{2\Phi}}V\right) \qquad \text{(B.4)}$$

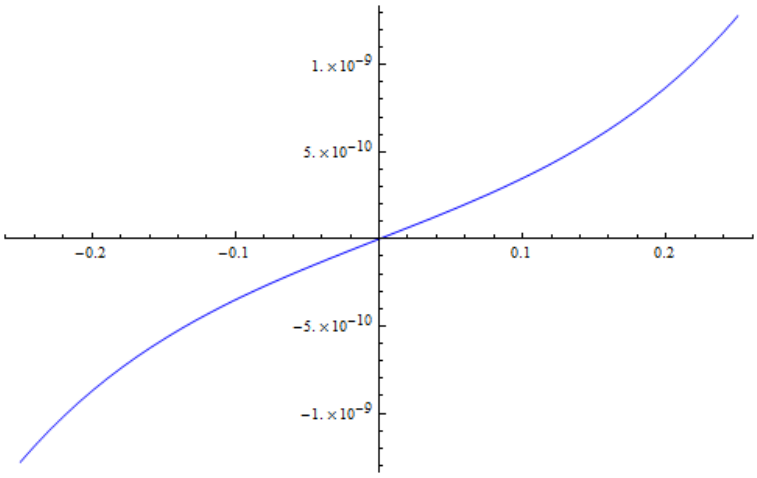

Figure 51: Calculation of the current density tunneling through a tunnel junction, current density, in A/m^2, in the *y-axis* and Voltage, in V, in the *x-axis*. *Equation B.4* has been used for the calculation with the following parameters: Φ = 0.51*eV* (approximately the gold work function at solid state devices) and s = 2nm.

There is another approximation in order to have a faster reading of the thickness of the insulating film in the junction with certain accuracy. While the Simmons model takes all the values for the current in a voltage range giving quite corrected results, by reading the value of the resistance it is possible to get an estimation of the separation by the electrodes as reported by Morpurgo, *et al.* [60]. This system is not as reliable as the Simmons model although it can give a certain approximation to the actual size of the gap.

Wolfram Mathematica Code for Simmons Model

Here the Simmons Model adapted for Wolfram Mathematica program with Whitside and Lindsay modifications which include: the replacements of the electron mass for the effective electron mass, m*, and the material and geometry asymmetry parameter [61, 62].

```
(* Where the Measure Current data file is located. The file must end in n0 *)

SetDirectory["C:\\Users\\delBarco\\Desktop\\Alvar\\Simmons model\\"];

(* Constants *)

e = 1.60217657 10^-19;          (* Electron's charge in C *)
h = 6.62606957 10^-34;          (* Planck's constant in J s *)
m = 10^-30;                     (* Effective mass in the insulating part in kg *)

(* Parameters *)

w = 10 10^-9 ;                  (* Width of the nanowire at the constriction in m *)
t = 5 10^-9 ;                   (* Thickness of the nanowire at the constriction in m *)
A = w t;                        (* Area of the tunnel junction in m2 *)

Φ1 = 00.40 ;                    (* Initial work function for the Source and Drain metals in V *)
Φ2 = 00.80 ;                    (* Final work function in V *)
Φ = 00.10 ;                     (* Increment in the work function steps V *)

L0 = 01.5 10^-9;                (* Minimum length of the tunnel junction in m *)
L = 02.5 10^-9;                 (* Maximum length of the tunnel junction in m *)
AL = 0.5 10^-9;                 (* Increment in the evaluation length of the tunnel junction in m *)

VbI = -0.200 ;                  (* Initial value for Voltage Bias in V *)
VbF = 0.200 ;                   (* Final value for Voltage Bias in V *)
AVb = 0.002 ;                   (* Increment on Voltage Bias in V *)

α = 0.50 ;                      (* Asymmetry parameter from 0 to 1, 1/2 gives original Simmons
model; symmetric barrier with respect to the electrodes*)

Filename = "IVL01n" ;           (* MEASURED FILE NAME *)

ΦMax = Round[1+ ((Φ2-Φ1)/AΦ)];

LMax = Round[1+ ((L-L0)/AL)];

VbMax = Round[1+ ((VbF-VbI)/AVb)];

VbMax1 = VbMax+1;

VbMax2 = VbMax+2;
```

```
Print[ Style[LMax "different gap sizes", Purple,Bold,20]];                    (* Number of gaps*)

Print[ Style[ΦMax "different work functions values", Purple,Bold,20]];    (* Number of Work Functions*)

Print[Style[VbMax "points for every graph (ΔV)", Purple,Bold,20]];          (* Number of points in the graphs *)


(* Create & Write file with Measure and Calculated Current IN ROWS *)

Newfilename = "SimmonsModel";
strm = OpenWrite[Newfilename<>".dat"];

WriteString[strm,FortranForm[voltage]];
WriteString[strm," "];
WriteString[strm,FortranForm[volts]];
WriteString[strm," "];

Print[ Style["Organizing data...", Purple,Bold,19]];

xcolumn = Import[Filename<>"0.dat","Table"];

For[j = 1, j < VbMax1, j++,
Voltage = xcolumn[[j,1]];
WriteString[strm,FortranForm[N[Voltage]]];
WriteString[strm," "];
];
WriteString[strm,"\n"];

WriteString[strm,FortranForm[current]];
WriteString[strm," "];
WriteString[strm,FortranForm[amperes]];
WriteString[strm," "];

For[i = 0, i < 1, i++,
Experimentaldata = Import[Filename <>ToString[i]<>".dat","Table"];
For[j = 1, j < VbMax1, j++,
Icurrent = Experimentaldata[[j,2]];
WriteString[strm,FortranForm[N[Icurrent]]];
WriteString[strm," "];
        ];
];
WriteString[strm,"\n"];
```

```
Print[ Style["Calculating data...", Purple,Bold,19]];

For[s = L0, s < L + AL, s += AL,
For[Φ = Φ1, Φ < Φ2 + AΦ, Φ += AΦ,
WriteString[strm,FortranForm[N[s]]];                    (* Adding gap size *)
WriteString[strm," "];
WriteString[strm,FortranForm[N[Φ]]];                    (* Adding work function value *)
WriteString[strm," "];
For[V = VbI, V < VbF + AVb, V += AVb,

Current=((e^2 A)/(2 π h s^2)) ((Φ - α V) E^(- ((4 π s)/h) Sqrt[2 m e] Sqrt[(Φ - α V)])-( Φ +(1-α)
V) E^(- ((4 π s)/h) Sqrt[2 m e] Sqrt[(Φ +(1-α) V)]));

WriteString[strm,FortranForm[N[Current]]];
WriteString[strm," "];
        ];
WriteString[strm,"\n"];
        ];
];

(* Transpose Calculated file *)

Trans = Import["SimmonsModel.dat","Table"];
Export["SimmonsModel.dat",Transpose[Trans]];

Close[strm];

Print[Style["Data organized and calculated!", Orange, Bold, 25]] ;
```

Wolfram Mathematica Code for Capacitances, Gate Coupling and Change in Spin

```
(* Parameters *)

(* First enter 3 values for Vbd (this slope "/") with 3 values for Vg *)
(* For Drain electrode *)

Vbd1 = 76 10^-3;          Vg1 = 1.18 ;          (* in V *)
Vbd2 = 48 10^-3;          Vg2 = 0.82 ;          (* in V *)
Vbd3 = -62 10^-3;         Vg3 = -0.54 ;         (* in V *)

(* Now enter 3 values for Vbs (this slope "\") with 3 values for Vg *)
(* For Source electrode *)

Vbs1 = 88 10^-3;          Vg4 = -0.66 ;         (* in V *)
Vbs2 = 36 10^-3;          Vg5 = -0.14 ;         (* in V *)
Vbs3 = -70 10^-3;         Vg6 = 0.90 ;          (* in V *)

(* Constants and Parameters for the changing in Spin *)

e = 1.60217657 10^-19;                          (* Electron charge in C *)
g = 2.002319304386;
μb = 5.78838 10^-5;                             (* in eV/T *)


B = 7;                                          (* in T *)
Vci = 0.63;                                     (* in V @ 0 B in T*)
Vcf = 0.61;                                     (* in V @ B in T*)


(* Code *)

data = {{Vg1,Vbd1},{Vg2,Vbd2},{Vg3,Vbd3}};
line1 = Fit[data,{1,Vg},Vg];


(* this slope "/" *)
x = line1[[2]];                                 (* x = Cg/(Cg+Cd) *)

data2 = {{Vg4,Vbs1},{Vg5,Vbs2},{Vg6,Vbs3}};
line2 = Fit[data2,{1,Vg},Vg];

(* this slope "\" *)
y = line2[[2]];                                 (* y = -(Cg/Cs) *)
```

```
Vg = 1;

Cd = ((1 - x) / x) Cg;                          (* Cd = Drain capacitance *)
Cs = - (Cg / y);                                (* Cs = Source capacitance *)


Cg = 1;                                         (* Cg = Gate capacitance *)

β = 1/(1 – 1 / y + (1 - x) / x);                (* β=Cg/(Cg+Cs+Cd) *) (*Gate Coupling*)

(* Print["x = Cg/(Cg+Cd) = ", Round[x,0.001],"     ","y = = -Cg/Cs = " ,Round[y,0.001]] *)

Print["Cg:Cs:Cd = ",Cg,":",Round[Cs,0.1],":",Round[Cd,0.1]]
Print["β = ",Round[β,0.001]];

ΔS = (β (Vcf - Vci))/( - 2 g μb B);      (* ΔS = (β ΔVc)/( - 2 g μb B) = ΔS (N+1)-ΔS (N) *)


Print["ΔS = ",Round[ΔS,0.01]];

Clear[Vg];
Clear[Cg];

(*

Equations for Capacitances and Gate Coupling

Vbd = Cg / (Cg + Cd) (Vg - Vc);       (* this slope "/" *)
x = Cg / (Cg + Cd);
Vbs = - (Cg / Cs) (Vg - Vc);   (* this slope "\" *)
y = - (Cg / Cs);

Cd = (1 - x) / x Cg;
Cs = Cg / y;
Ct = Cg + Cs + Cd;
β = 1 / (1 + 1 / y + (1 - x) / x); (* β=Cg/(Cg+Cs+Cd) *)

Equations for the change in Spin

e ΔVc = (- 2 g μb B ΔS) / β; ΔS=ΔS (N+1) - ΔS (N)

*)
```

APPENDIX C:
THE SINGLE-LEVEL TUNNELING MODEL FORMALISIM

The mathematical formalism for the temperature-dependent single-level tunnelling model in *Chapter 3* was completed in collaboration with Dr. Mucciolo in the department of physics of University of Central Florida.

The Rate Equation Formulation

Let *M* be the number of spin-split orbitals in the molecule. The number of possible electronic configurations is equal to $n = 2^M$ (i.e., each orbital can be empty or occupied). Each configuration can be described by a set of occupation numbers $c_\alpha(i)$, with $\alpha = 1, \ldots, n$ and $i = 1, \ldots, M$, where

$$c_\alpha(i) = 0 \text{ or } 1 \tag{C.1}$$

depending on whether the *i*-th orbital is occupied or not.

Call P_α the probability of the configuration, with $P_\alpha \geq 0$ and $\sum_{\alpha=1}^{n} P_\alpha = 1$. The rate equation governing the change in the configuration probabilities over time is equal to

$$\frac{dP_\alpha}{dt} = -P_\alpha \sum_{\beta \neq \alpha} \Gamma_{\alpha \to \beta} + P_\beta \sum_{\beta \neq \alpha} \Gamma_{\beta \to \alpha} \tag{C.2}$$

where $\Gamma_{\alpha \to \beta}$ is the rate of the $\alpha \to \beta$ transition. We can rewrite this equation in matrix form,

$$\frac{dP_\alpha}{dt} = \sum_\beta \Lambda_{\alpha\beta} P_\beta \tag{C.3}$$

where

$$\Lambda_{\alpha\beta} = \begin{cases} -\sum_{\gamma \neq \alpha} \Gamma_{\alpha \to \gamma}, if\ \alpha = \beta \\ \Gamma_{\beta \to \alpha}, if\ \alpha \neq \beta \end{cases} \tag{C.4}$$

Notice that, consistent with the normalization condition, we have

$$\sum_{\alpha=1}^{n} \frac{dP_\alpha}{dt} = -\sum_{\alpha=1}^{n} P_\alpha \sum_{\beta \neq \alpha} \Gamma_{\alpha \to \beta} + \sum_{\alpha=1}^{n} \sum_{\beta \neq \alpha} \Gamma_{\beta \to \alpha} P_\beta \tag{C.5}$$

$$\sum_{\alpha=1}^{n} \frac{dP_\alpha}{dt} = -\sum_{\alpha=1}^{n} P_\alpha \sum_{\beta \neq \alpha} \Gamma_{\alpha \to \beta} + \sum_{\beta=1}^{n} P_\beta \sum_{\alpha \neq \beta} \Gamma_{\beta \to \alpha}, \tag{C.6}$$

$$\sum_{\alpha=1}^{n} \frac{dP_\alpha}{dt} = 0 \tag{C.7}$$

implying that

$$\sum_{\alpha=1}^{n} \Lambda_{\alpha\beta} = 0 \tag{C.8}$$

as it can be easily verified. On the other hand,

$$\sum_{\beta=1}^{n} \Lambda_{\alpha\beta} = -\sum_{\gamma \neq \alpha} \Gamma_{\alpha \to \gamma} + \sum_{\beta \neq \alpha} \Gamma_{\beta \to \alpha} \tag{C.9}$$

$$\sum_{\beta=1}^{n} \Lambda_{\alpha\beta} = \sum_{\beta \neq \alpha} (\Gamma_{\beta \to \alpha} - \Gamma_{\alpha \to \beta}) \tag{C.10}$$

Thus, if $\Gamma_{\beta \to \alpha} = \Gamma_{\alpha \to \beta}$ for all transitions, then the r.h.s. of this equation is equal to zero. This means that a trivial stationary solution exits where $P_\alpha = 1/n$ for all $\alpha = 1, \ldots, n$. However, when $\Gamma_{\beta \to \alpha} \neq \Gamma_{\alpha \to \beta}$, other nontrivial stationary solution exist as well.

Stationary Solutions

In order to obtain a stationary solution to the rate equations set

$$\frac{dP_\alpha}{dt} = 0 \tag{C.11}$$

for all $\alpha = 1, \ldots, n$. This implies

$$\sum_{\beta} \Lambda_{\alpha\beta} P_\beta = 0 \tag{C.12}$$

Thus, to find the set of stationary probabilities { P_α }, one needs to find the right eigenvector corresponding to the zero eigenvalue of the matrix Λ.

Transition Rates

Let E_α be the total energy of the molecule and N_α be the total number of electrons in the α configuration. When an electron hops from one of the leads and into the molecule, energy conservation requires

$$\varepsilon + E_\alpha = E_\beta \tag{C.13}$$

where $\alpha(\beta)$ is the molecule's configuration before/after the hopping and ε is the energy of the electronic state in the lead. For this transition to take place, the state with energy ε in the lead must have a finite occupation number, namely $f\left(\frac{\varepsilon-\mu_l}{k_BT}\right) > 0$, where μ_l is the lead's chemical potential ($l = R, L$) and T is the temperature. Here, $f(x)$ denotes the Fermi-Dirac distribution,

$$f(x) = \frac{1}{e^x+1} \tag{C.14}$$

In the opposite case, when an electron hops from the molecule and into the lead, we have

$$E_\alpha = \varepsilon + E_\beta \tag{C.15}$$

Now, the occupation number of the state with energy ε must be such that $f\left(\frac{\varepsilon-\mu_l}{k_BT}\right) < 1$.

Call γ_R and γ_L the level widths due to the coupling to the right and left leads, respectively. We can split the transition rate into two contributions,

$$\Gamma_{\alpha\to\beta} = \Gamma^{\mathrm{R}}_{\alpha\to\beta} + \Gamma^{\mathrm{L}}_{\alpha\to\beta} \tag{C.16}$$

where

$$\Gamma^{l}_{\alpha\to\beta} = \begin{cases} \left(\frac{\gamma_l}{\hbar}\right) f\left(\frac{E_\beta - E_\alpha - \mu_l}{k_B T}\right), if\ N_\beta = N_\alpha + 1\ and\ d_H(c_\beta, c_\alpha) = 1 \\ \left(\frac{\gamma_l}{\hbar}\right)\left[1 - f\left(\frac{E_\alpha - E_\beta - \mu_l}{k_B T}\right)\right], if\ N_\beta = N_\alpha - 1\ and\ d_H(c_\beta, c_\alpha) = 1, \\ 0, \text{otherwise} \end{cases} \quad l=R,L, \tag{C.17}$$

where d_H (c_β, c_α) is the Hamming distance between the binary sets c_β and c_α . Namely, only transitions where the number of electrons in the molecule changes by one are allowed. Notice that the bias voltage is equal to $V = (\mu_L - \mu_R)/e$, where e denotes the electron charge.

The rate equation approach is valid when $k_B T \gg \gamma_{R,L}$ (since it assumed a perfectly sharp energy level in the molecule), and when the tunneling through the molecule is sequentially incoherent. Below, we discuss the validity of the rate equation in more detail.

Implicit in *Equation C.17* is the assumption that the molecule's energy levels are sharp, such that γ_R, γ_L are much smaller than other energy scales of the problem, such as $k_B T$, eV , and the separation of energy levels in the molecule.

Current

The current coming from the left lead is equal to

$$I_L = -e \sum_{\alpha,\beta} \Delta N_{\alpha\to\beta} \Gamma^{\mathrm{L}}_{\alpha\to\beta} \mathrm{P}_\alpha \tag{C.18}$$

where $\Delta N_{\alpha\to\beta} = N_\beta - N_\alpha$

Total Energy

The total energy in the molecule can be broken down as follows (constant charging energy model):

$$E_\alpha = \frac{1}{2}N_\alpha(N_\alpha - 1)E_c - eV_gN_\alpha + \sum_{i=1}^{M} c_\alpha(i)\varepsilon_i \quad \text{(C.19)}$$

where E_c is the charging energy, V_g is the gate voltage, and $\{\varepsilon_i\}_{i=1\ ,\dots\ ,\ M}$ are the energies of the orbitals.

Single-level Case

Let us apply this formulation compute the stationary current of a molecule with a single orbital (spinless case), in which case $M = 1$ and $n = 2$. $P_0(1)$ corresponds to the probability of the empty/filled state. The stationary problem is defined by the matrix

$$\Lambda = \begin{pmatrix} -\Gamma_{0\to1} & \Gamma_{1\to0} \\ \Gamma_{0\to1} & -\Gamma_{1\to0} \end{pmatrix} \quad \text{(C.20)}$$

where

$$\Gamma_{0\to1} = \Gamma_{0\to1}^{R} + \Gamma_{0\to1}^{L} \quad \text{(C.21)}$$

and

$$\Gamma_{1\to0} = \Gamma_{1\to0}^{R} + \Gamma_{1\to0}^{L} \quad \text{(C.22)}$$

with

$$\Gamma_{0\to1}^{l} = \left(\frac{\gamma_l}{\hbar}\right) f\left(\frac{E_1 - E_0 - \mu_l}{k_BT}\right), l = L, R \quad \text{(C.23)}$$

and

$$\Gamma_{1\to 0}^{l} = \left(\frac{\gamma_l}{\hbar}\right)[1 - f\left(\frac{E_1 - E_0 - \mu_l}{k_B T}\right)], l = L, R \tag{C.24}$$

The eigenvector of the Λ matrix with zero eigenvalue corresponds to

$$P_0 = \frac{\Gamma_{1\to 0}}{\Gamma_{1\to 0}\Gamma_{o\to 1}} = \frac{\hbar\Gamma_{1\to 0}}{\gamma_R + \gamma_L} \tag{C.25}$$

and

$$P_1 = \frac{\Gamma_{0\to 1}}{\Gamma_{1\to 0}\Gamma_{o\to 1}} = \frac{\hbar\Gamma_{0\to 1}}{\gamma_R + \gamma_L} \tag{C.26}$$

The current coming from the left lead is equal to

$$I_L = -e(P_0\Gamma_{0\to 1}^{L} - P_1\Gamma_{1\to 0}^{L}) \tag{C.27}$$

$$I_L = -\frac{e\hbar}{\gamma_R + \gamma_L}(\Gamma_{1\to 0}\Gamma_{0\to 1}^{L} - \Gamma_{o\to 1}\Gamma_{1\to 0}^{L}) \tag{C.28}$$

$$I_L = -\frac{e\hbar}{\gamma_R + \gamma_L}(\Gamma_{1\to 0}^{R}\Gamma_{0\to 1}^{L} - \Gamma_{o\to 1}^{L}\Gamma_{1\to 0}^{L}) \tag{C.29}$$

$$I_L = -\frac{e}{\hbar}\frac{\gamma_R\gamma_L}{\gamma_R + \gamma_L}\{\left[1 - f\left(\frac{E_{10} - \mu_R}{k_B T}\right)\right] f\left(\frac{E_{10} - \mu_L}{k_B T}\right) - f\left(\frac{E_{10} - \mu_R}{k_B T}\right)\left[1 - f\left(\frac{E_{10} - \mu_L}{k_B T}\right)\right]] \tag{C.30}$$

$$I_L = -\frac{e}{\hbar}\frac{\gamma_R\gamma_L}{\gamma_R + \gamma_L}[f\left(\frac{E_{10} - \mu_L}{k_B T}\right) - f\left(\frac{E_{10} - \mu_R}{k_B T}\right)] \tag{C.31}$$

where $E_{10} = E_1 - E_0 = -eV_g + \varepsilon_1$.

Finite Level Width

When the broadening of the energy level is not negligible, we have to modify the calculations to account for the uncertainty in ε_1. Let γ be the total level width and $D1(\varepsilon)$ the density of state profile associated to the single-level configuration; for instance, consider the Lorentzian profile

$$D_1(\epsilon) = \frac{1}{\pi}\frac{\frac{\gamma}{2}}{(\epsilon-\epsilon_1)^2+(\frac{\gamma}{2})^2} \tag{C.32}$$

with $\int d\varepsilon\ D_1(\varepsilon) = 1$. The modified expressions for the transition rates are

$$\Gamma_{0\to1}^{l} = \left(\frac{\gamma_l}{\hbar}\right)\int d\varepsilon\ D_1(\varepsilon) f\left(\frac{E_1-E_0-\mu_l}{k_BT}\right), l = L, R \tag{C.33}$$

and

$$\Gamma_{1\to0}^{l} = \left(\frac{\gamma_l}{\hbar}\right)\int d\varepsilon\ D_1(\varepsilon)[1 - f\left(\frac{E_1-E_0-\mu_l}{k_BT}\right)], l = L, R \tag{C.34}$$

where

$$E_1 - E_0 = -eV_g + \varepsilon \tag{C.35}$$

Notice that

$$\Gamma_{0\to1}^{R} + \Gamma_{1\to0}^{R} = \left(\frac{\gamma_R}{\hbar}\right)\int d\varepsilon\ D_1(\varepsilon) = \frac{\gamma_R}{\hbar} \tag{C.36}$$

and

$$\Gamma_{0\to1}^{L} + \Gamma_{1\to0}^{L} = \left(\frac{\gamma_L}{\hbar}\right)\int d\varepsilon\ D_1(\varepsilon) = \frac{\gamma_L}{\hbar} \tag{C.37}$$

Therefore,

$$\Gamma_{0\to1} + \Gamma_{1\to0} = (\gamma_R + \gamma_L)/\hbar \tag{C.38}$$

$$P_0 = \frac{1}{\gamma_R+\gamma_L}\int d\varepsilon\ D_1(\varepsilon)\sum_l \gamma_l[1 - f\left(\frac{E_1-E_0-\mu_l}{k_BT}\right)] \tag{C.39}$$

$$P_0 = \frac{1}{\gamma_R+\gamma_L}\sum_l \gamma_l \int d\varepsilon\, D_1\big(\varepsilon + eV_g\big)[1 - f\left(\frac{\varepsilon-\mu_l}{k_BT}\right)] \tag{C.40}$$

and

$$P_0 = \frac{1}{\gamma_R+\gamma_L}\int d\varepsilon\ D_1(\varepsilon)\sum_l \gamma_l f\left(\frac{E_1-E_0-\mu_l}{k_BT}\right) \tag{C.41}$$

$$P_0 = \frac{1}{\gamma_R+\gamma_L}\sum_l \gamma_l \int d\varepsilon\, D_1\big(\varepsilon + eV_g\big) f\left(\frac{\varepsilon-\mu_l}{k_BT}\right) \tag{C.42}$$

Going back to the expression defining the current through the left lead, we find

$$I_L = -e(P_0\Gamma^L_{0\to1} - P_1\Gamma^L_{1\to0}) \tag{C.43}$$

$$I_L = -\frac{e}{\hbar}\frac{1}{\gamma_R+\gamma_L}(\Gamma_{1\to0}\Gamma^L_{0\to1} - \Gamma_{o\to1}\Gamma^L_{1\to0}) \tag{C.44}$$

$$I_L = -\frac{e}{\hbar}\frac{1}{\gamma_R+\gamma_L}[(\Gamma^R_{1\to0}\Gamma^L_{1\to0})\Gamma^L_{0\to1} - (\Gamma^R_{o\to1}\Gamma^L_{0\to1})\Gamma^L_{1\to0}] \tag{C.45}$$

$$I_L = -\frac{e}{\hbar}\frac{1}{\gamma_R+\gamma_L}[\Gamma^R_{1\to0}\Gamma^L_{0\to1} - \Gamma^R_{o\to1}\Gamma^L_{1\to0}] \tag{C.46}$$

$$I_L = -\frac{e}{\hbar}\frac{\gamma_R\gamma_L}{\gamma_R+\gamma_L}\int d\varepsilon\ D_1(\varepsilon)\int d\varepsilon'\ D_1(\varepsilon')\{\left[1 - f\left(\frac{-eV_g+\varepsilon-\mu_R}{k_BT}\right)\right] f\left(\frac{-eV_g+\varepsilon'-\mu_L}{k_BT}\right) - f(\frac{-eV_g+\varepsilon-\mu_R}{k_BT})[1 - f(\frac{-eV_g+\varepsilon'-\mu_L}{k_BT})]\} \tag{C.47}$$

$$I_L = -\frac{e}{\hbar}\frac{\gamma_R\gamma_L}{\gamma_R+\gamma_L}\int d\varepsilon\ D_1(\varepsilon)\int d\varepsilon'\ D_1(\varepsilon')\{f\left(\frac{-eV_g+\varepsilon'-\mu_L}{k_BT}\right)-f(\frac{-eV_g+\varepsilon-\mu_R}{k_BT})\} \quad (C.48)$$

$$I_L = -\frac{e}{\hbar}\frac{\gamma_R\gamma_L}{\gamma_R+\gamma_L}\int d\varepsilon\ D_1(\varepsilon)[f\left(\frac{-eV_g+\varepsilon-\mu_L}{k_BT}\right)-f\left(\frac{-eV_g+\varepsilon-\mu_R}{k_BT}\right)] \quad (C.49)$$

$$I_L = -\frac{e}{\hbar}\frac{\gamma_R\gamma_L}{\gamma_R+\gamma_L}\int d\varepsilon\ D_1(\varepsilon+eV_g)[f\left(\frac{\varepsilon-\mu_L}{k_BT}\right)-f\left(\frac{\varepsilon-\mu_R}{k_BT}\right)] \quad (C.50)$$

$$I_L = -\frac{e}{\hbar}\frac{\gamma_R\gamma_L}{\gamma_R+\gamma_L}\int d\varepsilon\ \frac{\gamma}{(\varepsilon-\varepsilon_1+eV_g)^2+(\gamma/2)^2}\left[f\left(\frac{\varepsilon-\mu_L}{k_BT}\right)-f\left(\frac{\varepsilon-\mu_R}{k_BT}\right)\right] \quad (C.51)$$

This expression generalizes the previous one, *Equation C.31*, to include a finite level width. It is straightforward to check that *Equation C.51* recovers *Equation C.31* when $\gamma \to 0$.

It is natural to assume that the total level width can be broken into three components,

$$\gamma = \gamma_R + \gamma_L + \gamma_0 \quad (C.52)$$

Where γ_0 represents the broadening caused by effects other than the leakage of charge through the leads.

Adding Spin

To add spin, we split the configuration where the molecule level is occupied into two (↑,↓), resulting in a total of three con gurations: i = 0,↑,↓ (we forbid double occupancy by assuming that the charging energy E_c is a very large energy scale, namely, $E_c >> k_BT, eV, |\varepsilon|$). Let us assume that the molecular level is spin degenerate. Then, the total current through the left lead is given by the expression

$$I_L = -e[P_0\left(\Gamma^L_{0\to\uparrow} + \Gamma^L_{0\to\downarrow}\right) - P_\uparrow\Gamma^L_{\uparrow\to 0} - P_\downarrow\Gamma^L_{\downarrow\to 0}] \tag{C.53}$$

The rate equations are

$$\frac{dP_0}{dt} = -P_0(\Gamma_{0\to\uparrow} + \Gamma_{0\to\downarrow}) + P_\uparrow\Gamma_{\uparrow\to 0} + P_\downarrow\Gamma_{\downarrow\to 0}] \tag{C.54}$$

$$\frac{dP_\uparrow}{dt} = -P_\uparrow\Gamma_{\uparrow\to 0} + P_0\Gamma_{0\to\uparrow}] \tag{C.55}$$

$$\frac{dP_\downarrow}{dt} = -P_\downarrow\Gamma_{\downarrow\to 0} + P_0\Gamma_{0\to\downarrow}] \tag{C.56}$$

Solving for the steady state yields

$$P_0 = \frac{\Gamma_{\uparrow\to 0}\Gamma_{\downarrow\to 0}}{\Gamma_{\uparrow\to 0}\Gamma_{\downarrow\to 0}+\Gamma_{0\to\uparrow}\Gamma_{\downarrow\to 0}+\Gamma_{0\to\downarrow}\Gamma_{\uparrow\to 0}} \tag{C.57}$$

$$P_\uparrow = \frac{\Gamma_{0\to\uparrow}\Gamma_{\downarrow\to 0}}{\Gamma_{\uparrow\to 0}\Gamma_{\downarrow\to 0}+\Gamma_{0\to\uparrow}\Gamma_{\downarrow\to 0}+\Gamma_{0\to\downarrow}\Gamma_{\uparrow\to 0}}, \tag{C.58}$$

$$P_\downarrow = \frac{\Gamma_{0\to\downarrow}\Gamma_{\uparrow\to 0}}{\Gamma_{\uparrow\to 0}\Gamma_{\downarrow\to 0}+\Gamma_{0\to\uparrow}\Gamma_{\downarrow\to 0}+\Gamma_{0\to\downarrow}\Gamma_{\uparrow\to 0}} \tag{C.59}$$

Assuming spin degeneracy in the leads, we find

$$\Gamma^l_{0\to\uparrow} = \Gamma^l_{0\to\downarrow} = \left(\frac{\gamma_l}{\hbar}\right)\int d\varepsilon\ D_1(\varepsilon) f\left(\frac{E_1-E_0-\mu_l}{k_BT}\right) \equiv \Gamma^l_{0\to 1}, l = L, R \tag{C.60}$$

and

$$\Gamma^l_{\uparrow\to 0} = \Gamma^l_{\downarrow\to 0} = \left(\frac{\gamma_l}{\hbar}\right)\int d\varepsilon\ D_1(\varepsilon)[1 - f\left(\frac{E_1-E_0-\mu_l}{k_BT}\right)] \equiv \Gamma^l_{1\to 0}, l = L, R \tag{C.61}$$

Therefore,

$$\Gamma_{0\to\uparrow} = \Gamma_{0\to\downarrow} = \int d\varepsilon\ D_1(\varepsilon)[\gamma_R f_R(\varepsilon) + [\gamma_L f_L(\varepsilon)] \equiv \Gamma_{0\to 1} \tag{C.62}$$

and

$$\Gamma_{\uparrow\to 0} = \Gamma_{\downarrow\to 0} = \int d\varepsilon\ D_1(\varepsilon)[\gamma_R + \gamma_L - \gamma_R f_R(\varepsilon) - \gamma_L f_L(\varepsilon)]/\hbar \tag{C.63}$$

$$\Gamma_{\uparrow\to 0} = \Gamma_{\downarrow\to 0} = \frac{\gamma_R+\gamma_L}{\hbar} - \int d\varepsilon\ D_1(\varepsilon)[\gamma_R f_R(\varepsilon) - \gamma_L f_L(\varepsilon)]/\hbar \tag{C.64}$$

$$\Gamma_{\uparrow\to 0} = \Gamma_{\downarrow\to 0} = \frac{\gamma_R+\gamma_L}{\hbar} - \Gamma_{0\to 1} \equiv \Gamma_{1\to 0} \tag{C.65}$$

Where we introduced

$$f_l(\varepsilon) = f\left(\frac{E_1-E_0-\mu_l}{k_B T}\right) \tag{C.66}$$

Notice that rates and probabilities do not depend on spin. Thus, we can recast the problem in terms of P_0 and $P_1 = P_\uparrow + P_\downarrow$. Then, we find

$$P_0 = \frac{\Gamma_{1\to 0}}{\Gamma_{1\to 0}+2\Gamma_{0\to 1}} \tag{C.67}$$

$$P_1 = \frac{2\Gamma_{0\to 1}}{\Gamma_{1\to 0}+2\Gamma_{0\to 1}} \tag{C.68}$$

Plugging them into the expression for the current, we get

$$I_L = -e(2P_0\Gamma^L_{0\to 1} - P_1\Gamma^L_{1\to 0}) \tag{C.69}$$

$$I_L = -2e\frac{\Gamma_{1\to 0}\Gamma^L_{0\to 1}-\Gamma_{0\to 1}\Gamma^L_{1\to 0}}{\Gamma_{1\to 0}+2\Gamma_{0\to 1}} \tag{C.70}$$

$$I_L = -2e\frac{\Gamma^R_{1\to 0}\Gamma^L_{0\to 1}-\Gamma^R_{0\to 1}\Gamma^L_{1\to 0}}{\frac{\gamma_R+\gamma_L}{\hbar}+\Gamma_{0\to 1}} \tag{C.71}$$

$$I_L = -2\frac{e}{\hbar}\frac{\gamma_R+\gamma_L}{(\gamma_R+\gamma_L)+\hbar\Gamma_{0\to 1}}\int d\varepsilon \frac{\gamma}{(\varepsilon-\varepsilon_1+eV_g)^2+(\gamma/2)^2}\left[f\left(\frac{\varepsilon-\mu_L}{k_B T}\right) - f\left(\frac{\varepsilon-\mu_R}{k_B T}\right)\right] \tag{C.72}$$

where

$$\Gamma_{0\to1} = \int d\varepsilon \frac{\gamma}{(\varepsilon-\varepsilon_1+eV_g)^2+(\gamma/2)^2}\left[\gamma_R f\left(\frac{\varepsilon-\mu_L}{k_BT}\right)+\gamma_L f\left(\frac{\varepsilon-\mu_R}{k_BT}\right)\right]/\hbar \qquad \text{(C.73)}$$

Notice that because of the term $\Gamma_{0\to1}$ in the denominator of the prefactor in *Equation C.72*, the expression for the current in the presence of spin is not exactly equal to twice that for the spinless case. However, if we are only interested in linear response, we can set $\mu_L = \mu_R = \mu$ in *Equation C.73*, in which case we obtain $\Gamma_{0\to1} \approx (\gamma_R + \gamma_L)/\hbar$, provided that $\varepsilon_1 - eVg < \mu$ (namely, when the energy level is brought below the Fermi energy in the leads). Then, the factor of 2 is approximately cancelled and we recover the expression for the spinless current. The current for the spinfull case is only exactly equal to twice that for the spinless case when the charging energy in the molecule is zero (non-interacting limit), in which case conductance through the molecule is spin degenerate.

Exact Solution of the Single-level Case (Spinless)

It is possible to solve the fully coherent single-level case by using the Keldysh non-equilibrium technique. The result is the following: the probability of the level to be occupied is equal to

$$P_1 = \sum_l \frac{\gamma_L}{\gamma_R+\gamma_L}\int \frac{d\varepsilon}{2\pi} f\left(\frac{\varepsilon-\mu_l}{k_BT}\right)\frac{\gamma}{(\varepsilon-\varepsilon_1+eV_g)^2+(\gamma/2)^2} \qquad \text{(C.74)}$$

where $\gamma = \gamma_R + \gamma_L$ (absence of any level broadening other than leakage of charge through the leads). The probability of the empty level configuration is $P_0 = 1 - P_1$. The expressions for the probabilities are identical to those obtained with the rate equations after when broadening of the energy level is incorporated.

The fact that the coherent and incoherent formulations yield the same results for the probabilities is not surprising. For single channel leads and a single level in the molecule, interference plays no role since there is only one conduction path. When the molecule has multiple independent paths for electrons to hop in and out, then the coherent and incoherent predictions depart, since interference between paths can result in enhancement or depletion of certain configuration occupations.

An expression for the current was derived by Jauho, Wingreen, and Meir [46] using the Keldysh Green's function technique. Their result was

$$I_L = -\frac{e}{\hbar}\int d\varepsilon \frac{\gamma}{(\varepsilon-\varepsilon_1+eV_g)^2+(\gamma/2)^2}\left[f\left(\frac{\varepsilon-\mu_L}{k_BT}\right)-f\left(\frac{\varepsilon-\mu_R}{k_BT}\right)\right] \qquad \text{(C.75)}$$

Contrary to our previous derivation using rate equations, this expression fully takes into account coherence. Yet, *Equation C.75* and *Equation C.51* are identical, provided that we set $\gamma = \gamma_R + \gamma_L$ (namely, no level broadening other than that due leakage through the leads).

Asymptotic for the current

Notice that

$$f\left(\frac{\varepsilon-\mu_L}{k_BT}\right)-f\left(\frac{\varepsilon-\mu_R}{k_BT}\right)=\frac{\sinh(\frac{eV_b}{k_BT})}{\cosh(\frac{\varepsilon+E_F}{k_BT})+\cosh(\frac{eV_b}{k_BT})} \qquad \text{(C.76)}$$

where $eV_b = \mu_L - \mu_R$ and $E_F = (\mu_L + \mu_R)/2$. Defining $\varepsilon' = \varepsilon - \varepsilon_1 + eV_g$, we can then rewrite *Equation C.75* as

$$I_L = -\frac{e}{\hbar}\int d\varepsilon'\, D(\varepsilon')\left[\frac{\sinh(\frac{eV_b}{k_BT})}{\cosh(\frac{\varepsilon+E_F}{k_BT})+\cosh(\frac{eV_b}{k_BT})}\right] \tag{C.77}$$

where

$$D(\varepsilon') = \frac{1}{\pi}\frac{\gamma/2}{\varepsilon'^2+(\gamma/2)^2} \tag{C.78}$$

It is easy to show that

$$\int d\varepsilon'\, D(\varepsilon') = 1 \tag{C.79}$$

Without loss of generality, we can set $eV_g = E_F$. Thus, ε_1 becomes the position of the energy level with respect the Fermi energy in the leads at zero bias. Then,

$$I_L = -\frac{e}{\hbar}\frac{\gamma_R\gamma_L}{\gamma_R+\gamma_L}\sinh(\frac{eV_b}{k_BT})\int d\varepsilon'\, D(\varepsilon')\frac{1}{\cosh(\frac{\varepsilon'+\varepsilon_1}{k_BT})+\cosh(\frac{eV_b}{k_BT})} \tag{C.80}$$

Let us look at some asymptotic limits.

- $\gamma \ll e|V_b| \ll k_BT \ll |\varepsilon_1|$: Weak broadening, finite bias, large temperature.

$$I_L \approx -\frac{e}{\hbar}\frac{\gamma_R\gamma_L}{\gamma_R+\gamma_L}(\frac{eV_b}{k_BT})\int d\varepsilon'\, D(\varepsilon')\frac{1}{\cosh(\frac{\varepsilon'+\varepsilon_1}{k_BT})+1} \tag{C.81}$$

$$I_L \approx -\frac{e}{\hbar}\frac{\gamma_R\gamma_L}{\gamma_R+\gamma_L}(\frac{eV_b}{k_BT})2e^{-\varepsilon_1/k_BT} \tag{C.82}$$

The current in this case shows an activation behavior, with the activation energy being the offset between the energy level in the molecule and the Fermi energy in the leads. Linear bias regime. On resonance, we find

$$I_L \approx -\frac{e}{\hbar}\frac{\gamma_R\gamma_L}{\gamma_R+\gamma_L}\frac{2eV_b}{k_BT} \tag{C.83}$$

- $\gamma \ll |\varepsilon_1| \ll k_BT \ll e|V_b|$: Weak broadening, intermediate temperature, large bias, nearly on resonance.
  - $I_L \approx -\frac{e}{\hbar}\frac{\gamma_R\gamma_L}{\gamma_R+\gamma_L}\sinh(\frac{eV_b}{k_BT})\int d\varepsilon'\, D(\varepsilon')\frac{1}{1+\cosh(\frac{eV_b}{k_BT})}$ (C.84)
  - $I_L \approx -\frac{e}{\hbar}\frac{\gamma_R\gamma_L}{\gamma_R+\gamma_L}$ (C.85)

  The current is approximately temperature and bias independent (non-linear bias regime).

- $\gamma \ll k_BT \ll |\varepsilon_1| \ll e|V_b|$: Similar to the previous case, more off-resonance.

$$I_L \approx -\frac{e}{\hbar}\frac{\gamma_R\gamma_L}{\gamma_R+\gamma_L}\frac{e^{e|V_b|/k_BT}}{2}\int d\varepsilon'\, D(\varepsilon')\frac{1}{\cosh\left(\frac{\varepsilon'+\varepsilon_1}{k_BT}\right)+e^{e|V_b|/k_BT}/2} \tag{C.86}$$

$$I_L \approx -\frac{e}{\hbar}\frac{\gamma_R\gamma_L}{\gamma_R+\gamma_L} \tag{C.87}$$

The current is again approximately temperature and bias independent.

- $\gamma \ll k_BT \ll e|V_b| < |\varepsilon_1|$: Similar to the previous case, but even more off-resonance.
  - $I_L \approx -\frac{e}{\hbar}\frac{\gamma_R\gamma_L}{\gamma_R+\gamma_L}\frac{e^{e|V_b|/k_BT}}{2}\int d\varepsilon'\, D(\varepsilon')\frac{1}{\cosh\left(\frac{\varepsilon'+\varepsilon_1}{k_BT}\right)+e^{e|V_b|/k_BT}/2}$ (C.88)
  - $I_L \approx -\frac{e}{\hbar}\frac{\gamma_R\gamma_L}{\gamma_R+\gamma_L}e^{(e|V_b|-|\varepsilon_1|)/k_BT}$ (C.89)

  The current shows activation behavior and is highly non-linear.

- γ, $e|V_b|$, $|\varepsilon_1| \ll k_B T$: High-temperature regime.

$$I_L \approx -\frac{e}{\hbar}\frac{\gamma_R\gamma_L}{\gamma_R+\gamma_L}\left(\frac{eV_b}{k_BT}\right)\int d\varepsilon'\, D(\varepsilon')\frac{1}{2} \tag{C.90}$$

$$I_L \approx -\frac{e}{\hbar}\frac{\gamma_R\gamma_L}{\gamma_R+\gamma_L}\left(\frac{eV_b}{2k_BT}\right) \tag{C.91}$$

The current decreases with the inverse of the temperature (linear bias regime).

- $k_BT \ll \gamma$: Low-temperature regime; strong broadening.
  - $I_L \approx -\frac{e}{\hbar}\frac{\gamma_R\gamma_L}{\gamma_R+\gamma_L}\sinh\left(\frac{eV_b}{k_BT}\right)\int d\varepsilon'\, D(\varepsilon')\frac{1}{\cosh\left(\frac{\varepsilon'+\varepsilon_1}{k_BT}\right)+\cosh\left(\frac{eV_b}{k_BT}\right)}$ (C.92)
  - $I_L \approx -\frac{e^2}{h}\frac{4\gamma_R\gamma_L}{(\gamma_R+\gamma_L)^2}V_b$ (C.93)

The current is temperature independent and linear with the bias voltage.

Conclusions

Given that for single-channel, single-level conductance both fully coherent (Keldysh) and sequentially incoherent (rate equation) approaches lead to the same expression for the current, we can conclude that the most general expression (at low bias) is given by

$$I_L = -\frac{e}{\hbar}\frac{\gamma_R\gamma_L}{\gamma_R+\gamma_L}\int d\varepsilon \frac{\gamma}{(\varepsilon-\varepsilon_1+eV_g)^2+(\gamma/2)^2}\left[f\left(\frac{\varepsilon-\mu_L}{k_BT}\right)-f\left(\frac{\varepsilon-\mu_R}{k_BT}\right)\right] \tag{C.94}$$

where we allow the total level width to include some broadening due to energy relaxation mechanisms other than leakage through the leads, namely, $\gamma = \gamma_R+\gamma_L+\gamma_0$.

APPENDIX D:
METHODS AND SYNTHESIS FOR FERROCENE-BASED INDIVIDUAL MOLECULES

Ferrocene-based individual molecules measured in *Chapter 4* were synthesized by Dr. Lejia Wang in Dr. Christian Nijhuis group (our chemistry collaborator) in the Department of Chemistry of the National University of Singapore.

Methods and Synthesis detail

$AcS(CH_2)_4Fc(CH_2)_4SAc$ were prepared from native ferrocene in three steps using well-established procedures displayed below in the synthesis detail section [63,64]. All compounds were characterized with ^{1}H NMR, ^{13}C NMR, and ESI HRMS. Briefly, ferrocene was substituted with 4-bromobutanoyl chloride via a Friedel-Crafts acylation to yield $(Br(CH_2)_3CO)_2Fc$ (1,5 g, 45% yield). Next, this compound was reduced with borane-tert-butylamine to yield $(Br(CH_2)_4)_2Fc$ (1.2 g, 88% yield). The bromine functionality was converted to a thioacetate functionality with potassium thioacetate and the $AcS(CH_2)_4Fc(CH_2)_4SAc$ was isolated with a yield of 95% (1.0 g).

This thioacetate derivative is stable and was stored under an atmosphere of N_2 at -20 °C. We found that the isolation of the free dithiol was problematic because of disulfide formation. Hence our choice to isolate and use the thioacetate protected derivative which was deprotected in situ for self-assembly of the junction.

The following chemicals were purchased from Sigma-Aldrich and used without further purification: 4-bromobutanoyl chloride, borane-tert-butylamine complex, ferrocene, anhydrous aluminum chloride and potassium ethanethioate. Solvents for chemical synthesis were freshly distilled prior to use: dichloromethane (DCM) was distilled from calcium chloride and tetrahydrofuran (THF) was distilled from sodium/benzophenone. Deionized water (18.2 MΩ cm) was generated from a water purifier (Purelab Option). All moisture sensitive reactions were

performed under a N_2-atmosphere. Thin layer chromatography (TLC) glass plates coated with 0.25 mm thick layer of silica gel 60 and fluorescent indication UV_{254} (Macherey-Nagel) were used to monitor the progress of the reactions. The products were purified by column chromatography over silica gel (pore size 60 Å, 230-400 mesh particle size, 40-63 μm particle size, Sigma-Aldrich). ^{1}H and ^{13}C NMR spectra were recorded on a Bruker Avance 300 MHz (AV300) spectrometer using chloroform-d as a solvent. Electrospray ionization (ESI) high resolution mass spectra were recorded on a Finnigan LCQ mass spectrometer.

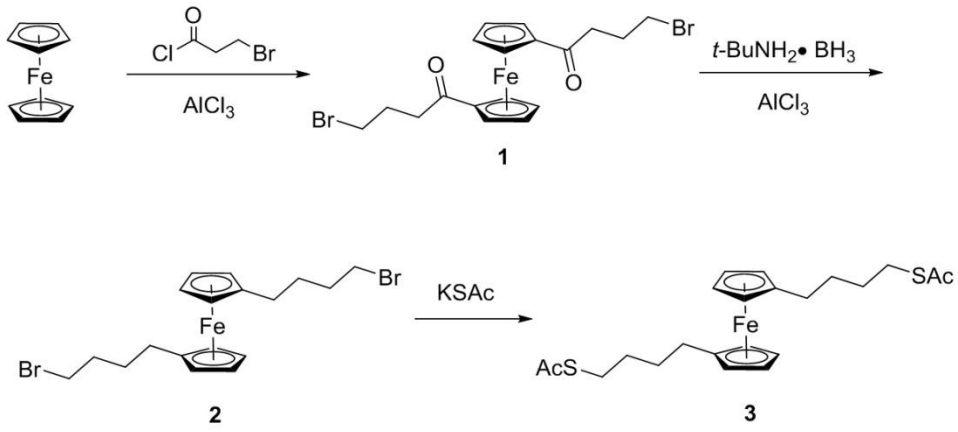

Figure 52: Synthetic route to prepare $AcS(CH_2)_4Fc(CH_2)_4SAc$ in three steps.

Compound 1

An acylation procedure was followed as described in the literature [63] to synthesize ω-bromo aliphatic-1,1′-diacylferrocenes. In a 100 ml Schlenk flask, ferrocene (1.3 g, 7 mmol) and anhydrous $AlCl_3$ (2.8 g, 21 mmol) were dissolved in anhydrous DCM (30 mL), next a solution of 4-bromobutanoyl chloride (2 mL, 17 mmol) in anhydrous DCM (25 mL) was added to the reaction mixture dropwise at room temperature. The reaction mixture was stirred for 3 h at room

temperature under a nitrogen atmosphere. After addition of deionized water (30 mL), the reaction mixture was stirred for an additional 10 min. The dark red colored organic layer was separated from the blue colored aqueous layer. The aqueous layer was extracted three times with DCM (25 mL) and the combined organic layers were washed with saturated sodium chloride, dried over sodium sulfate, filtered, and concentrated using rotary evaporation. The crude product was purified by column chromatography (hexane/DCM = 1:3) to yield the product (1,5 g, 45% yield) as a dark red oil.

^{1}H NMR ($CDCl_3$, 300 MHz) δ 4.83 (s, 4H), 4.54 (s, 4H), 3.58 (t, 4H, J=6.0 Hz), 2.88 (t, 4H, J=6.6 Hz), 2.26 (m, 4H); ^{13}C NMR ($CDCl_3$, 75 MHz) δ 202.1, 80.1, 73.6, 70.6, 37.5, 33.8, 26.6; ESI HRMS *m/z* calcd for $C_{18}H_{21}FeBr_2O_2$ 482.9253, found 482.9249 (M^++H).

Compound 2

The reduction was performed according to a literature [64] reported procedure. Borane-tert-butylamine complex (1.56 g, 18 mmol) in anhydrous DCM (50 mL) was added at 0 °C to a suspension of $AlCl_3$ (1.2 g, 9 mmol) in anhydrous DCM (50 mL), the resulting mixture was allowed to stir at 0 °C for 1h until a clear solution was obtained. A solution of compound **1** (1.45 g, 3 mmol) in anhydrous DCM (25 mL) was added dropwise. The reaction mixture was stirred at 0 °C for 2 h and then hydrolyzed with deionized water (30 mL). The aqueous layer was extracted three times with DCM (25 mL) and the combined organic layers were washed with 0.1 M HCl, water and saturated sodium chloride, dried over sodium sulfate, filtered, and concentrated using

rotary evaporation. The crude product was purified by column chromatography (hexane/DCM = 10:1) to provide product (1.2 g, 88% yield) as a yellow oil.

^{1}H NMR ($CDCl_3$, 300 MHz) δ 4.07 (s, 8H), 3.41 (t, 4H, J=6.6 Hz), 2.29 (t, 4H, J=6.9 Hz), 1.88 (t, 4H, J=6.9 Hz), 1.65 (m, 4H); ^{13}C NMR ($CDCl_3$, 75 MHz) δ 89.3, 69.3, 68.5, 33.8, 32.5, 29.6, 28.5; ESI HRMS *m/z* calcd for $C_{18}H_{24}FeBr_2$ 453.9589, found 453.9596 (M^+).

Compound 3

In a 100 ml Schlenk flask, potassium thioacetate (0.72g, 6.25 mmol) and compound 2 (1.15 g, 2.5mmol) were dissolved in anhydrous THF (50 mL). The solution was refluxed for 2 hour, and then allowed to cool to room temperature overnight. The resulting mixture was poured into water and extracted with ethyl acetate. The combined organic layers were washed with saturated sodium chloride, dried over sodium sulfate, filtered, and concentrated using rotary evaporation. The crude product was purified by column chromatography (hexane/DCM = 3:1) to provide product (1 g, 95% yield) as a yellow oil.

^{1}H NMR ($CDCl_3$, 300 MHz) δ 4.04 (s, 8H), 2.87 (t, 4H, J=6.9 Hz), 2.32 (s, 6H), 2.27 (t, 4H, J=7.2 Hz), 1.58 (m, 8H); ^{13}C NMR ($CDCl_3$, 75 MHz) δ 195.9, 89.4, 69.2, 68.3, 30.6, 30.3, 29.3, 28.9, 28.8; ESI HRMS *m/z* calcd for $C_{22}H_{31}FeO_2S_2$ 447.1109, found 447.1107 (M^++H).

LIST OF REFERENCES

1. Park, H. *et al*. Nanomechanical oscillations in a single-C60 transistor. *Nature* **407,** 57-60 (2000).
2. Park, J. *et al*. Coulomb blockade and the kondo effect in single atom transistors. *Nature* **417,** 722-725 (2002).
3. Liang, W. J., Shores, M. P., Bockrath, M., Long, J. R. & Park, H. Kondo resonance in a single-molecule transistor. *Nature* **417,** 725-729 (2002).
4. Kubatkin, S. *et al*. Single-electron transistor of a single organic molecule with access to several redox states. *Nature* **425,** 698-701 (2003).
5. Zhetenev, N. B., Meng, H. & Bao, Z. Conductance of small molecular junctions. *Phys. Rev. Lett*. **88,** 226801 (2002).
6. Yu, L. H. *et al*. Inelastic electron tunneling via molecular vibrations in single-molecule transistors. *Phys. Rev. Lett.* **93,** 266802 (2004).
7. Haque, F., Langhirt (UG), M., del Barco, E., Taguchi, T. & Christou, G. Magnetic field dependent transport through a Mn4 single-molecule magnet. *J. Appl. Phys.* **109,** 07B112 (2011).
8. Jo, M. *et al*. Signatures of Molecular Magnetism in Single-Molecule Transport Spectroscopy. *Nano Lett.* **6,** 2014-2020 (2006).
9. Poot, M. *et al*. Temperature dependence of three-terminal molecular junctions with sulfur end-functionalized tercyclohexylidenes. *Nano Lett*. **6,** 1031-1035 (2006).
10. Díez-Pérez, I. *et al*. Rectification and stability of a single molecular diode with controlled orientation. *Nat Chem*. **1,** 635-641 (2009).
11. Venkataraman, L., Klare, J. E., Nuckolls, C., Hybertsen, M. S. & Steigerwald, M. L. Dependence of single-molecule junction conductance on molecular conformation. *Nature* **442,** 904-907 (2006).
12. Chiechi, R. C., Weiss, E. A., Dickey, M. D. & Whitesides, G. M. Eutectic gallium–indium (EGaIn): a moldable liquid metal for electrical characterization of self-assembled monolayers. *Angew. Chem. Int. Ed*. **47,** 142-146 (2008).
13. Reus, W. F., Thuo, M. N., Shapiro, N. D., Nijhuis, C. A. & Whitesides, G. M. The SAM, not the electrodes, dominates charge transport in metal-monolayer// Ga2O3/gallium-indium eutectic junctions. *ACS Nano* **6,** 4806-4822 (2012).
14. Nijhuis, C. A., Reus, W. F., Barber, J. & Whitesides, G. M. Comparison of SAM-based tunneling junctions with Ga2O3/EGaIn top-electrodes to other large-area junctions. *J. Phys. Chem*. **116,** 14139-14150 (2012).
15. Fracasso, D., Valkenier, H., Hummelen, J. C., Solomon, G. & Chiechi, R. C. Evidence for quantum interference in SAMs of arylethynylene thiolates in tunneling junctions with

eutectic Ga-In (EGaIn) top-contacts. *J. Am. Chem. Soc*. **133,** 9556-9563 (2011).

16. Nijhuis, C. A., Reus, W. F., Barber, J., Dickey, M. D. & Whitesides, G. M. Charge transport and rectification in arrays of SAM-based tunneling junctions. *Nano Lett*. **10,** 3611- 3619 (2010).
17. Fracasso, D., Muglali, M. I., Rohwerder, M., Terfort, A. & Chiechi, R. C. Influence of an atom in EGaIn/Ga2O3 tunneling junctions comprising self-assembled monolayers. *J. Phys. Chem*. **117,** 1136-11376 (2013).
18. McCreery, R. L. & Bergren, A. Progress with molecular electronic junctions: meeting experimental challenges in design and fabrication. J. *Adv. Mater*. **21,** 4303-4322 (2009).
19. Haj-Yahia, A.-E. *et al*. Substituent variation drives metal/monolayer/semiconductor junctions from strongly rectifying to ohmic behavior. *Adv. Mater*. **25,** 702-706 (2013).
20. Bowers, C. M. *et al*. Characterizing the metal–SAM interface in tunneling junctions. *Nano Lett*. **9,** 1471-1477 (2015).
21. Zhang, Y., Zhao, Z., Fracasso, D. & Chiechi, R. C. Bottom-Up molecular tunneling junctions formed by self-assembly. *Isr. J. Chem*. **54,** 513-533 (2014).
22. Yoon, H. J. *et al*. Rectification in tunneling junctions: 2,2′-bipyridyl-terminated n-alkanethiolates. *J. Am. Chem. Soc*. **136,** 17155–17162 (2014).
23. Perrin, M. L. *et al*. Large tunable image-charge effects in single-molecule junctions. *Nat. Nanotechnol*. **8,** 282-287 (2013).
24. Yuan, L., Breuer, R., Jiang, L., Schmittel, M. & Nijhuis, C. A. Molecular diode with a statistically robust rectification ratio of three orders of magnitude. *Nano Lett*. **15,** 5506–5512 (2015).
25. Capozzi, B. *et al*. Single-molecule diodes with high rectification ratios through environmental control. *Nat. Nanotechnol*. **10,** 522-527 (2015).
26. Beenakker, C. W. J. Theory of Coulomb-blockade oscillations in the conductance of a quantum dot. *Phys. Rev. B* **44,** 1646-1656 (1991).
27. Kouwenhoven, L.P. *et al*. Electron Transport in Quantum Dots, in Mesoscopic Electron Transport. (Sohn, L. L., Kouwenhoven, L. L. & Schoen, G., Plenum: New York and London, 105-214, 1997).
28. Park, J. Electron Transport in Single Molecule Transistors, University of California, Berkeley (1996).
29. Thijssen, J. M. & Van der Zant, H. S. J. Charge transport and single-electron effects in nanoscale systems. *Phys. Stat. Sol.* **245,** 1445-1470 (2008).
30. Pasupathy, A. N. Electron transport in molecular transistors, Cornell University (2004).
31. Grose, J. E. Electron transport in single-molecule transistor based on high-spin molecules, Cornell University (2007).

32. Bartolome, J., Luis, F. & Fernandez, J. F. Molecular Magnets, NanoScience and Technology. Ch. 12. (Springer-Verlag Berlin Heidelberg, 2014).

33. Yuan, L. *et al*. Controlling the direction of rectification in a molecular diode. *Nat. Commun.* **6,** 6324 (2015).

34. Breuer, R. & Schmittel, M. Redox-stable SAMs in water (pH 0–12) from 1,1′-biferrocenylene-terminated thiols on gold. *Organometallics* **31,** 6642-6651 (2012).

35. Henderson, J. J., Ramsey, C. M., del Barco, E., Mishra, A. & Christou, G. Fabrication of nano-gapped single-electron transistors for transport studies of individual single-molecule magnets. *J. Appl. Phys.* **101,** 09E102 (2007).

36. Haque, F. H. Single-Electron Transport Spectroscopy Studies on Magnetic Molecules and Nanoparticles, University of Central Florida (2011).

37. Durkan, C., Schneider, M. A. & Welland, M. E. Analysis of failure mechanisms in electrically stressed Au nanowires. *J. Appl. Phys.* **86,** 1280 (1999).

38. O'Neill, K., Osorio, E. A. & van der Zant, H. S. J. Self-breaking in planar few-atom Au constrictions for nanometer-spaced electrodes. *Appl. Phys. Lett*. **90,** 133109 (2007).

39. Landauer, R. Can a length of perfect conductor have a resistance? R. *Phys. Rev. A* **85,** 91-93 (1981).

40. Park, T. *et al*. Formation and structure of self-assembled monolayers of octylthioacetates on Au(111) in catalytic tetrabutylammonium cyanide solution. *Bull. Korean Chem. Soc.* **30,** 441-444 (2009).

41. Smith, C.E. *et al*. Length dependent nanotransport and charge hopping bottlenecks in long thiophene-containing π-conjugated molecular wires. *J. Am. Chem. Soc.* **137,** 15732-15741 (2015).

42. Kumar, K. S., Pasula, R. R., Lim, S. & Nijhuis, C. A. Long-range tunneling processes across ferritin-based junctions. *Adv. Mater.* 10.1002/adma.201504402 (2015).

43. Yan, H. *et al*. Activationless charge transport across 4.5 to 22 nm in molecular electronic junctions. *Proc. Natl. Acad. Sci. USA* **110,** 5326 (2013).

44. Marcus, R. A. On the theory of oxidation-reduction reactions involving electron transfer I. *J. Chem. Phys.* **24,** 966-978 (1956).

45. Arrhenius, S. Concerning the heat of dissociation and the influence of the temperature on the degree of dissociation of electrolytes. *Z. Phys. Chem.* **4,** 96-116 (1889).

46. Jauho, A.-P., Wingreen, N. S. & Meir, Y. Time-dependent transport in interacting and noninteracting resonant-tunneling systems. *Phys. Rev. B* **50,** 5528-5544 (1994).

47. Datta, S. *et al*. Current-voltage characteristics of self-assembled monolayers by scanning tunneling microscopy. *Phys. Rev. Lett.* **79,** 2530 (1997).

48. Heurich, J., Cuevas, J. C., Wenzel, W. & Schön, G. Electrical transport through single-molecule junctions: from molecular orbitals to conduction channels. *Phys. Rev. Lett.* **88,**

256803 (2002).

49. Kornilovitch, P. E., Bratkovsky, A. M. & Williams, R. S. Current rectification by molecules with asymmetric tunneling barriers. *Phys. Rev. B* **66,** 165436 (2002).

50. Moth-Poulson, K. & Bjornholm, T. Molecular electronics with single molecules in solid-state devices. *Nat. Nanotechnol*. **4,** 551-556 (2009).

51. Datta, S. Lessons from Nanoelectronics: A New Perspective on Transport. Vol. 1 (World Scientific, Singapore, 2012).

52. Kergueris, C. *et al*. Electron transport through a metal-molecule-metal junction. *Phys. Rev. B* **59,** 12505 (1999).

53. Suchand Sangeeth, C. S., Wan, A. & Nijhuis, C. A. Equivalent circuits of a self-assembled monolayer-based tunnel junction determined by impedance spectroscopy. *J. Am. Chem. Soc.* **136,** 11134-11144 (2014).

54. Holmes, B. T. & Snow, A. W. Aliphatic thioacetate deprotection using catalytic tetrabutylammonium cyanide. *Tetrahedron* **61,** 12339-12342 (2005).

55. Tao, N. J. Electron transport in molecular junctions. *Nature Nanotech*. **1,** 173–181 (2006).

56. Xue, Y. & Ratner, M.A. Microscopic study of electrical transport through individual molecules with metallic contacts. I. Band lineup, voltage drop, and high-field transport. *Phys. Rev. B*, **68,** 115406 (2003).

57. Nitzan, A., Galperin, M., Ingold, G-L. & Grabert, H. On the electrostatic potential profile in biased molecular wires. *J. Chem. Phys.* **117,** 10837-10841 (2002).

58. Liang, G. C., Ghosh, A. W., Paulsson, M. & Datta S. Electrostatic potential profiles of molecular conductors. *Phys. Rev. B* **69,** 115302 (2004).

59. Simmons, J. G. Generalized Formula for the Electric Tunnel Effect between Similar Electrodes Separated by a Thin Insulating Film. *J. Appl. Phys.* **34,** 1793-1803 (1963).

60. Morpurgo, A. F., Marcus, C. M. & Robinson, D. B. Controlled fabrication of metallic electrodes with atomic separation. *Appl. Phys. Lett.* **74,** 2084-2086 (1999).

61. Holmlin, R. E. *et al*. Electron Transport through Thin Organic Films in Metal−Insulator−Metal Junctions Based on Self-Assembled Monolayers. *J. Am. Chem. Soc.* **123,** 5075-5085 (2001).

62. Cui, X. D. *et al*. Changes in the Electronic Properties of a Molecule When It Is Wired into a Circuit. *J. Phys. Chem. B* **106,** 8609-8614 (2002).

63. Vulugundam, G., Kumar, K., Kondaiah, P. & Bhattacharya, S. Efficacious redox-responsive gene delivery in serum by ferrocenylated monomeric and dimeric cationic cholesterols. *Org. Biomol. Chem.* **13,** 4310-4320 (2015).

64. Gharib, B. & Hirsch, A. Synthesis and Characterization of new ferrocene-containing ionic liquids. Eur. *J. Org. Chem.* **19,** 4123-4136 (2014).